



# ECC-SMART PROJECT

**Joint European Canadian Chinese development of Small Modular Reactor Technology**

Grant Agreement Number: 945234  
H2020 – NFRP-2019-2020

Start Date of the Project: 1/09/2020  
Duration: 54 Months

<b>Deliverable Title:</b>	D3.1 Report summarizing the newly generated reference data for natural convection, forced and mixed convection and decay heat removal
<b>Lead party:</b>	KIT
<b>Author(s):</b>	Ivan Otic (KIT)
<b>Participant(s):</b>	<b>KIT:</b> Fabian Wiltschko <b>CNL:</b> Armando Nava, Chukwudy Azih <b>CVR:</b> Monika Šípová, Jan Vít <b>IPP:</b> Vladislav Filonov, Yuliia Filonova <b>USFD:</b> Kenneth Chinembiri, Shuisheng He
<b>Due Date:</b>	31/08/2024

**Version Number:**

**0.4**

**Approved by: Coordinator**

**Date: 6.11.2024**

Dissemination level		
<b>PU</b>	Public	<b>X</b>
<b>CO</b>	Confidential: only for ECC-SMART Partners (including the Commission Services)	
<b>EU-RES</b>	Classified Information: RESTREINT UE*	
<b>EU-CON</b>	Classified Information: CONFIDENTIEL UE*	
<b>EU-SEC</b>	Classified Information: SECRET UE*	

## Document History – Version Control

Version	Issue Date	Stage	Description of Changes	Contributor
0.3	30.10.2024	Draft Version	3. version	KIT, CNL, CVR, IPP, USFD
0.4	6.11.2024	Final version	4. version	KIT, CNL, CVR, IPP, USFD

## Project information

<b>Project acronym:</b>	ECC-SMART
<b>Project title:</b>	Joint European Canadian Chinese development of Small Modular Reactor Technology
<b>Grant Agreement n°</b>	945234
<b>Start date:</b>	1.9.2020
<b>Duration</b>	54 months
<b>Programme:</b>	Framework Programme for Research and Innovation (2019-2020) under the call NFRP-2019-2020
<b>Coordinator:</b>	Centrum Výzkumu Řež, s.r.o. (Czech Republic)

## Document information

<b>Work package:</b>	WP3 Thermal Hydraulics and Safety of the SCW-SMR
<b>Contractual Date of Delivery:</b>	31/08/2024
<b>Actual Date of Delivery to the EC:</b>	06/11/2024
<b>Document type:</b>	Report
<b>Dissemination level:</b>	Public (PU)
<b>Number of pages:</b>	78

### **Abstract:**

This report summarises results obtained in the Task 3.2 "Reference Database" activities within WP3, focusing on the collection of existing and generation of new data for supercritical water reactors (SCWR). Through six subtasks, the work combines experimental investigations, direct numerical simulations (DNS), and material corrosion studies which were performed in close cooperation with WP2. Research activities include heat transfer analyses under rough surface conditions; DNS of turbulent flows at postulated operating conditions, long-duration steel corrosion tests, and development of CFD solvers. The resulting comprehensive experimental and numerical database, created within this task and the ECC-SMART project provides crucial data for design and safety analysis. This research significantly contributes to the technical knowledge base required for SCW-SMR development.

## Copyright / Disclaimer

The document is property of the ECC-SMART consortium members. This document reflects only the author's view. It does not represent the view of the European Commission and the European Commission is not responsible for any use that may be made of the information it contains. This deliverable contains original unpublished work except where clearly indicated otherwise. Acknowledgement of previously published material and of the work of others has been made through appropriate citation, quotation or both. No copying or distributing, in any form or by any means, is allowed without the prior written agreement of the owner of the property rights



*The ECC-SMART project has received funding from the Euratom research and training programme 2019-2020 under grant agreement No 945234.*

## Executive Summary

Work package three (WP3) is focused on thermal-hydraulic investigations related to the design and safety of the SCW-SMR. The knowledge and experience gained from these developments will support the design specifications and optimise the SCW-SMR proposed in this ECC-SMART project. Within WP3, Task 3.2, "Reference Database," focuses on assembling existing and generating new data for thermal-hydraulic investigations. This work established close cooperation between the WP2 dedicated to nuclear materials, and the WP3 dedicated to thermal hydraulics and safety. One main goal of this task and the whole project is to perform studies of corrosion impact on heat transfer to coolant and moderator under supercritical pressure conditions.

The knowledge and data provided in this task support the design and safety research and development for SCW-SMR.

This Deliverable 3.1 summarizes the activities within Task 3.2 on assembling existing and generating new data for thermal-hydraulic investigations.

### Subtask 3.2.1 Experimental investigations of turbulent heat transfer along corroded surfaces (KIT)

- Conducted comparative analyses using smooth and rough tubes provided by the project partners from WP2 and within the subtask 3.2.3.
- Evaluated heat transfer coefficients across varying surface conditions.
- Generated new data on surface roughness effects under supercritical pressure conditions.

### Subtask 3.2.2 Investigations of turbulent flows along corroded surface (CNL)

- Performed direct numerical simulations (DNS) using ANSYS CFX computational fluid dynamics (CFD) software.
- Based on the DNS results, analysed effects of smooth and rough surfaces on turbulent forced convection at the inflow Reynolds number 12,000.
- Generated new reference DNS data for turbulent forced convection under supercritical conditions.

### Subtask 3.2.3 Exposure of experimental specimens (CVR)

- Exposure of the fuel cladding specimens to supercritical water (at 500°C/25 MPa).
- Conducted long-duration testing up to 10,000 hours and provided statistical analysis for selected steels.
- Experimental setup and data analysis were performed in close cooperation with the WP2.
- Manufactured test tubes with varying surface roughness for thermal-hydraulic experiments. The tubes were provided to project partners for experimental thermal hydraulic investigations within the subtask 3.2.1.

### Subtask 3.2.4 Direct numerical simulations (DNS) of flow over rough surfaces (USFD)

- Utilized immersed boundary method for in-house DNS solver CHAPSm2.
- Investigated asymmetrically heated channel flow.
- Analysed both smooth and pyramid-roughened surfaces in supercritical water.
- Generated new reference DNS data for turbulent forced and mixed convection under supercritical conditions.

### Subtask 3.2.5 DNS of turbulent heat transfer under supercritical pressure conditions (KIT)

D3.1 Report summarizing the newly generated reference data for natural convection, forced and mixed convection and decay heat removal

- Developed customized compressible DNS solver for flow, heat and mass transfer and implemented it in the open source CFD code OpenFOAM.
- Validated the new solver against literature data.
- Analysed turbulent natural convection for different temperature ranges in supercritical water.
- Generated new reference data for turbulent natural convection under supercritical conditions.

Subtask 3.2.6 Assembling the existing experimental database (IPP)

- Consolidated existing and newly generated experimental and numerical data.
- Created comprehensive reference database for thermal-hydraulic investigations.

### **Impact and Applications**

The integrated database provides essential insights for SCW-SMR design, design optimization and safety analysis. The combination of experimental data and high-performance numerical simulations results offers a robust foundation for understanding thermal-hydraulic behaviour in supercritical water conditions, particularly regarding surface roughness effects and heat transfer characteristics. CFD software for high performance computing is further developed and validated to provide new reference data. Material corrosion tests for selected materials are performed in close cooperation with the WP2 and provided to the project partners for further numerical analysis and modelling. This research significantly contributes to the technical knowledge base required for SCW-SMR development.

## Table of contents

Nomenclature.....	9
List of acronyms and abbreviations.....	9
List of tables .....	10
List of figures .....	10
Related documents .....	12
1 Introduction.....	13
2 Experimental investigations of turbulent heat transfer along corroded surfaces (KIT) .....	15
2.1 Performed work and goals .....	15
2.2 Experimental setup and methodology .....	16
2.3 KIT Model Fluid Facility – KIMOF.....	16
2.4 Test section .....	17
2.5 Wall roughness of the different test tubes .....	18
2.6 Measurement devices .....	20
2.6.1 Thermocouples for wall temperature measurement.....	20
2.6.2 Thermocouples inlet and outlet temperature .....	20
2.6.3 Pressure sensors.....	21
2.6.4 Flow meter .....	21
2.6.5 Heat power measurement .....	22
2.6.6 Uncertainty of measurement devices .....	22
2.7 Heat loss .....	22
2.8 Test procedure and parameter range .....	23
2.9 The reference database.....	24
2.10 Publications .....	25
3 Investigations of turbulent heat transfer along corroded surfaces (CNL) .....	26
3.1 Background.....	26
3.2 Objective .....	26
3.3 Investigations on smooth surface baseline cases at subcritical conditions.....	27
3.3.1 Test case .....	27
3.3.2 Methodology .....	27
3.3.3 Results and discussion.....	29
3.4 Investigations on smooth surface baseline cases at supercritical conditions.....	30
3.4.1 Test case .....	30
3.4.2 Methodology .....	30

3.4.3	Results and discussion.....	31
3.5	Investigations on rough surface baseline cases at subcritical conditions.....	33
3.5.1	Test cases .....	33
3.5.2	Methodology .....	34
3.5.3	Results and discussion.....	35
3.6	Investigations on rough surface baseline cases at supercritical conditions .....	37
3.6.1	Test case .....	37
3.6.2	Methodology .....	37
3.6.3	Results and discussion.....	40
4	Exposition of experimental specimens (CVR).....	43
4.1	Experimental details.....	43
4.1.1	Materials and specimens.....	43
4.1.2	Autoclave.....	44
4.1.3	Campaigns .....	45
4.1.4	Measurement of the surface roughness .....	46
4.1.5	Evaluation of the oxide layer .....	46
4.2	Results of the long-term exposure .....	46
5	Direct numerical simulations of flow over rough surfaces (USFD) .....	50
5.1	Introduction.....	50
5.2	Methodology .....	50
5.3	Immersed Boundary Method (IBM) .....	51
5.4	Thermal boundary conditions for a rough surface using the Immersed Boundary Method .....	52
5.5	Validation and Verification.....	54
5.6	Description of cases in the reference database .....	56
5.7	The reference database.....	57
6	Numerical simulations of turbulent heat transfer under supercritical pressure conditions (KIT) .....	60
6.1	Introduction.....	60
6.2	Optimization approach for heat transfer similarity analysis.....	60
6.3	CFD solver .....	61
6.4	Simulation setup and results .....	62
6.4.1	Reference case .....	62
6.4.2	Computational Mesh and Initial Fields.....	63
6.5	Solver Validation .....	66
6.6	DNS of natural convection in water at supercritical pressure conditions.....	66



6.7 Summary and Outlook..... 69

7 Assembling the existing experimental data base (IPP) ..... 71

## Nomenclature

Full nomenclature description is given in Tables 8.1 to 8.4 at pp. 73 ff.

## List of acronyms and abbreviations

ANSYS	Engineering simulation software
CCP-NTH	Collaborative Computational Project Nuclear Thermal Hydraulics
CFD	Computational Fluid Dynamics
CFX	ANSYS CFD software
CG	Conjugate gradient
CHAPSm2	USFD DNS Software
CHT	Conjugate Heat Transfer
CNL	Canadian National Laboratories
CVR	Centrum Výzkumu Řež, s.r.o.
CWF	Constant Wall Flux
CWT	Constant Wall Temperature
DIC	Diagonal Incomplete Cholesky
DNS	Direct Numerical Simulation
ECC-SMART	Joint European Canadian Chinese development of Small Modular Reactor Technology
IAEA	International Atomic Energy Agency
IAPWS	International Association for Properties of Water and Steam
IBM	Immersed Boundary Method
ID	Inner diameter
IPP	IPP Centre
IPPE	Test facility
ISO	International Organization for Standardization
JIHTRAS	Test facility
KIT	Karlsruhe Institute of Technology
KIMOF	KIT Model Fluid Facility
L	Length
LOCA	Loss of Coolant Accident
LVDT	Linear Variable Differential Transformer
LWR	Light Water Reactor
MSTF	Test facility
NTUU	Test facility
OD	Outer diameter
OpenFOAM	Open-source CFD software
PAA-33X	Pressure transmitter by Keller
PIO	Physics Informed Optimization
RANS	Reynolds Averaged Navier Stokes
RHS	Right-hand side
RPM	Revolutions per minute
SEM	Scanning electron microscope
SCW	Supercritical Water
SCW-SMR	Small modular reactor cooled by supercritical water

SCWR	Supercritical Water Reactor
SMR	Small modular reactor
TKE	Turbulence kinetic energy
USFD	University of Sheffield
WP	Work Package

## List of tables

Table 2-1: Roughness parameters of the smooth test tube .....	18
Table 2-2: Roughness parameters of the rough test tube.....	19
Table 2-3: Uncertainty of measurement devices.....	22
Table 2-4: Ranges of experimental parameters.....	23
Table 2-5: Titles in the experimental database .....	24
Table 4-1: Chemical composition (in %wt.) of the selected materials.....	43
Table 4-2: Selected physical properties (corresponding T at 20°C) of materials of interest.....	44
Table 5-1: Table of verification and validation tests carried out for the immersed boundary method .....	54
Table 5-2: Cases presently contained in the reference database .....	57
Table 6-1 Cases considered for the simulation.....	63
Table 6-2: $y^+$ Values for Different Surfaces.....	66
Table 6-3: $y^+$ Values for Different Surfaces.....	68

## List of figures

Figure 1: Scheme of the KIMOF test facility.....	17
Figure 2: Schematic view of the test section.....	18
Figure 3: Cutting of the rough tube. ....	19
Figure 4: Mounted thermocouples for wall temperature measurement .....	20
Figure 5: Scheme of thermocouples for inlet and outlet temperature .....	21
Figure 6: Coiled tubing and pressure transducer. ....	21
Figure 7: Heat loss experiment and polynomial fitting.....	23
Figure 8: Illustration of the computational domain for the channel simulations.....	27
Figure 9 Wall-normal grid spacing for smooth wall simulations.....	28
Figure 10 Mean flow properties evaluated at $x\delta = 9$ for the smooth subcritical turbulent channel case: a) streamwise velocity component; b) root-mean-square of perturbation velocity components.....	29
Figure 11 Specific rates of turbulence kinetic energy budgets evaluated at $x\delta = 9$ smooth subcritical turbulent channel case.....	30
Figure 12 Mean temperature evaluated at $x\delta = 9$ for the smooth subcritical turbulent channel case .....	30
Figure 13 Mean flow properties evaluated at $x\delta = 2$ (a and b) and $x\delta = 9$ (c and d) for the smooth turbulent channel cases: a,c) streamwise velocity component; b,d) root-mean-square of perturbation velocity components, solid line is u, dashed is v, and dotted is w. ....	31
Figure 14 Turbulence kinetic energy budgets evaluated at $x\delta = 9$ for the smooth turbulent channel cases: a) Production of TKE from mean shear (solid line) and from buoyancy (dash-dotted line); b) dissipation of TKE by the mean shear. ....	32

## D3.1 Report summarizing the newly generated reference data for natural convection, forced and mixed convection and decay heat removal

Figure 15 Temperature distribution for the smooth wall test cases at $x\delta = 9$ . A) wall-normal temperature profile. b) streamwise temperature profile.....	32
Figure 16 Computational domain and boundary conditions for the subcritical turbulent cases with a boundary layer: a) cavity-type surface roughness; b) protrusion-type surface roughness. ....	34
Figure 17 Mesh resolution for the cavity-type surface roughness. ....	35
Figure 18 Mesh resolution for the protrusion-type surface roughness.....	35
Figure 19 Distribution of instantaneous a) streamwise (u) b) wall-normal (v) component of velocity over the centre streamwise row at three wall-normal distances for the subcritical turbulent-boundary-layer over rough surfaces. ....	36
Figure 20 Distributions of time-averaged streamwise vorticity in three yz planes for cubic protrusions in the subcritical turbulent- boundary-layer over rough surfaces.....	37
Figure 21 Partial view of grid in the computational domain and the highly refined region.....	38
Figure 22 Distribution of streamwise (x) component of velocity at the wall with modelled cavity-type surface $dr+ = 5.0$ (left); b) $dr+ = 10.0$ (right). ....	39
Figure 23 : Uniform array of modelled surface cavities, prescribed as a profile of the streamwise component of velocity, along the surface.....	39
Figure 24 Wall velocity profile for alternating patches of surface cavities ( $dr+ = 10.0$ ) and smooth wall patches. The grey regions flanking the profile correspond to the parts of the surface outside of the highly-refined grid region. A no-slip boundary condition is imposed on these parts of the surface. ....	39
Figure 25 Heat flux boundary condition implemented on the channel wall at the $y=0$ plane.....	40
Figure 26 Streamwise variation of normalized wall temperature difference, for supercritical conditions; results correspond to a smooth wall (a), small wall cavities ( ) (b), large wall cavities ( ) (c), and alternating patches of large wall cavities ( ) (d).....	41
Figure 27: The sketch of the autoclave and accompanying equipment.....	45
Figure 28: Scheme of the campaigns performed within WP3 based on cooperation with WP2.	45
Figure 29: The evaluation of the surface roughness during exposure in SCW at 500 °C/25 MPa up to 10,000 hours .....	47
Figure 30: The SEM images of the surface of stainless steel 316Ti at the as - received state(a), after 4,000h in SCW 500 ° C/25MPa (b), and after 10,000 h in SCW 500 °C/25MPa in the cross-section (c).....	48
Figure 31: The 3D model of the surface of the stainless steel 316Ti before the exposure (as-received state), after 4,000 h in SCW 500 °C/25 MPa, and after 10,000 h in SCW 500 °C/25 MPa. ....	48
Figure 32: The SEM images of the surface of stainless steel 310S at as-received state (a), after 4,000 h in SCW 500 °C/25 MPa (b), and after 10,000 h in SCW 500 °C/25 MPa (c) also in the cross-section (d).....	48
Figure 33: The 3D model of the surface of the stainless steel 310S before the exposure (as-received state), after 4,000 h in SCW 500 °C/25 MPa, and after 10,000 h in SCW 500 °C/25 MPa .....	49
Figure 34: The SEM images of the surface of alloy 800H at as-received state (a), after 4,000 h in SCW 500 °C/25 MPa (b), and after 10,000 h in SCW 500 °C/25 MPa (c) also in the cross-section (d). ....	49
Figure 35: The 3D model of the surface of the alloy 800H after 4,000 h, and after 10,000 h in SCW 500 °C/25 MPa.....	49
Figure 36: Illustrations of complex bodies imposed on a 2D cartesian grid. Right hand side figure from Fadlun et. al, 2000.....	51

Figure 37: Illustration of the steps required to model an immersed body or rough surface in CHAPSim2. The steps for geometry description and Identification of node type are only performed once at the beginning of the computation. ....	52
Figure 38: Schematic of the conjugate heat transfer implementation.....	53
Figure 39: Sketch showing the computation of the artificial boundary face temperature. In Figure (a), the physical temperature variation is shown. Figure (b) shows the numerical temperature variation is shown.....	54
Figure 40: Comparison of the normal stresses against the data from Seddighi et. al., 2015. Note that the reference data has only the bottom wall rough, while the present simulation has both surfaces roughened.....	55
Figure 41: Test 2a – Nusselt number, $C_p$ and $C_f$ comparisons for an unconfined cylinder with a constant wall temperature boundary condition. Comparisons are made against the data from Das et al., 2018 and Tseng and Ferzinger, 2003. ....	55
Figure 42: Test 2b – Nusselt number comparison for an unconfined cylinder with constant heat flux verification test case. Comparison is against data from Das et. al., 2018 .....	56
Figure 43: Test 3 – Sketch of the modelled domain for pure conduction for an immersed sphere in a heated channel. ....	56
Figure 44: Modelled domain for rough wall simulations. Insert is a close-up of the roughness topography. The gravity vector is oriented in the streamwise direction for the vertical cases, and in the wall normal direction for horizontal case .....	57
Figure 45: Horizontal flow profiles for Favre averaged velocity (left) plus temperature and enthalpy (right). Black lines are for smooth case (SB2800-H) and grey for rough case (PB2800-H). Red and blue horizontal lines denote the peak roughness height on the hot and cold wall, respectively. ....	58
Figure 46: Horizontal flow profiles for the normal Favre averaged stresses for the smooth case (SB2800-H) and rough case (PB2800-H). ....	59
Figure 47: Vertical flow profiles for Favre averaged velocity (left) plus temperature and enthalpy (right). Black lines are for smooth case (SB2800-V) and grey for rough case (PB2800-V). Red and blue vertical lines denote the peak roughness height on the hot and cold wall, respectively. ....	59
Figure 48: Vertical flow profile for the normal Favre averaged cases for the smooth case (SB2800-V) and rough case (PB2800-V).....	59
Figure 49: Geometry sketch .....	62
Figure 50: Mean temperature, Air L .....	67
Figure 51: Mean temperature Air H .....	67
Figure 52: Vertical profile of the mean temperature; .....	69

## Related documents

-

## 1 Introduction

The ECC-SMART project aims to define the design requirements for Small Modular Reactors (SMRs) based on Supercritical Water Reactor (SCWR) technology. The SCWR, an innovative Generation IV reactor concept (see the SCWR page on the GIF website), has primarily focused on large-scale reactors over the past few decades. Reviews of these SCWR concepts have been documented in the literature and national projects (see Piro and Duffey, 2007; Oka et al., 2010; Schulenberg and Starflinger, 2012) and in IAEA technical documents resulting from Coordinated Research Projects (IAEA 2014; IAEA 2019a; IAEA 2020a). Recently, SMRs have gained significant attention within the nuclear community due to their potential advantages (IAEA 2020b). Their lower power levels could reduce the consequences and likelihood of severe accidents. Additionally, the modularity of SMRs, allowing partial construction in workshops and on-site assembly, could reduce economic risks and offer greater flexibility in adapting to future electrical grids dominated by renewable energy sources. These benefits align well with the inherent advantages of SCWR technology, such as higher core outlet temperatures compared to current Light Water Reactors (LWRs), leading to increased energy conversion efficiencies (see Piro and Duffey, 2007; Schulenberg and Starflinger, 2012). Moreover, the more compact design, enabled by a direct cycle, promises to reduce overall plant costs.

Work package three (WP3) is focused on thermal-hydraulic investigations related to the design and safety of the SCW-SMR. The knowledge and experience gained from these developments will support the design specifications and optimizing the SCW-SMR proposed in this project.

Main Objectives of WP3:

- Building on the existing results and experience, the first objective of this work package is to conduct further system design analysis and develop a joint design requirement document. This document will serve as the foundation for future conceptual design efforts.
- Surface-Coolant Interaction and Corrosion Prediction: The second objective is to analyse and model the interaction between the surface and coolant to predict corrosion under supercritical water conditions. Corrosion is a critical challenge identified within the Generation IV Supercritical Water-Cooled Reactor (SCWR) framework. Accurately predicting corrosion rates under both nominal operating and upset conditions is essential. This work package will generate new experimental data and direct numerical simulations (DNS) of turbulent heat and mass transfer along corroded surfaces. This will include leveraging proven methods for predicting rough surface behaviour using accurate RANS turbulence models. The resulting extended database will be used to analyse, develop, and validate models for turbulent heat and mass transfer in both corroded and non-corroded environments. This objective is closely linked with WP2.
- Thermal-Hydraulic Phenomena Investigation: The third objective is to conduct numerical and experimental investigations of thermal-hydraulic phenomena relevant to the safety and feasibility of the SCW-SMR. This includes developing and refining numerical tools used in engineering environments. Specifically, the focus will be on fast transients (such as those occurring in Loss of Coolant Accident (LOCA) conditions), improving heat transfer correlations for system codes, and enhancing and validating turbulence heat transfer models for Computational Fluid Dynamics (CFD) codes.

The overarching goal of this work package is to enhance and provide the scientific foundation necessary for the design and safety demonstration of the SCW-SMR concept.

D3.1 Report summarizing the newly generated reference data for natural convection, forced and mixed convection and decay heat removal

Within WP3, Task 3.2, "Reference Database," focuses on assembling existing and generating new data for thermal-hydraulic investigations. One focus of this task is to provide new data for turbulent flow and heat transfer in corroded environments. The research is performed in close cooperation with the WP2, dedicated to nuclear materials, to provide new data and increase knowledge on corrosion impact to heat transfer under supercritical pressure conditions. This work supports the design and safety research and development for SCW-SMR. Task 3.2 includes the following sub-tasks:

**3.2.1** Experimental investigations of turbulent heat transfer along corroded surfaces (KIT)

**3.2.2** Experimental investigations of turbulent flows along corroded surface (CNL)

**3.2.3** Exposure of experimental specimens (CVR)

**3.2.4** Direct numerical simulations (DNS) of flow over rough surfaces (USFD)

**3.2.5** DNS of turbulent heat transfer under supercritical pressure conditions (KIT)

**3.2.6** Assembling the existing experimental database (IPP)

This report summarizes the activities within Task 3.2 on assembling existing and generating new data for thermal-hydraulic investigations.

## 2 Experimental investigations of turbulent heat transfer along corroded surfaces (KIT)

The focus of this sub-task (3.2.1) is the experimental investigation of the effect of wall roughness on heat transfer. Currently, only a few experimental investigations are available in literature, in which irregular rough surfaces have been used. Among those, the work of Toubia and McFadden, 1966, in which water was used as coolant fluid, should be mentioned. In this experiment, the surface roughness was not the scope of the investigation but Copping and Yaras, 2022, have estimated the relative roughness to be  $k/d_h=7*10^{-4}$ . Herkenrath, 1967, performed experiments in similar conditions, with a smooth surface. By comparison of the experimental results, Copping and Yaras have shown that the heat transfer is enhanced due to the roughness. Further, Tanaka et al., 1971, performed experiments with supercritical carbon dioxide in two different circular tubes, for which the roughness of  $0.2\mu\text{m}$  and  $14\mu\text{m}$  is reported, but no further description of the roughness is provided. The results show that surface roughness generally enhances the heat transfer and further, that the heat transfer deterioration is shifted to larger bulk enthalpies for the rough tube, but occurs more rapidly, compared to the smooth tube. Further, the authors conclude that the entrance effect runs short when the roughness is predominant. Furthermore, the experiments of Niino et al., 1979, using supercritical hydrogen as coolant, were performed in three different tubes, for which the mean roughness height  $R_a$  was reported with values of  $R_a=4.2\mu\text{m}$  characterized as “fully rough” and two “semi-rough” tubes ( $R_a=0.25, 0.55\mu\text{m}$ ). However, Niino et al. did not compare the results from the different test sections directly with each other, so no analysis of the effect of the roughness on the heat transfer was performed. Instead, the scope of the work is the comparison with existing empirical correlations. In a recently published experimental investigation by Chen et al., 2022, using supercritical pressure  $\text{CO}_2$ , 5 different tubes are used, with a roughness of  $1.5\mu\text{m}$  as a smooth reference and 10, 20, 30, and  $40\mu\text{m}$  as rough tubes. In this publication, there is no further description of the roughness value, except those values. Nevertheless, in this reference the focus is on the evaluation of the effect of the different wall roughness and the results are presented as direct comparisons between the different tubes. The heat transfer is generally enhanced with increasing roughness. Further, the critical heat load ( $q/G$ ) for heat transfer deterioration increases with increasing roughness, with decreasing maximum peak temperatures at the same time. Further, it is stated, that the predictions of existing heat transfer correlations are insufficient for rough tubes and therefore, a new correlation with an additional roughness term is proposed.

The experiments in the present investigation are conducted in a smooth tube, as a reference, and in a rough tube. The newly generated database enables the community to further study the effect of the surface roughness on the heat transfer to fluids at supercritical pressure conditions.

### 2.1 Performed work and goals

In WP 2, autoclave experiments are performed at temperature and pressure conditions corresponding to the expected working conditions in the reactor core of a SCW-SMR. The oxide layer which grows on the specimen is analyzed by the project partners in WP2. The oxidated surface of the specimen shows only a very small roughness, which would not have any effect on the heat transfer. In such autoclave experiments, only a very small mass flow rate is achieved, to maintain the water chemistry at the desired parameters. This is different from the conditions in a real nuclear reactor, where a large mass flow is required to remove the heat produced by the heating rods. Under real reactor conditions, the wall shear stress acting on the corroded layer causes further damage to the surface of the fuel cladding (flow accelerated corrosion). To take

D3.1 Report summarizing the newly generated reference data for natural convection, forced and mixed convection and decay heat removal

this into account, a test tube with an increased surface roughness was manufactured by CVR within the Subtask 3.2.3. In this work, experiments are firstly conducted with a simple tube with surface roughness, as received from the manufacturer. Then, experiments are repeated, using the test tube with the higher wall roughness. The obtained experimental database can be used to study the effect of the wall roughness on the heat transfer coefficient.

## 2.2 Experimental setup and methodology

In this section, the experimental facility and in special the design of the test section, the experimental procedure and further the parameter range is described. Also, the measurement devices are described, and the uncertainty range of all devices is given.

## 2.3 KIT Model Fluid Facility – KIMOF

The KIMOF facility is a closed loop with a forced circulation of the coolant freon R134a. A scheme of the facility is shown in Figure 1. At the KOMIF facility, up to 3 test sections, such as simple tubes, annuli or even rod bundles can be installed. The circulation of the flow is driven by a coolant pump. The flow rate, which is measured by a Coriolis flowmeter, can be controlled by a process valve. Downstream of the outlet of the test sections a pressurizer is connected to the loop to control the pressure in the system. The KIMOF facility is designed for a maximum pressure of 50 bar and a maximum temperature of 250 °C.

The inlet temperature of the fluid into the test sections can be controlled by two pre-heating systems. One is an electrical continuous flow-heater. For lower mass flow rates, inlet temperatures of up to 95 °C can be reached. For larger mass flow rates, a second pre-heating system, which consists of a heat exchanger with water in the secondary loop can be used. The water in the secondary loop of the pre-heater is heated up by a gas burner. To buffer the impact of the gas burner on the pre-heating power, a 500 liters storage tank is installed. The temperature in the storage tank is maintained on a defined level, using the gas burner. Further, the flow rate of the water hot water from the storage tank through the secondary site of the heat exchanger is controlled by a valve.

The heat introduced to the fluid during the experiments is removed by a cooling tower. For large experimental heat fluxes, also a cooling machine can be used. Further, with the cooling machine it is possible to achieve inlet temperatures smaller than the ambient temperature.

The data is acquired, using 5 data loggers from FLUKE (2640A), which are connected to a PC with LABVIEW. The experimental parameters are controlled by WAGO programmable logic controllers.

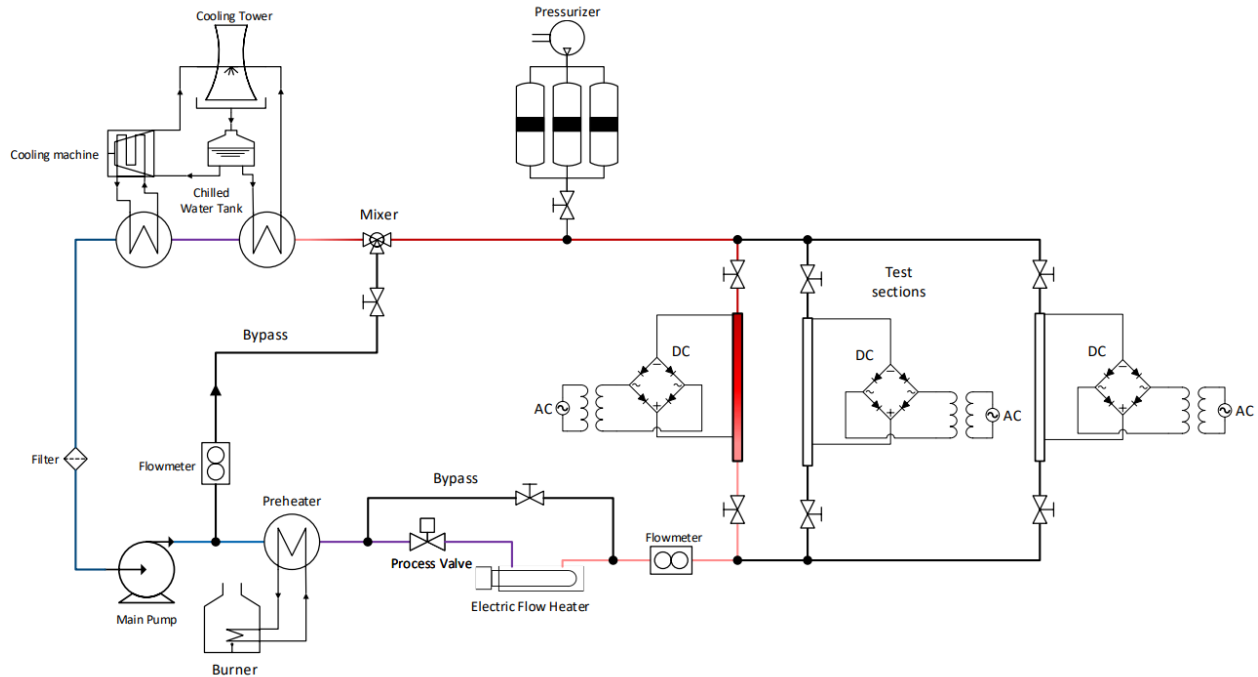


Figure 1: Scheme of the KIMOF test facility

## 2.4 Test section

In this investigation, a simple tube, which is directly heated by electrical DC current is used as test section. A scheme of the test tube can be seen on Figure 2. The inner diameter of the tube is 9 mm, and the wall thickness is 1.5 mm. The heated section has a length of 2800 mm and starts after 700 mm (78 hydraulic diameters of the tube), to achieve fully developed turbulent flow. The tube is manufactured from stainless steel 1.4571 (316Ti) and was delivered by the Sandvik Group. The flow direction is upwards. Two insulation flanges are used for electrical insulation of the test section. The inlet and the outlet temperature of the flow is measured using sheathed thermocouples of type T. The inlet and the outlet pressure are measured by pressure sensors. At the connectors, the voltage drop is measured, to determine the heat flux. For measurement of the heat transfer coefficient, 68 thermocouples of type T are mounted on the outside of the tube. The spacing in between the thermocouples is 45 mm (5 hydraulic diameters). The distance of the first and last thermocouple from the connectors is 50 mm, respectively. The thermocouples are mounted alternating at opposite sides of the tube (referred as 'left' and 'right' in the proposed database). At 4 levels there are 2 thermocouples on the same height and at one level in the middle of the tube there are 4 thermocouples in the same height ('left', 'right', 'front' and 'back' in the database). To minimize the heat loss to the environment, the tube is covered by 50 mm thick mineral wool.

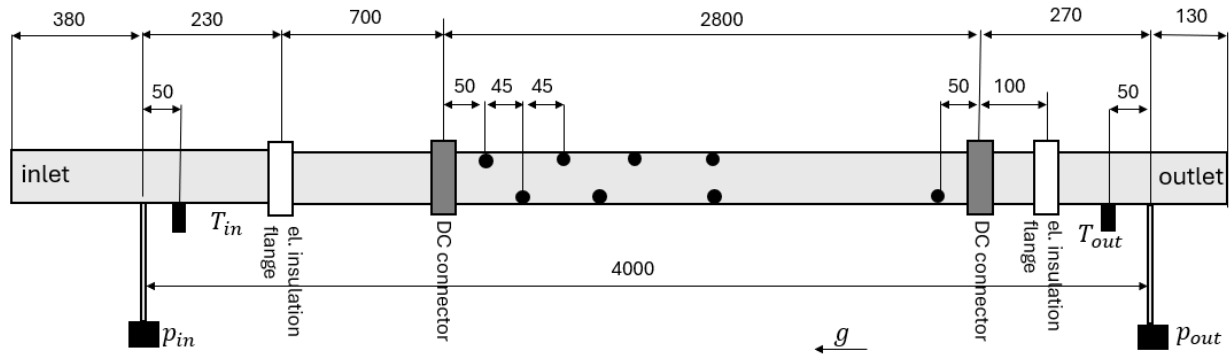


Figure 2: Schematic view of the test section

## 2.5 Wall roughness of the different test tubes

An oxide layer on a steel tube has an irregular shape. There are several different quantities to describe such an irregular roughness profile. The most relevant ones are the mean roughness height  $R_a$ , the maximum roughness height  $R_z$ , the root mean squared roughness height  $R_q$  and the skewness of the roughness profile  $s_k$ .

$$R_a = \frac{1}{n} \sum_{i=0}^n |y_i| \quad 2.1$$

$$R_z = \max(y_i) - \min(|y_i|) \quad 2.2$$

$$R_q = \sqrt{\frac{1}{n} \sum_{i=0}^n y_i^2} \quad 2.3$$

$$s_k = \frac{1}{nR_q^3} \sum_{i=0}^n y_i^3 \quad 2.4$$

The roughness of the tubes is measured by the CVR, using contact and non-contact profilometer (described in details in 4.1.4.). An identical tube was, as received from the manufacturer, cut and the roughness was measured along 6 lines. Figure 3 shows the measured roughness parameters along the 6 lines for the smooth tube.

Table 2-1: Roughness parameters of the smooth test tube

Line	$R_a$	$R_z$	$R_q$	$s_k$
	[ $\mu\text{m}$ ]	[ $\mu\text{m}$ ]	[ $\mu\text{m}$ ]	[-]
1	0.194	1.507	0.252	-0.724
2	0.29	2.024	0.371	-0.791
3	0.334	2.132	0.416	-1.038
4	0.301	5.258	0.575	2.495
5	0.231	3.709	0.424	2.129
6	0.207	1.964	0.281	-1.357

For the rough tube, two tubes were produced with the exact same manufacturing parameters and artificially treated inner surface. To achieve the rough surface, several methods such as

D3.1 Report summarizing the newly generated reference data for natural convection, forced and mixed convection and decay heat removal

electropolishing, mechanical sanding, shot-peening and chemical treatment were tested and evaluated. More details on this can be found in (Vit J. et al, 2025). It was found out that to achieve rough surface corresponding to  $R_a \approx 4 \mu\text{m}$ , combined method of mechanical and chemical treatment has to be applied. This surface treatment involved a combination of inner mechanical rotary grinding followed by etching with concentrated hydrochloric acid (35 % HCl) for 48 h. The mechanical treatment utilized simultaneous rapid rotation of the specimen at 1400 RPMs and linear movement (23 cm/min) of the inner grinding needle (H3 roughness class) along the entire length of the specimen. For this purpose, a bench for rotary grinding was developed and built to ensure homogeneous treatment of inner surface tube specimens longer than 4 meters. Two tubes/specimens with 4m length were produced by CVR. One tube was used for experiment described in this chapter 2. The second tube was cut at 6 different locations, according to Figure Figure 3. At each of the 6 locations, the roughness is measurement is performed 3 times. The results are shown in Table 2-2.

Table 2-2: Roughness parameters of the rough test tube.

LINE	$R_a$ [ $\mu\text{m}$ ]	$R_z$ [ $\mu\text{m}$ ]	$R_q$ [ $\mu\text{m}$ ]	$s_k$ [-]
1-1	3.417	24.253	4.357	-0.365
1-2	3.482	22.745	3.308	-0.395
1-3	3.34	20.312	3.816	-0.198
2-1	3.507	20.932	4.193	-0.262
2-2	3.203	19.784	3.839	-0.294
2-3	3.941	20.315	3.941	-0.103
3-1	4.097	25.565	5.082	-0.247
3-2	4.168	24.64	5.288	-0.304
3-3	4.103	23.878	4.813	-0.34
4-1	3.423	22.561	4.141	-0.289
4-2	3.65	27.765	4.655	-0.348
4-3	3.356	23.243	4.215	-0.555
5-1	3.597	22.367	4.521	-0.381
5-2	3.082	19.922	3.691	-0.301
5-3	3.404	26.628	4.757	-0.696
6-1	2.832	24.084	3.844	-0.615
6-2	2.734	16.035	3.471	-0.332
6-3	3.212	19.492	3.879	-0.282

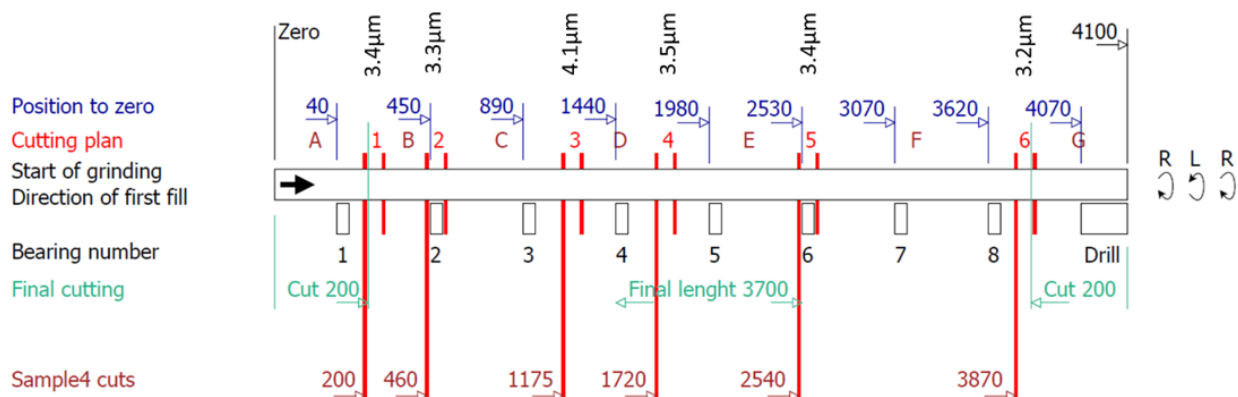


Figure 3: Cutting of the rough tube.

## 2.6 Measurement devices

### 2.6.1 Thermocouples for wall temperature measurement

The thermocouples used to measure the wall temperature are of type T, class 1 and have a measurement uncertainty of max (+/- 0.5 K, 0.4%). The diameter of the thermo-wires is 0.2 mm. Since the test section is heated by electrical current, electrical insulation of the TC measurement tips from the heated tube is required. To achieve that, one layer of self-adhesive fiberglass tape is applied on the tube. Then the thermocouples are mounted on the tube, using self-adhesive fiberglass tape. On the left of Figure 4 a picture of a mounted thermocouple is shown. On the right, the principle of the application of the thermocouples is shown schematically.

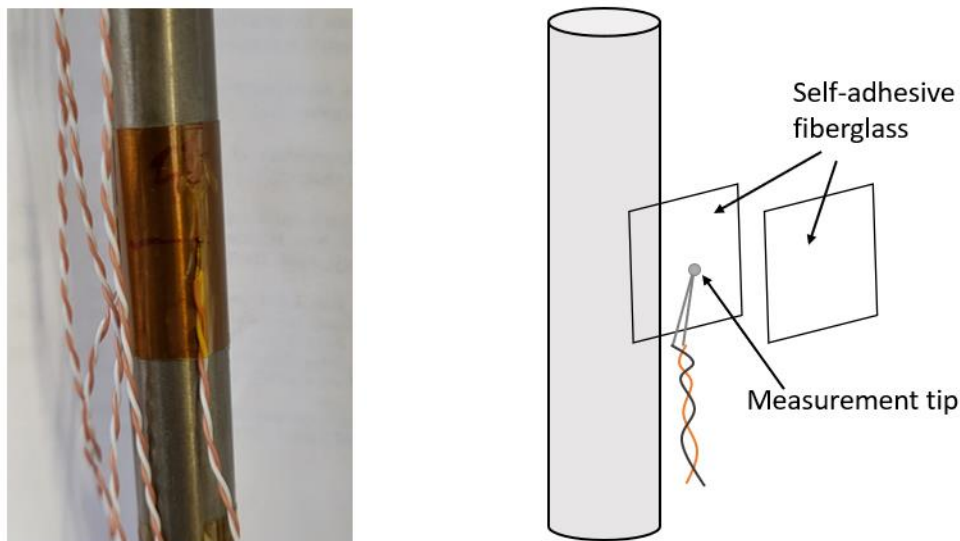


Figure 4: Mounted thermocouples for wall temperature measurement

### 2.6.2 Thermocouples inlet and outlet temperature

The thermocouples for measurement of inlet and outlet temperature protrude into the center of the test tube, as visualized schematically in the above figure. Since the flow passes several bends of the tubing on the way from the pre-heaters to the inlet of the test section, the flow can be considered as fully mixed, and the temperature profile is homogeneous. Also, the outlet temperature is homogenous. The thermocouples are the sheathed thermoelements 12-T-100-321-1,5-2I-3P6, which are of the type T and class 2 and have a measurement uncertainty of max (+/- 1 K, 0.75%). A 1/8" compression fitting is used to put the thermocouples in the center of the flow inside the tube. A clamping ring in the compression fitting provides the sealing.

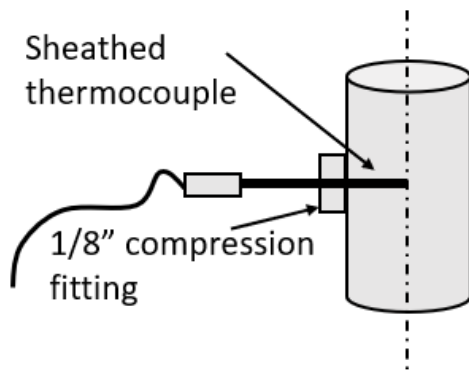


Figure 5: Scheme of thermocouples for inlet and outlet temperature

### 2.6.3 Pressure sensors

The pressure sensors for inlet and outlet pressure measurements are the PAA-33X from Keller. The measurement range of the sensors is 0...60 bar and the absolute pressure is measured. The analog channel is used, which has a measurement uncertainty of 0.1% of the measurement range, which is 0.06 bar. Since the pressure measurement is sensitive to the temperature, which is present at the transducer, the applied PAA-33X transducers are compensated for the temperature within a temperature range of 10...40 °C. To make sure, that the temperature at the transducers is always in the temperature compensated range, a coiled tubing is mounted onto the test tube and at the end of the coiled tube the pressure transducer is installed. Figure 5 the coiled tubing with the pressure transducer.

The pressure transducers have been calibrated by the manufacturer. The calibration protocells are considered in the data acquisition procedure. The sensors are measuring the voltage. The linear function from which the corresponding pressure is calculated includes the results of the calibration.

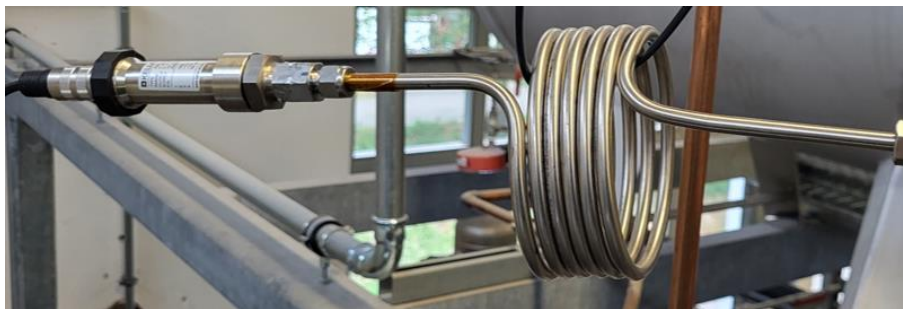


Figure 6: Coiled tubing and pressure transducer.

### 2.6.4 Flow meter

The Coriolis flow meter which is used to measure the mass flow rate through the test section is the RCUS34S-20TG90-0C6A-NN00-4-JA1/L005 from YOKOGAWA Deutschland GmbH. The mass flow rate is measured with an uncertainty of at most 0.15%.

## 2.6.5 Heat power measurement

Parallel to the electric power supply, the voltage is measured using an input channel of the fluke data logger 2640A. The electrical current is directly measured by the power supply. From the measured values, the heat flux can be calculated.

## 2.6.6 Uncertainty of measurement devices

Table 2-3 gives an overview of the uncertainties of all measurement devices and relevant geometry parameters.

Table 2-3: Uncertainty of measurement devices

Parameter	Uncertainty
Fluid temperatures	max (1K, 0.75% of measured in °C)
Wall temperatures	Max (0.5K, 0.4% of measured in °C)
Pressure	0.1% (of full sensor range)
Flow rate	0.15 %
Datalogger voltage	0.03 %
Datalogger temperature	0.5 K
Current	1.5%
Length	0.5 mm
Tube inner diameter	0.03 mm

## 2.7 Heat loss

Further, heat loss must be considered. The heat loss is driven by the temperature difference of the test section to the ambient. To determine a polynomial which describes the heat loss as a function of the temperature difference, the test section was evacuated, and a vacuum was created inside of it. Due to the vacuum in the test section, all the heat which is applied on the test tube needs to be released to the environment and no natural convection can transport the heat in the tube. A small heat flux was applied to the test tube. Once the temperature of the test section reaches a steady state, the heat which is generated by the electrical power equals the heat which is released to the ambient. Once the steady state condition is reached, the temperatures, as well as the ambient temperature and the heating power (current and voltage) are measured. Then, the procedure is repeated for larger heat fluxes, until the maximum possible wall temperature was reached. From the obtained values, a polynomial function of degree 2, which describes the heat loss as a function of the difference between the mean temperature of the test section and the ambient temperature was fitted. Figure 7 shows the recorded heat loss experiments and the polynomial fit.

$$\dot{Q}_v = 0.00063091(T_{w,m} - T_{env})^2 + 0.26959(T_{w,m} - T_{env}) - 0.31 \quad 2.5$$

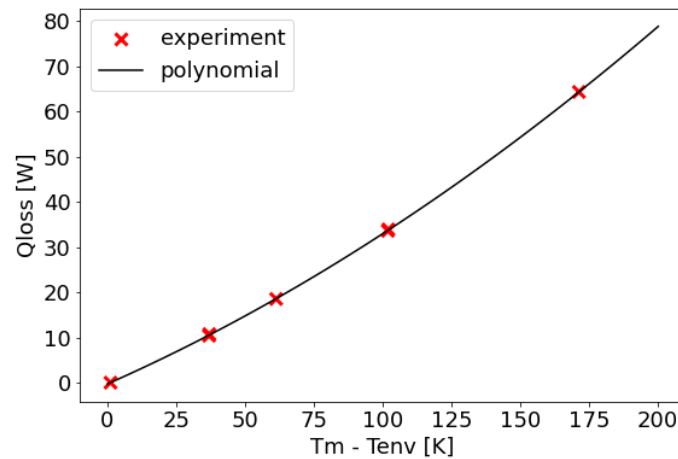


Figure 7: Heat loss experiment and polynomial fitting

## 2.8 Test procedure and parameter range

The experiments are conducted at steady state flow conditions and for each set of boundary conditions, data is collected for 60s, with a frequency of 2 Hz. Hence, 120 values are obtained for each measurement device. The pressure is the first parameter which is set and will be kept constant for a whole experimental day, since transients in pressure are shortening the lifetime of the components of the facility. Once the desired pressure is reached, the mass flow rate which is required is set. Following that, the desired inlet temperature is adjusted. To reach the desired inlet temperature is the most time consuming, while the heat flux can be adjusted in a relatively short time. Hence, the pressure, the mass flux and the inlet temperature are kept constant, and the heat flux is increased, starting from the lowest one. Once a set of desired boundary conditions is reached, the facility is held at steady state conditions for at least 15 minutes, to make sure that the flow is temporally fully developed. Then the data is acquired. After that, the heat flux is adjusted to the next higher one. When the measurement at the largest heat flux of the parameter set is finished, the next higher inlet temperature is set, and the heat flux is reduced to the smallest one in the matrix in the meantime. The full set of experimental parameters is shown in Table 2-4. The experiments are first performed using the smooth tube and all the cases in the matrix are repeated, using the tube with the rough inner wall.

The pressure range is chosen according to the fluid-to-fluid scaling model of Cheng et al., 2011. According to the model, a pressure of 46 bar in freon corresponds to 250 bar in water, which is the pressure in the proposed reactor design of Schulenberg and Otic 2022, which is discussed thoroughly within the ECC-SMART project. Additionally, a lower pressure of 43.5 bar is chosen, which is closer to the critical pressure of R134a (40.59 bar).

Table 2-4: Ranges of experimental parameters

$p$ [bar]	$T_{in}$ [°C]	$G$ [ $\frac{kg}{m^2s}$ ]	$q$ [ $\frac{kW}{m^2}$ ]
43.5 46	50,	500	20 – 70
	60,	750	30 – 75
	70,	1000	40 – 130

	80	1250	50 – 150
		1500	60 – 180
		1750	70 – 190
		2000	80 – 200

At this lower pressure conditions, the variation of the thermophysical properties of the coolant is much stronger, hence effects like the deterioration of the heat transfer are also more likely to appear more intensively. The pseudocritical temperature of R134a at 43.5 and 46 bar is 104.53°C and 107.42 °C, respectively. Hence, the fluid is subcooled at the inlet for all the experimental conditions. However, for many of the experimental cases, the outlet temperature exceeds the pseudocritical temperature. A roughness effect on the heat transfer is most likely to appear for large Reynolds numbers, when the thickness of the boundary layer is small. Therefore, the experimental conditions cover mass fluxes of up to 2000 kg/m<sup>2</sup>s. The steps for the mass flux are chosen to be 250 kg/m<sup>2</sup>s. In that way, the onset of roughness effects on the turbulent heat transfer can be captured. The minimum mass flux of 500 kg/m<sup>2</sup>s is close to the lower limit of the test facility. For lower mass fluxes, it becomes very hard to achieve steady state operating conditions in the test facility. The heat flux varies for all cases from a relatively small value, where normal heat transfer conditions appear, since the thermophysical properties do not show strong variations, to larger heat fluxes, where string variation of thermophysical properties appear. For  $G = 500 \text{ kg/m}^2\text{s}$  and  $G = 750 \text{ kg/m}^2\text{s}$ , the heat flux is increased by steps of 5 kW/m<sup>2</sup>, for all the other cases, the step is 10 kW/m<sup>2</sup>. The maximum of the applied heat fluxes is defined by the limitations of the measurement devices and the maximum possible operating temperature of R134a (250 °C) and some safety margin to that value. In total, 312 combinations of experimental parameters are obtained in each of the test tubes.

## 2.9 The reference database

The newly generated reference database is shared with the project partners in the ECC-SMART SharePoint. Since the choice of the thermophysical property library has an impact on the calculated parameters, the data is released in its original form, just with quantities which are measured in the experiment. This is the mass flow rate, the electrical current and the voltage, the inlet pressure, the outlet pressure, the inlet temperature, and the outlet temperature as well as the wall temperatures measured on the outside of the test tubes. In that way, reference database for supercritical heat transfer at rough walls can be evaluated using updated versions of thermophysical properties, which may be available in the future. All required geometrical parameters of the test section, as well as uncertainties of the measurement devices can be found in this report.

The titles of the data in the database are summarized in Table 2-5.

Table 2-5: Titles in the experimental database

<i>Parameter</i>	<i>Title in database</i>	<i>Unit</i>
<i>TC-Name</i>	TC	-
<i>TC mounted at side of the tube</i>	location	-
<i>inlet pressure</i>	Pin	bar
<i>outlet pressure</i>	Pout	bar
<i>inlet Temperature</i>	Tin	°C
<i>outlet Temperature</i>	Tout	°C

D3.1 Report summarizing the newly generated reference data for natural convection, forced and mixed convection and decay heat removal

<i>mass flow rate</i>	m	kg/h
<i>electrical voltage</i>	U	V
<i>electrical current</i>	I	A
<i>outside wall temperature</i>	Tw_o	°C
<i>ambient temperature</i>	T amb	°C

## 2.10 Publications

The following publications have been made within the scope of the ECC-SMART project:

- 1) F. Wiltschko, X. Cheng, Experimental investigation of heat transfer to supercritical pressure R134a in circular tubes with rough surface, Kerntechnik 2024, June 11-13, Leipzig, Germany
- 2) F. Wiltschko, M. Sipova, J. Vit, X. Cheng, Experimental investigation of heat transfer to supercritical pressure R134a in artificially roughened tubes, 31st International Conference on Nuclear Engineering (ICONE31), 2024, August 4-8, Prague, Czech Republic.

### 3 Investigations of turbulent heat transfer along corroded surfaces (CNL)

#### 3.1 Background

The high temperatures and substantial variations in fluid density encountered in industrial applications involving supercritical water promote corrosion at solid surfaces. Initially smooth surfaces can become roughened over time through the formation of oxide layers and the deposit of foreign matter. Despite this reality, the heat transfer characteristics of supercritical water in the presence of naturally rough surfaces are not well understood. Here, the adoption of the term naturally rough is intended to identify surface topology characteristics which arise from stochastic processes; i.e. those surfaces in which the spacing and regularity of the perturbations are not generated in a controlled process. In their literature review, Copping and Yaras (2022) surveyed oxide layers that formed while being exposed to supercritical water in supercritical steam generators (SCSG) in power generation (e.g. SCWR) and in laboratory environments. The roughness heights reported in their review are converted to turbulence wall scales to facilitate comparisons against turbulence and heat transfer parameters. In turbulent wall-bounded flows, the wall scales correspond to viscous length and time scales and normalization with these scales is denoted with the “+” superscript. viscous length scale is defined as  $\nu/u_\tau$ , where  $\nu$  is the kinematic viscosity of the fluid and  $u_\tau$  is the friction velocity. The parameter  $u_\tau$  is defined as  $(\tau_w/\rho)^{1/2}$ , where  $\tau$  is the time-mean shear stress,  $\rho$  is the fluid density, and the  $w$  subscript indicates values evaluated at the wall. Copping and Yaras (2022) noted that these values vary through the heater in a SCSG and the reactor core of a SCWR due to the differences of the thermophysical properties of water between the inlet and the exit. Also, the value of the friction velocity differs between the SCSG and SCWR applications due to differences in flow Reynolds number and mass flux. These wall-scaled roughnesses correspond to the viscous sublayer ( $y^+ < \sim 5$ ) and the buffer layer ( $\sim 5 < y^+ < \sim 40$ ) of a turbulent boundary layer. In a few instances, the roughness elements are noted to extend past the buffer layer. Based on these observations, as a starting point for investigating the effects of surface roughness on heat transfer in channel flows of supercritical fluids, the present study focuses on surface roughness that is within the range of  $y^+ < 10$ .

As turbulence in the inner region of the boundary layer is critical to the convective heat transfer to/from the supercritical fluid, its accurate prediction is key to reliable predictions of this transport process. This turbulence can be significantly altered by high thermophysical property gradients that may develop when the working fluid is near its pseudocritical state, thereby contributing to the altered heat transfer phenomenon, which may develop in instances of heat transfer involving supercritical fluids (Azih and Yaras, 2018). Presence of surface roughness would affect near-wall turbulence both directly by defining the wall topology, and potentially indirectly by altering the local spatial distributions of thermophysical properties.

#### 3.2 Objective

The objective of this subtask is to produce data for turbulent heat transfer for flows of supercritical fluids along corroded surfaces. This was accomplished by review of literature (Copping and Yaras, 2022) to determine the range of corrosion induced roughness imposed on surfaces exposed to these conditions in experiments and industrial applications. Following this review, direct numerical simulations were performed for smooth and rough surfaces to understand the influence of roughness on turbulence at relevant roughness heights.

### 3.3 Investigations on smooth surface baseline cases at subcritical conditions

This section discusses simulations of flows in channels under subcritical conditions for smooth surfaces that serve as a baseline for comparison for the simulations at supercritical conditions.

#### 3.3.1 Test case

Direct numerical simulation is performed at an inflow Reynolds number of 12,000 based on the channel hydraulic diameter, mass flow rate, and bulk-fluid viscosity. The working fluid is water. The equivalent friction Reynolds number (friction velocity as the characteristic velocity) is 225. To simulate subcritical conditions, while still providing an adequate baseline for comparison against supercritical flows, the inlet condition is set above the critical pressure. However, the thermophysical properties are artificially fixed at this inlet condition so that upon heating, no spatial gradient of fluid properties exist within the domain. The inlet conditions and domain conditions are  $p/p_c = 1.085$  and  $T/T_{pc} = 0.983$ , respectively. Where, the subscripts  $c$  and  $pc$  refer to the critical and pseudocritical state, respectively. The domain comprises a rectangular channel with a height of  $45.4 \text{ mm} = 2\delta$ . Where,  $\delta$  is the half-height and characteristic length of the channel. As per Figure 8, The channel length is  $11.3\delta$  and the channel width is  $3.2\delta$ . A heat flux of  $25 \text{ kW/m}^2$  is applied to attain a ratio of wall heat flux to flow mass flux of  $3.0 \text{ kJ/kg}$ . Where  $Q$  is the heat flow, the  $\dot{\cdot}$  superscript indicates a time rate of change, the  $''$  superscript indicates an area flux, and the  $w$  subscript indicates values evaluated at the heated wall.

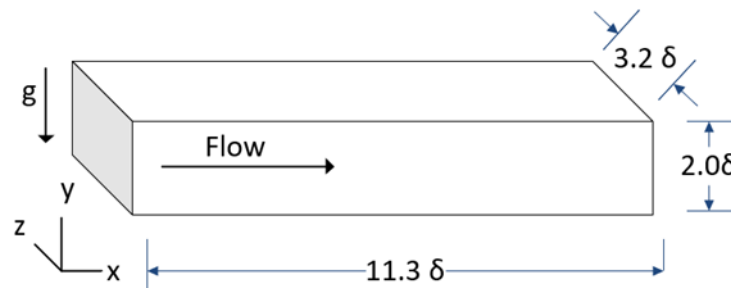


Figure 8: Illustration of the computational domain for the channel simulations

#### 3.3.2 Methodology

The inlet turbulence in these simulations come from the work of Azih and Yaras (2018). Although the length of the domain is somewhat short, it captures the behaviour of near wall turbulence adequately up to a wall-normal distance of  $0.6\delta$ . Above this wall-normal height, the turbulence development becomes affected by the domain length as there is not enough space for full development. In this study, the primary objective is to look at the change in turbulence due to changes in roughness. These changes are limited to the vicinity of the wall, so this domain is deemed sufficient.

Spanwise periodic boundaries are applied to the side wall and no-slip boundary conditions is applied to the upper and lower wall of the horizontally oriented channel. The outflow boundary is set to have an area-averaged pressure of  $p/p_c = 1.085$ .

D3.1 Report summarizing the newly generated reference data for natural convection, forced and mixed convection and decay heat removal

Structured grids with hexahedral cells are mapped onto the computational domain shown in Figure 8. The node distributions are selected to capture the smallest turbulence scales corresponding to the Kolmogorov scales and Batchelor scales. The nodes are uniformly spaced in the streamwise and spanwise directions. In the wall-normal directions the nodes are clustered towards the wall and dispersed in the region of the bulk flow. Near the wall, the grid spacing in the streamwise, wall-normal, and spanwise directions ( $x$ ,  $y$ , and  $z$ , respectively) are 5.0, 0.12, and 4.0 wall units. The range of wall-normal node spacing is 0.12 -3.02 wall units and the distribution is depicted in Figure 9.

A time step size of 0.013 is used and is dictated by the stability of the numerical method in the presence of the gradients in the thermophysical properties rather than the turbulence time scales.

Numerical integration of the compressible form of the Navier-Stokes equations without body forces is performed with versions 12 and 19 of the ANSYS CFX commercial computational fluid-dynamics software. The CFX algorithm utilizes an integral discretization formulation based on the finite-volume technique. For these simulations, spatial interpolations to determine the mass, momentum and energy fluxes at the control-volume faces are set to be equivalent to centred differencing in a finite difference formulation. Numerical integration in time is realized with second-order accurate Euler discretization. In each time step, the iterative algebraic-multigrid solution of the discretized governing equations using the incomplete lower-upper factorization technique is declared converged when the root mean-square (rms) of the finite-volume residuals of mass, momentum and energy is reduced to at least  $1 \times 10^{-5}$ . Relevant thermophysical properties are obtained via bilinear interpolation of the tabularized IAPWS equations of state for water (IAPWS, 2009), which are indexed by temperature and pressure.

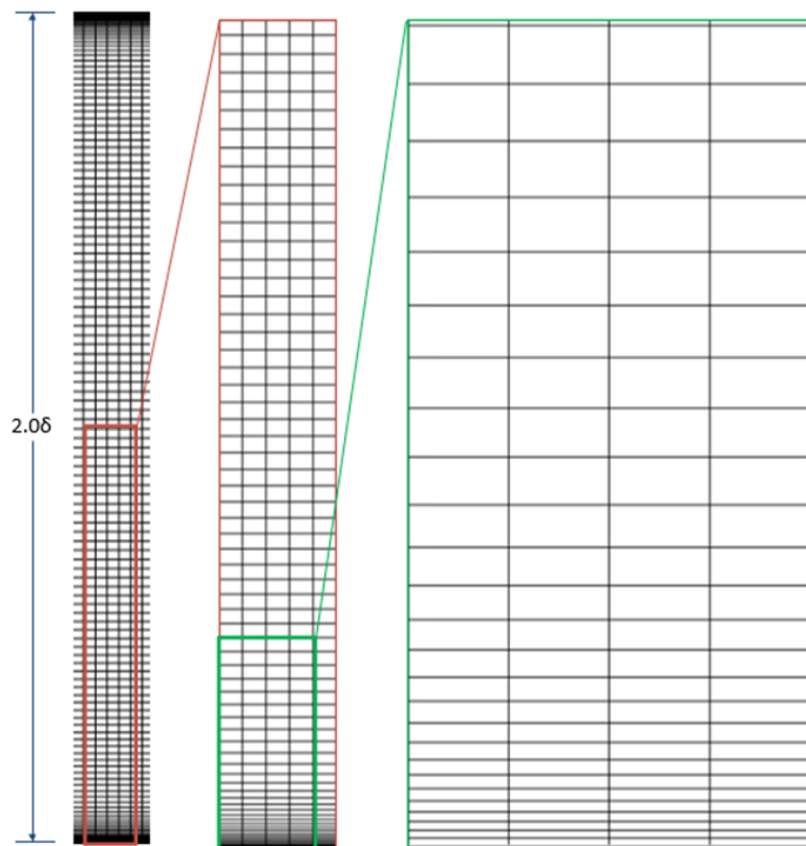


Figure 9 Wall-normal grid spacing for smooth wall simulations

### 3.3.3 Results and discussion

The simulations were partitioned and executed on 20 Intel™ L5410 Xeon processors. Approximately 1300 wall time units (100,000 timesteps) were required to reach a statistically steady state. The data from the baseline case is compared to published data to validate the computational methodology. The data also serves as a baseline for comparison for the test conditions at the supercritical state and with roughness as shown in Figure 10. Compared parameters are the mean velocity, root-mean-squared (rms) perturbation velocity components, turbulence production and dissipation rates, and temperature. Here, the mean identified with an overbar refers to averages taken along statistically homogeneous coordinates, which are the temporal and spanwise coordinates in the present study. The ' symbol indicates fluctuation components, and the velocity in the  $x$ ,  $y$  and  $z$  cartesian directions are  $u$ ,  $v$ , and  $w$ , respectively. The statistical turbulence properties compare very favourably with the DNS data of Abe et al. (2001) and Kim et al. (1987) and also agrees well with the hot-film experimental data of Eckelmann (1974), especially for  $y^+ < 60$ .

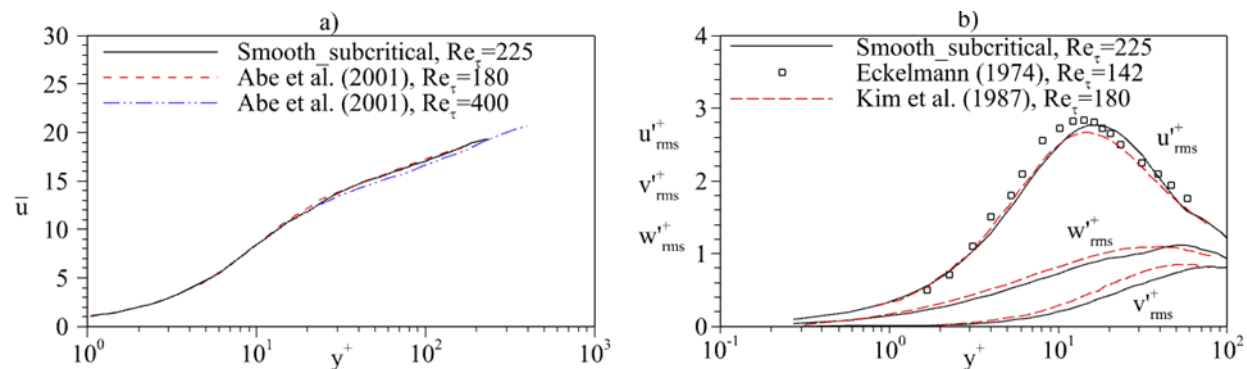


Figure 10 Mean flow properties evaluated at  $x\delta = 9$  for the smooth subcritical turbulent channel case: a) streamwise velocity component; b) root-mean-square of perturbation velocity components

Turbulence kinetic energy budgets (production, transport and dissipation) are compared against well-established trends through the data of Abe et al. (2000) in Figure 11. Very good agreement is obtained for the turbulence production, transport (pressure diffusion, turbulent advection, and viscous diffusion), and dissipations terms. This shows that the present method correctly models the kinetics of turbulent flows. For energy transport, further validation of the computational method is demonstrated by comparing the distribution of mean temperature at  $x\delta = 9$  to the results of Kawamura et al. (1998), and is shown in Figure 12. In Figure 12, the normalized temperature is used to define the ordinate. Figure 12 depicts favourable agreement in the inner part of the shear layer between the present simulation ( $Pr = 1.67$ ) and Kawamura et al.'s (1998) case corresponding to a  $Pr = 1.5$ . The fuller temperature profile in the outer part of the shear layer of Kawamura et al.'s (1998)  $Pr = 1.5$  case is expected due to the comparatively higher Reynolds number and Prandtl number of the present case as well as the present study's shorter domain resulting in a thermal profile that is not fully developed.

D3.1 Report summarizing the newly generated reference data for natural convection, forced and mixed convection and decay heat removal

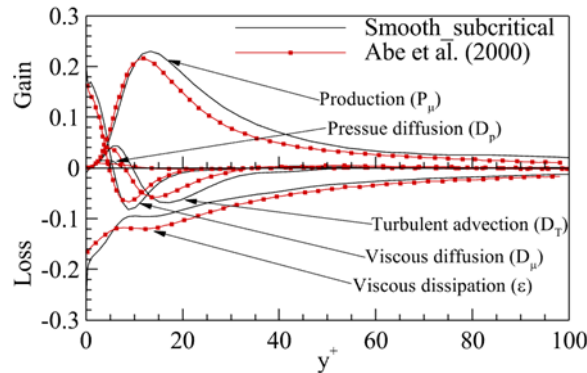


Figure 11 Specific rates of turbulence kinetic energy budgets evaluated at  $x\delta = 9$  smooth subcritical turbulent channel case

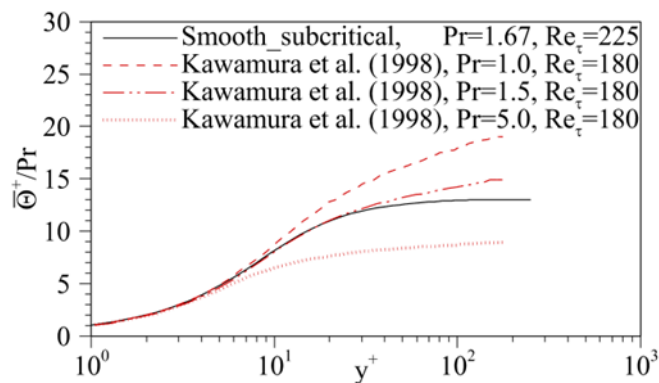


Figure 12 Mean temperature evaluated at  $x\delta = 9$  for the smooth subcritical turbulent channel case

### 3.4 Investigations on smooth surface baseline cases at supercritical conditions

This section discusses simulations of flows in channels under supercritical conditions for smooth surfaces that serve as a baseline for comparison for the simulations on rough surface conditions for horizontal flow.

#### 3.4.1 Test case

Using the computational domain in Figure 8, direct numerical simulation is performed at an inflow Reynolds number of 12,000 on horizontally flow in a channel. Since the fluid properties vary, the Reynolds number changes as the flow develops through the domain. In this case, the channel walls are uniformly heated at the same level as the baseline case with no thermophysical property gradients (Section 3.3.1) yielding wall-temperature values ranging from  $T_w < T_{pc}$  to  $T_w > T_{pc}$  along the length of the channel. In this simulation, a domain of unheated up stream flow is not considered, previous work by Azih and Yaras (2018) has shown that this can cause up to a 6% difference in the statistical properties obtained from the simulation. The fluid properties are allowed to vary in accordance with the International Association for the Properties of Water and Steam (IAPWS) equations of state (IAPWS, 2009).

#### 3.4.2 Methodology

The computational method discussed in Section 3.3.2 was followed. A gravitational acceleration value of  $9.81 \times 10^{-3} \text{ m/s}^2$  is specified and a no-slip boundary condition is specified at  $y = 0$  (lower

wall) and  $y = 2\delta$  (upper wall). The nodes are uniformly spaced in the streamwise and spanwise directions. In the wall-normal directions the nodes are clustered towards the wall and dispersed in the region of the bulk flow as was done for the baseline case. Since the wall shear is different on the lower and upper wall, two different normalized grid spacing are obtained. Near the wall, the grid spacing in the streamwise, wall-normal, and spanwise directions of the lower wall are 10.1, 0.24, and 8.0 wall units. Likewise, the grid spacing in the streamwise, wall-normal, and spanwise directions of the upper wall are 5.5, 0.13, and 4.4 wall units. The range of wall-normal node spacing is 0.24 -6.13 and 0.13 -3.33 wall units on the lower and upper walls, respectively.

### 3.4.3 Results and discussion

The streamwise velocity field normalized by wall units is shown in Figure 13 (a and c). Parameters are plotted separately for the lower and upper wall of the supercritical case. The value of the friction velocity is 0.00318 m/s on the lower wall and 0.00220 m/s on the upper wall. The value of the friction velocity for the subcritical case 0.00137 m/s. The velocity fluctuations normalized by wall units is shown in Figure 13 (b and d). In comparison to the subcritical case, the normalized fluctuations are noted to be larger in the upper half of the channel at  $x\delta = 9$ . For the lower wall the normalized fluctuations are larger than those of the subcritical case below  $y^+$  of 10. This means that for the present conditions, the near wall mixing is more intense in the supercritical cases at  $x\delta=9$ .

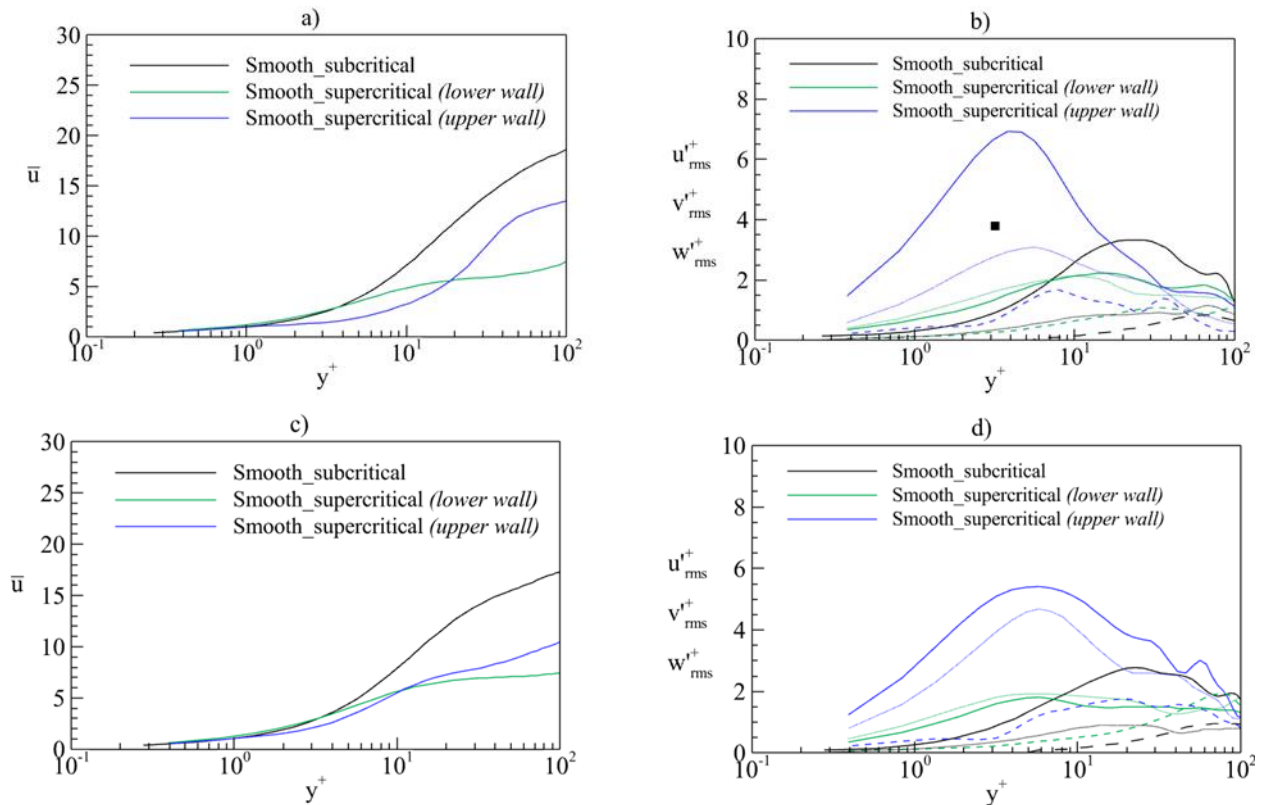


Figure 13 Mean flow properties evaluated at  $x\delta = 2$  (a and b) and  $x\delta = 9$  (c and d) for the smooth turbulent channel cases: a,c) streamwise velocity component; b,d) root-mean-square of perturbation velocity components, solid line is  $u$ , dashed is  $v$ , and dotted is  $w$ .

The turbulence kinetic energy (TKE) budgets of variable property flows differ significantly from the constat property flow. There are many additional terms from the Favre decomposed turbulence kinetic energy production and transport. The focus in this section will be on the TKE production and dissipation terms. There are two primary terms that contribute to TKE production:

1) TKE production from the mean shear ( $P_\mu$ ) and 2) TKE production from buoyancy forces ( $P_g$ ). These values are plotted in Figure 14. The  $\delta$  superscript indicates that the values are normalized by  $\delta$  and the inlet velocity. As expected, the gravitational production in the subcritical case is zero. On the lower wall, TKE production is supplemented by TKE production from buoyancy forces, however, even without production due to buoyancy forces, TKE production from the mean shear is enhanced compared to the subcritical case. For the upper wall, the overall production of TKE from the mean shear is negated by the mitigation of TKE by buoyancy forces. The additional TKE production in both cases is balanced by higher rates of TKE dissipation, however, both cases show higher net production of turbulence near the wall in comparison the subcritical case.

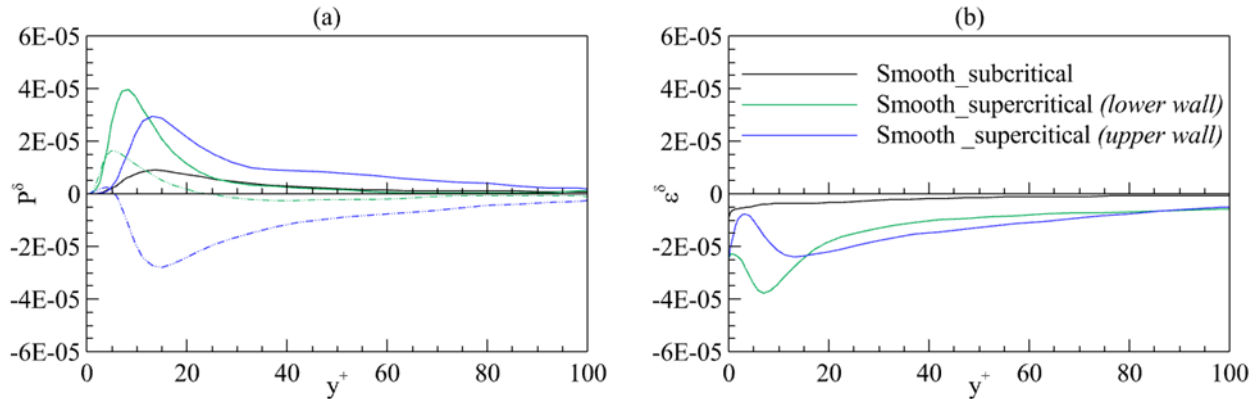


Figure 14 Turbulence kinetic energy budgets evaluated at  $x\delta = 9$  for the smooth turbulent channel cases: a) Production of TKE from mean shear (solid line) and from buoyancy (dash-dotted line); b) dissipation of TKE by the mean shear.

The temperature distribution in the flow and at the walls are shown in Figure 15. The working fluid is water at a nominal supercritical pressure of 24 MPa, a uniform inflow temperature of 643 K, and an outflow bulk temperature of 645.06 K. For 24 MPa, the pseudocritical temperature of water is 654.4 K. It is evident that the additional mixing due to increased turbulence in the supercritical cases results in lower temperatures at the wall in comparison to the subcritical case. On inspection of the streamwise temperature profile along the upper wall in Figure 15(b), a signature of deteriorated heat transfer is observed whereby the temperature profile does not monotonically increase, but has a local maximum at  $x_\delta = 2$ . Under this deteriorated condition, there is a sharp change in the slope of the normalized velocity profile at  $\sim y^+ = 50$ , depicted in Figure 15 (a).

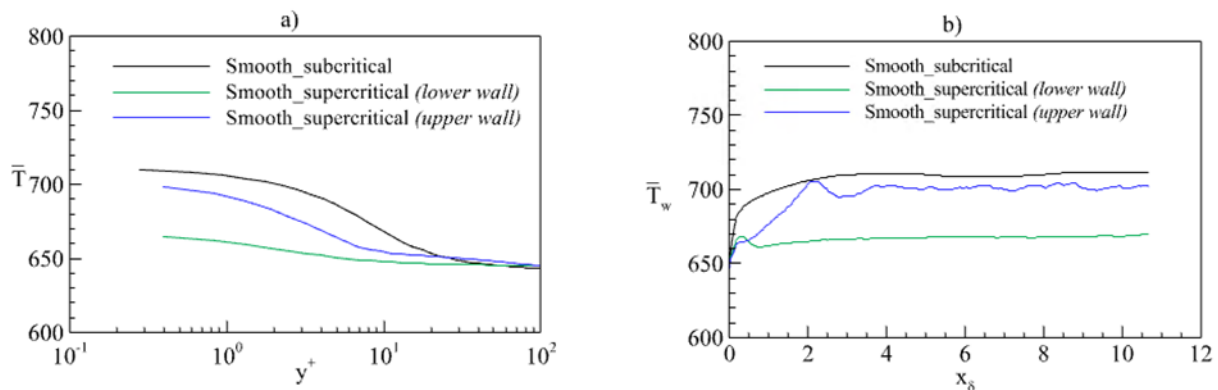


Figure 15 Temperature distribution for the smooth wall test cases at  $x\delta = 9$ . A) wall-normal temperature profile. b) streamwise temperature profile.

### 3.5 Investigations on rough surface baseline cases at subcritical conditions

This section investigates the effect of roughness on smooth surfaces at subcritical conditions. The goal is to determine the adequacy of the method used to simplify the boundary conditions that will be applied to the rough cases at supercritical conditions.

#### 3.5.1 Test cases

To enable investigation of the effect of surface roughness on the local thermal hydraulics through modification of the wall heat transfer pattern, with minimal additional effects associated with roughness-induced changes in surface drag and vorticity fields, the subcritical studies look at roughness patterns involving cube-shaped cavities arranged in streamwise rows and cube-shaped protrusions along the surface. The cavities and protrusions are chosen to be comparable to the thickness of the viscous sublayer of a turbulent boundary layer. The cavities have nominal dimensions of  $\sim 5$  wall units and the protrusions range from 5 to 9 wall units. The computational domain is shown in Figure 16. These cases are developed over a flat surface rather than a channel, as the goal is to determine the adequacy of the method used to simplify the boundary conditions that will be applied to the rough cases at supercritical conditions. Therefore, a free slip boundary condition is prescribed at the top of the computational domain. At the no-slip boundary at the bottom of the domain, the surface roughness is implemented as a patch that is spanwise centred in the domain and is placed at some distance from the leading edge of the plate. The streamwise location of the patch is chosen such that the size of the roughness elements is comparable to, or smaller than, the thickness of the viscous sublayer. The patch for the roughness pattern involving cavities contains three streamwise rows and five spanwise rows. These patch dimensions in terms of cavity count are found to be sufficient to obtain cavity-flow conditions at the centre of the patch that are not affected by the finite size of the patch. For the case involving protruding roughness elements, the primary interest is in the vorticity field associated with such protrusions and modification of the surface drag experienced by the boundary layer due to the presence of such protrusions. To account for the mutual interaction of protrusions in tandem and side-by-side settings, the chosen patch involves three protrusions configured as shown in Figure 16 (b).

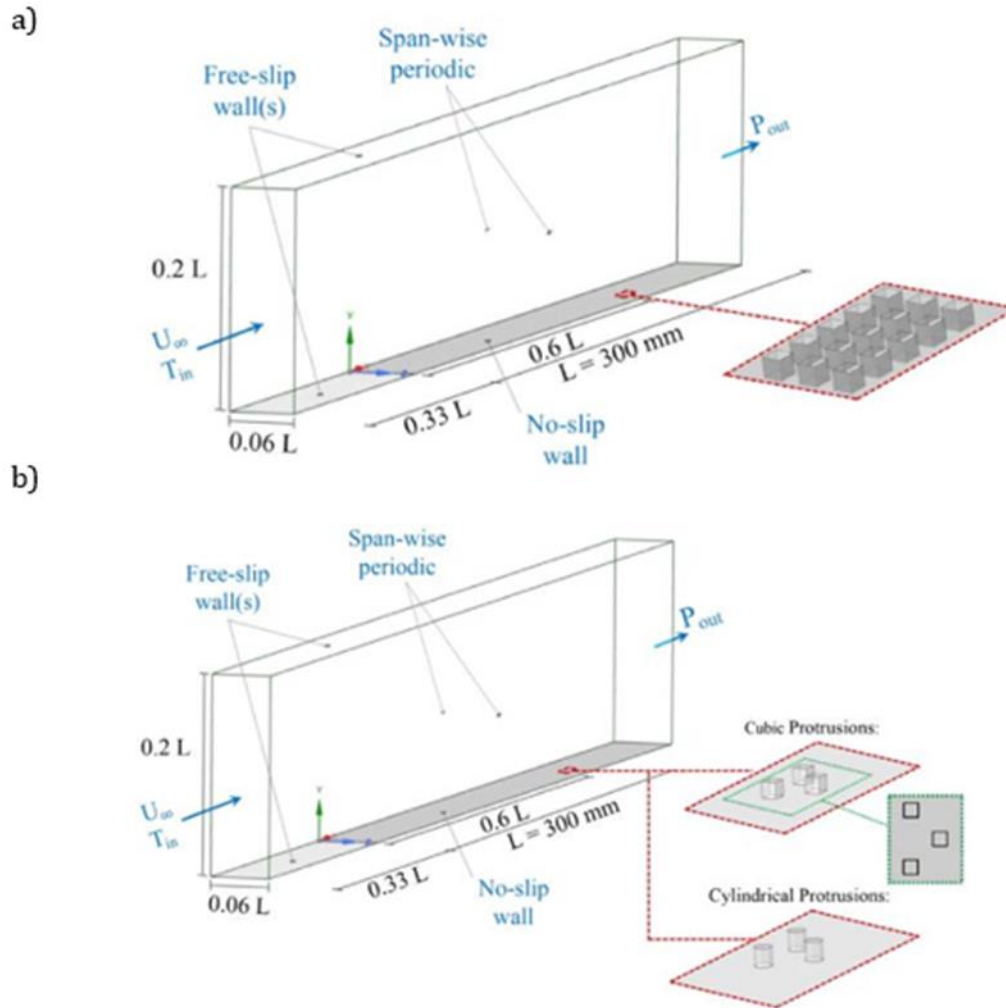


Figure 16 Computational domain and boundary conditions for the subcritical turbulent cases with a boundary layer: a) cavity-type surface roughness; b) protrusion-type surface roughness.

### 3.5.2 Methodology

A block-structured grid of hexahedral elements is mapped to the computational domain. The near-wall region ( $y^+ < 50$ ) has a considerably finer resolution in the streamwise and spanwise directions. The grid-node distribution region farther from the wall ( $y^+ > 50$ ) is also concentrated in the vicinity of the roughness patch in both the spanwise and streamwise directions. The total grid-node count in the grid block adjacent to the wall for the small cavity case and for the large cavity case, and in the coarser-grid block farther from the wall are 52.3 million, 41.5 million and 5 million, respectively. The grid is similar to the smooth wall case except in the vicinity of the roughness patches. Resolution of the grid around the roughness patches is depicted in Figure 17 and Figure 3-11. The grid in blue colour corresponds to the fluid domain. The grey-coloured grid is mapped into the solid medium of the plate through which heat is conducted. The conservative grid resolution in the solid medium with a total grid-node count of 1.9 million is chosen to accurately capture the temperature gradients within this medium.

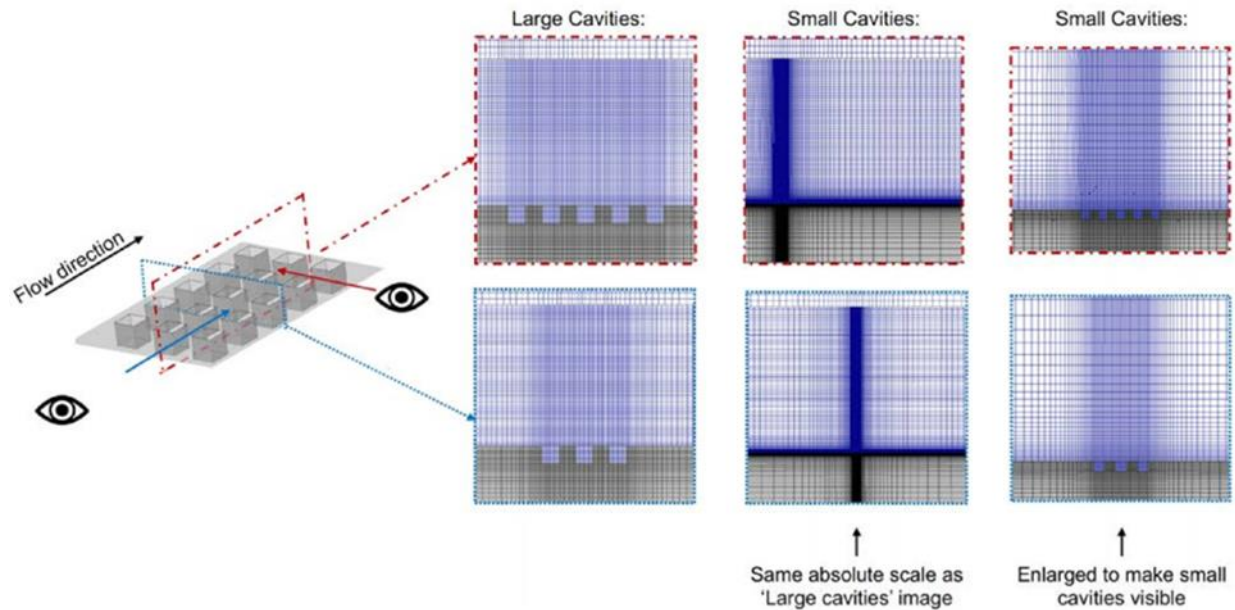


Figure 17 Mesh resolution for the cavity-type surface roughness.

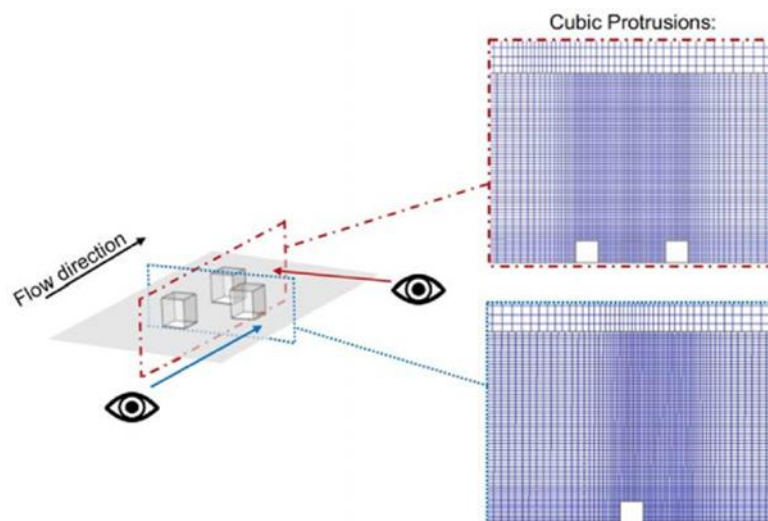


Figure 18 Mesh resolution for the protrusion-type surface roughness

### 3.5.3 Results and discussion

Figure 18 presents distributions of the instantaneous values of streamwise and wall-normal components of velocity in the same format. The time-averaged values are shown with a solid curve in these plots. Three moments in time are selected for this illustration, which correspond to a larger boundary-layer eddy convecting over the roughness patch. This transience would affect the convection mode of heat transfer within the cavity, which in turn would result in transience in the instantaneous rate of heat transfer at the cavity opening. Given this dominance of the conduction heat transfer mode within the cavities, the relative amplitudes of fluctuations in heat transfer rate at the cavity opening are expected to be considerably less than the relative amplitudes involved in the velocity-field transience. This observation forms the basis of a simplified thermal boundary condition for the rough cases at supercritical conditions.

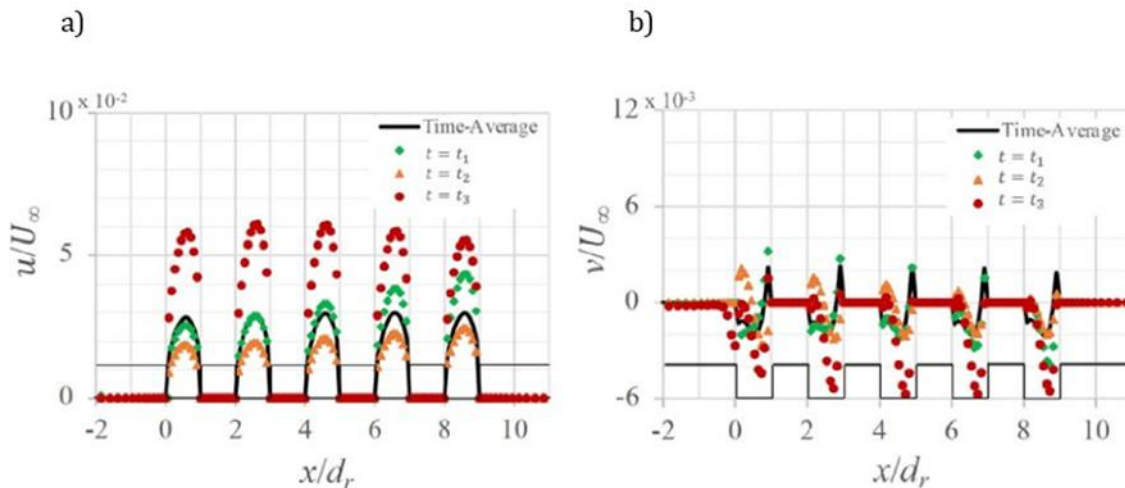


Figure 19 Distribution of instantaneous a) streamwise ( $u$ ) b) wall-normal ( $v$ ) component of velocity over the centre streamwise row at three wall-normal distances for the subcritical turbulent- boundary-layer over rough surfaces.

Results from the case with protrusions is shown in Figure 19. The fact that the vorticity field (shown in Figure 19) related to the presence of protrusions remains highly localized within a wall-normal region that is comparable to the height of the protrusion elements would suggest that direct interaction of the associated localized coherent vortices with the eddies of a turbulent boundary layer is unlikely.

The simulation results with cavity-type surface roughness and protrusions presented may provide an opportunity to simplify the wall boundary conditions for the study of heat transfer in channel flow of supercritical water. Given the very small magnitudes of wall-normal velocity observed at the cavity openings, it may be reasonable to set it to zero. As the simulations showed essentially no motion in the spanwise direction at the cavity openings, the  $z$  component of velocity,  $w$ , can also be set to zero at the cavity openings. The boundary conditions for mass and momentum conservation at the wall, implemented by constraining the flow velocity at the wall, can then be imposed at the  $y = 0$  plane through specification of the spatial distribution for the  $x$  component of velocity,  $u(x,z)$ .

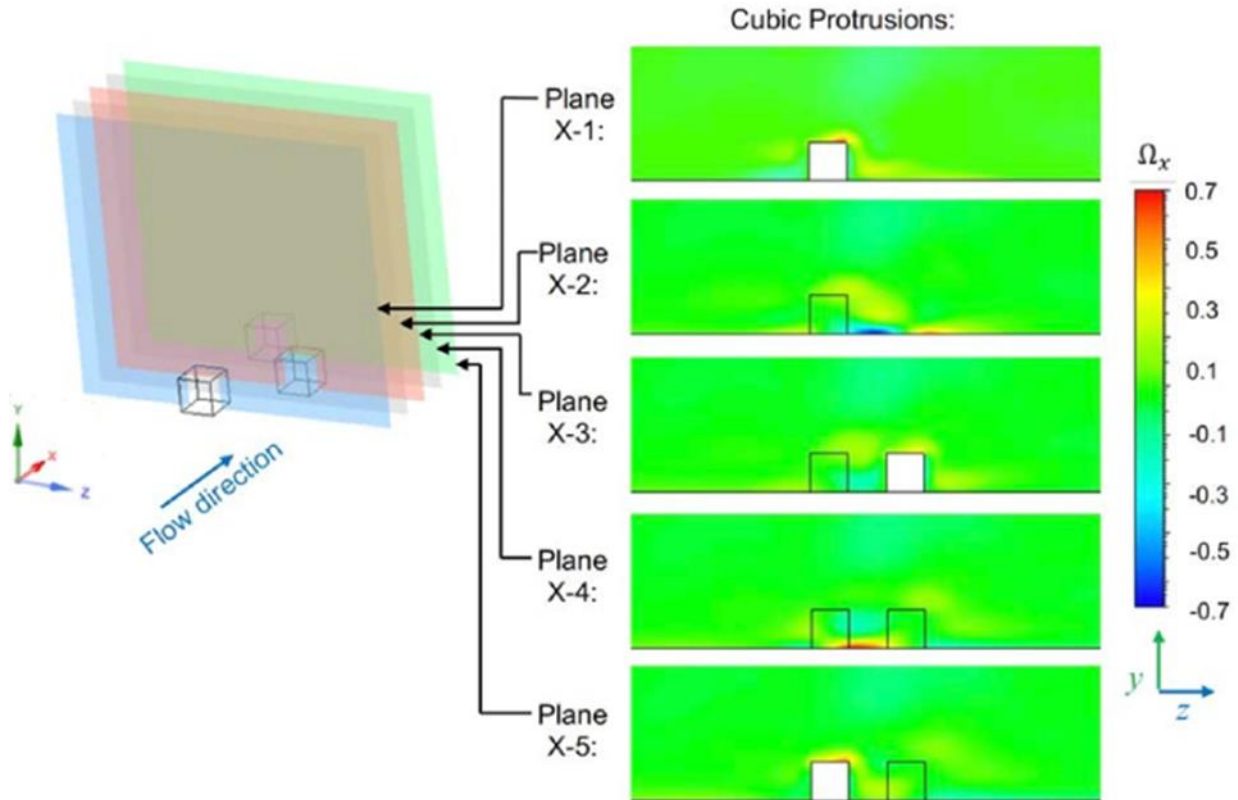


Figure 20 Distributions of time-averaged streamwise vorticity in three  $yz$  planes for cubic protrusions in the subcritical turbulent-boundary-layer over rough surfaces.

### 3.6 Investigations on rough surface baseline cases at supercritical conditions

#### 3.6.1 This section presents DNS simulations of simulated roughness on a heated surface cooled by a flow of water at the supercritical state. Test case

The computational domain for direct numerical simulation of heated channel flow of supercritical water with rough walls the same as that used in the smooth surface baseline cases and shown in Figure 8. The domain length of  $11.25\delta$  length is deemed sufficient for the present study since the focus is on the smaller-scale turbulence near the channel wall, which has been shown in several studies to dominate the local convection of heat from the wall into the working fluid (e.g. Bae et al., 2005; Li et al., 2008). The difference in the rough wall cases is that a slip boundary condition is prescribed to match the velocity and heat transfer profiles at the surface deduced from the patterned rough wall simulations. Inflow and outflow boundary conditions and the state of the working fluid are the same as that of the smooth wall case.

#### 3.6.2 Methodology

The present grid adheres closely to that of the smooth-surface simulation, with the exception of a segment of the computational domain along the lower wall of the channel. Shown in Figure 21, the spatial resolution is increased in the longitudinal ( $x$ ) and lateral ( $z$ ) directions in this segment of the domain. This region of highly refined grid extends to the fifth grid node from the wall and is

D3.1 Report summarizing the newly generated reference data for natural convection, forced and mixed convection and decay heat removal

spanwise centred in the computational domain covering 58.3% of the domain span along the lower wall. As visually indicated, the grid node spacings in the  $x$  and  $z$  directions are reduced by about an order of magnitude. In the wall-normal ( $y$ ) direction, the grid-node spacing is increased with distance from the wall at a rate that places 16 nodes below  $y^+ = 10$ . In the range of  $20 < y^+ < 150$ , the grid-node spacing follows  $\Delta y^+ = (0.41y^+)^{0.25}$ , which adheres to the Kolmogorov length scale distribution in the log-low region of wall-bounded turbulent flows. In the range  $\delta^+ > y^+ > 150$ , the node spacing is increased at a rate of 10%. This grid-node distribution in the  $x$ ,  $y$  and  $z$  directions results in grid cells that are orthogonal and have aspect ratios no larger than 25. The total grid-node count in the computational domain is 15.4 million, 9.1 million of which are located in the region of high grid refinement.

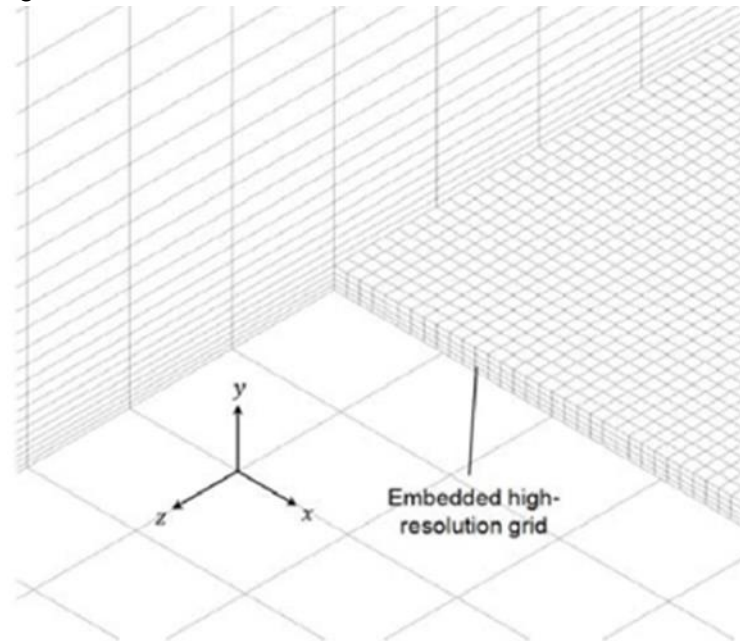


Figure 21 Partial view of grid in the computational domain and the highly refined region

The edge length of the simulated cavities is of  $d_r^+ = 5.0$  and  $10.0$  ( $d_r/\delta = 0.020$  and  $0.040$ ), with the cavities arranged in rows aligned with the streamwise direction. The centre-to-centre spacing between adjacent cavities in the streamwise rows and the spanwise spacing between adjacent rows is set equal to  $10.0$  wall units. Based on the results of the subcritical rough wall cases, the computational model does not include the fluid region within the cavities. Instead, the domain boundary is placed at  $y = 0$ , which corresponds to the wall-normal position of the openings of the cavities. The wall boundary conditions are applied in accordance to the observations in the subcritical rough wall cases, whereby along the opening of the cavity, the fluid is able to slip and is also able to move in and out of the cavity. The distribution of streamwise velocity at the edge of the cavity, imposed as the prescribed wall velocity in the simulation, is shown in Figure 22.

The wall velocity profile was specified as a uniform array of surface cavities, spaced such that they collectively occupy one quarter of the total surface area of the highly refined computational grid. The pattern of the array is shown in Figure 23. Additionally, a profile consisting of uniform patches of modelled surface cavities ( $d_r^+ = 10.0$ ), arranged in alternating fashion with smooth patches, was also simulated. This profile is shown in Figure 24.

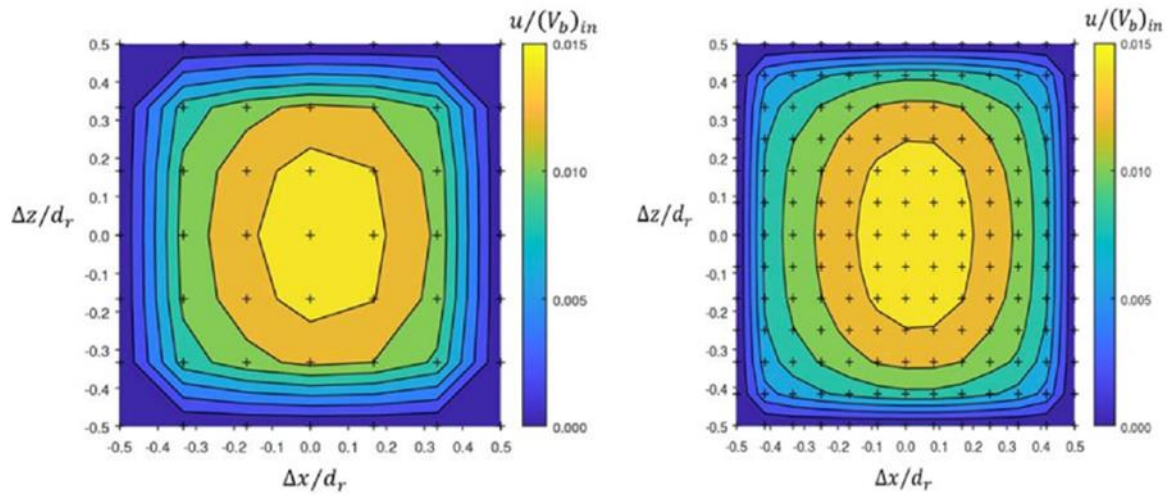


Figure 22 Distribution of streamwise (x) component of velocity at the wall with modelled cavity-type surface  $dr+ = 5.0$  (left);  $b) dr+ = 10.0$  (right).

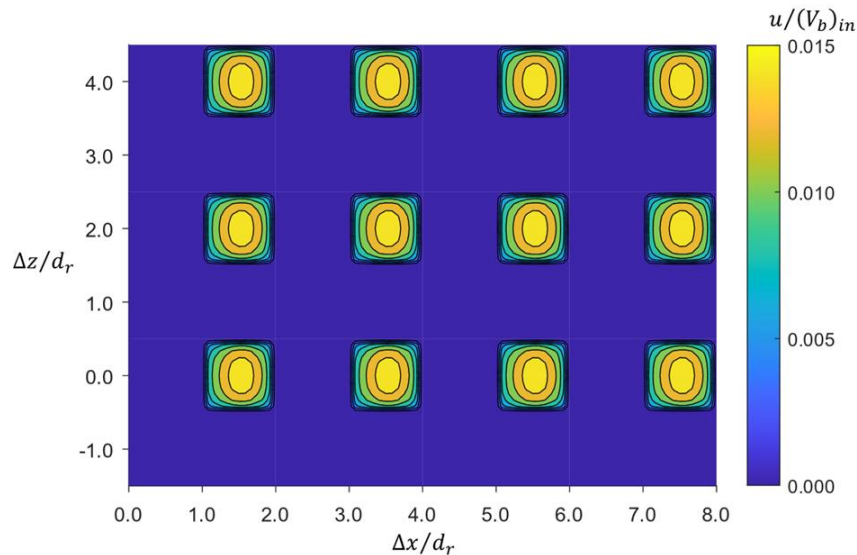


Figure 23 : Uniform array of modelled surface cavities, prescribed as a profile of the streamwise component of velocity, along the surface

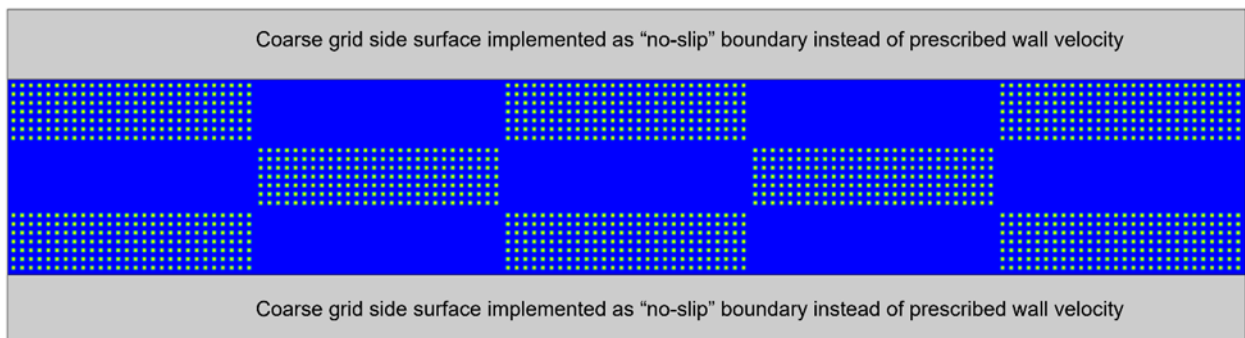


Figure 24 Wall velocity profile for alternating patches of surface cavities ( $dr+ = 10.0$ ) and smooth wall patches. The grey regions flanking the profile correspond to the parts of the surface outside of the highly-refined grid region. A no-slip boundary condition is imposed on these parts of the surface.

Consistent with the momentum boundary condition, the thermal boundary condition on the wall with surface roughness is imposed on the  $y = 0$  plane, excluding the fluid volume of the cavities. To establish a physical realistic Dirichlet boundary condition for heat flux at  $y = 0$ , a thermal-resistance-network analysis is performed. Relative to the material of the solid wall, which is set to be 316 stainless steel. The heat flux boundary conditions is shown in Figure 25.

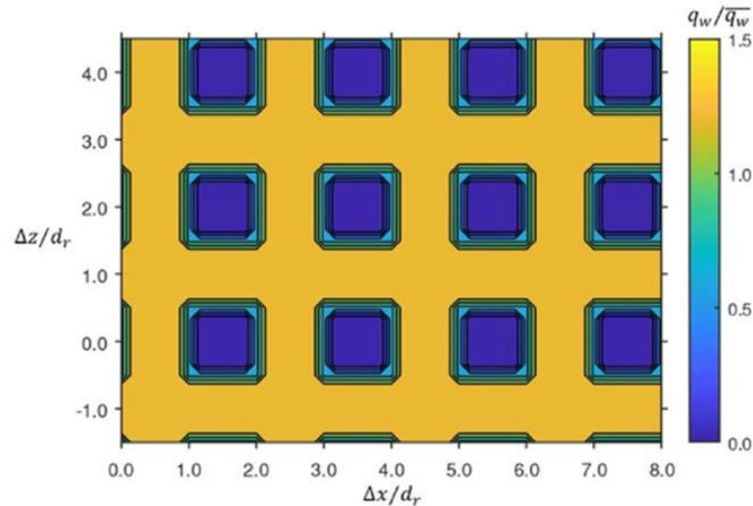


Figure 25 Heat flux boundary condition implemented on the channel wall at the  $y=0$  plane.

### 3.6.3 Results and discussion

The simulations in the presence of modelled surface cavities were primarily intended to serve as a scoping study to assess the sensitivity of forced convection heat transfer at supercritical states to small momentum and thermal perturbations at the liquid-solid interface. Accordingly, only a limited number of timesteps were computed for each case. The statistics presented henceforth, correspond to a sampling duration of 8,000 timesteps, with sampling at every 50 timesteps.

The streamwise distributions of the normalized wall temperature difference,

$$Nu^{(-1)}(x) \equiv (T_w(x) - T_i n) / \theta_q = (k_i n (T_w(x) - T_i n)) / ((q_w) \bar{\delta})$$

are plotted in Figure 26. This parameter represents a heat-flux-based characteristic temperature difference, and hence, may be interpreted as an inverse Nusselt number. The profiles plotted in Figure 26 correspond to time averages and spanwise averages of the wall temperature, and the wall shear stress, evaluated over the highly resolved portion of the surface. For the cases involving modelled surface cavities, the profiles have been smoothed over lengths equal to the streamwise periodicity of the cavities, to better identify the low-wavenumber perturbations which remain after averaging over the limited sampling duration. Evidence of the streamwise periodicity of the alternating rough patches can be detected in the profile of this case (Figure 26 (d)). Nonetheless, it is apparent that insufficient transient samples are available to compute meaningful statistics based on temporal/spanwise averaging alone. The dashed lines in each plot correspond to the streamwise average over the region, where represents the streamwise extent of the computational domain. Because the magnitudes of local deviations from this average, over the range of its evaluation, appear fairly uniform, it is judged reasonable to also adopt streamwise averaging to compute more robust turbulence statistics. The area within a plane used for spatial averaging is indicated Figure 25.

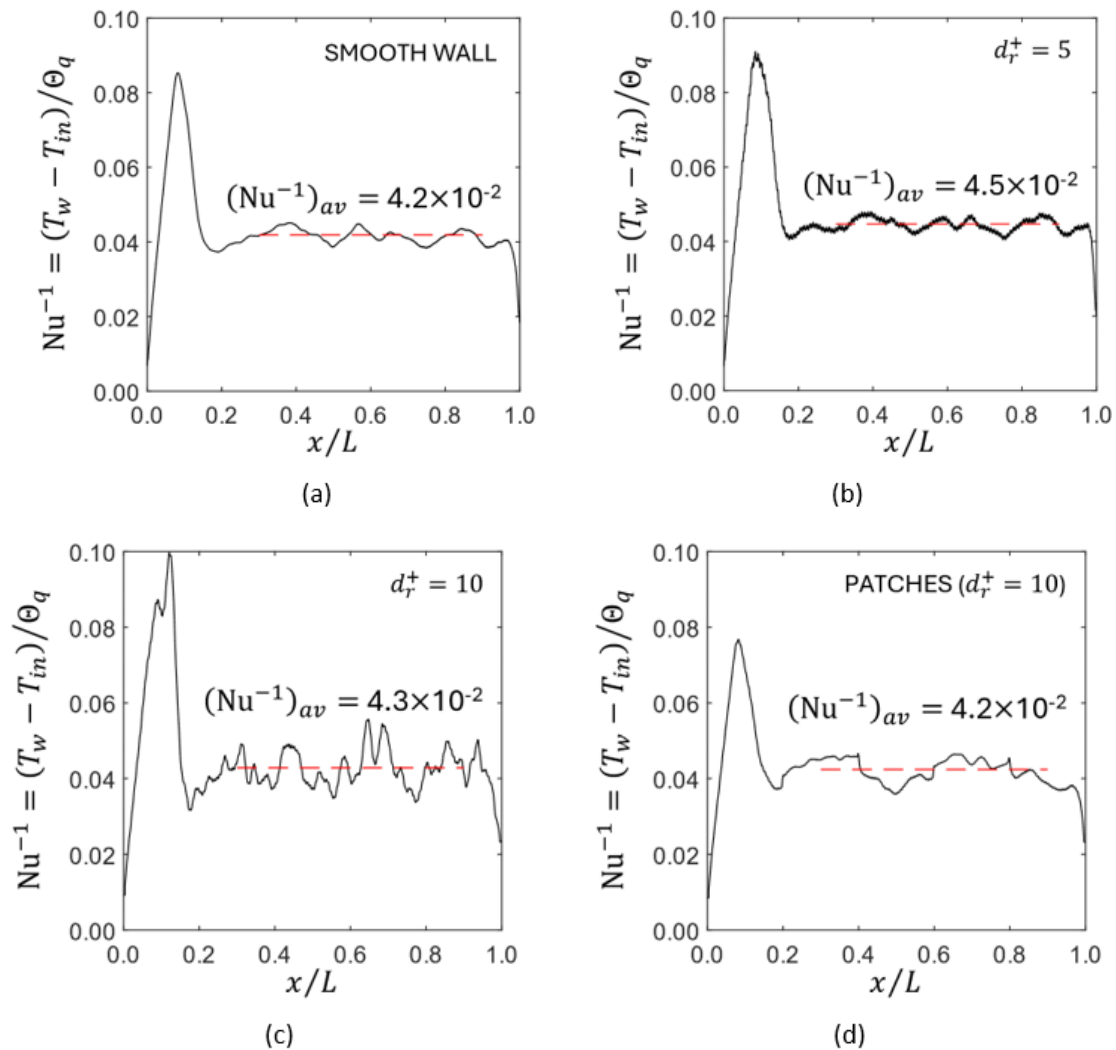


Figure 26 Streamwise variation of normalized wall temperature difference, for supercritical conditions; results correspond to a smooth wall (a), small wall cavities (b), large wall cavities (c), and alternating patches of large wall cavities (d).

The wall-normal profiles of the mean streamwise component of velocity, and the root-mean-square of each perturbation velocity component, as evaluated using conventional Reynolds time-averaging followed with streamwise/spanwise averaging, are plotted in Figure 26. Here the wall-normal coordinate is expressed in terms of viscous wall units, which are evaluated in terms of the streamwise/spanwise average viscous length scale computed for each case. Notable changes in the velocity and the velocity fluctuation profiles are only observed in the case where the simulated roughness elements correspond to  $d_r^+ = 10.0$ .

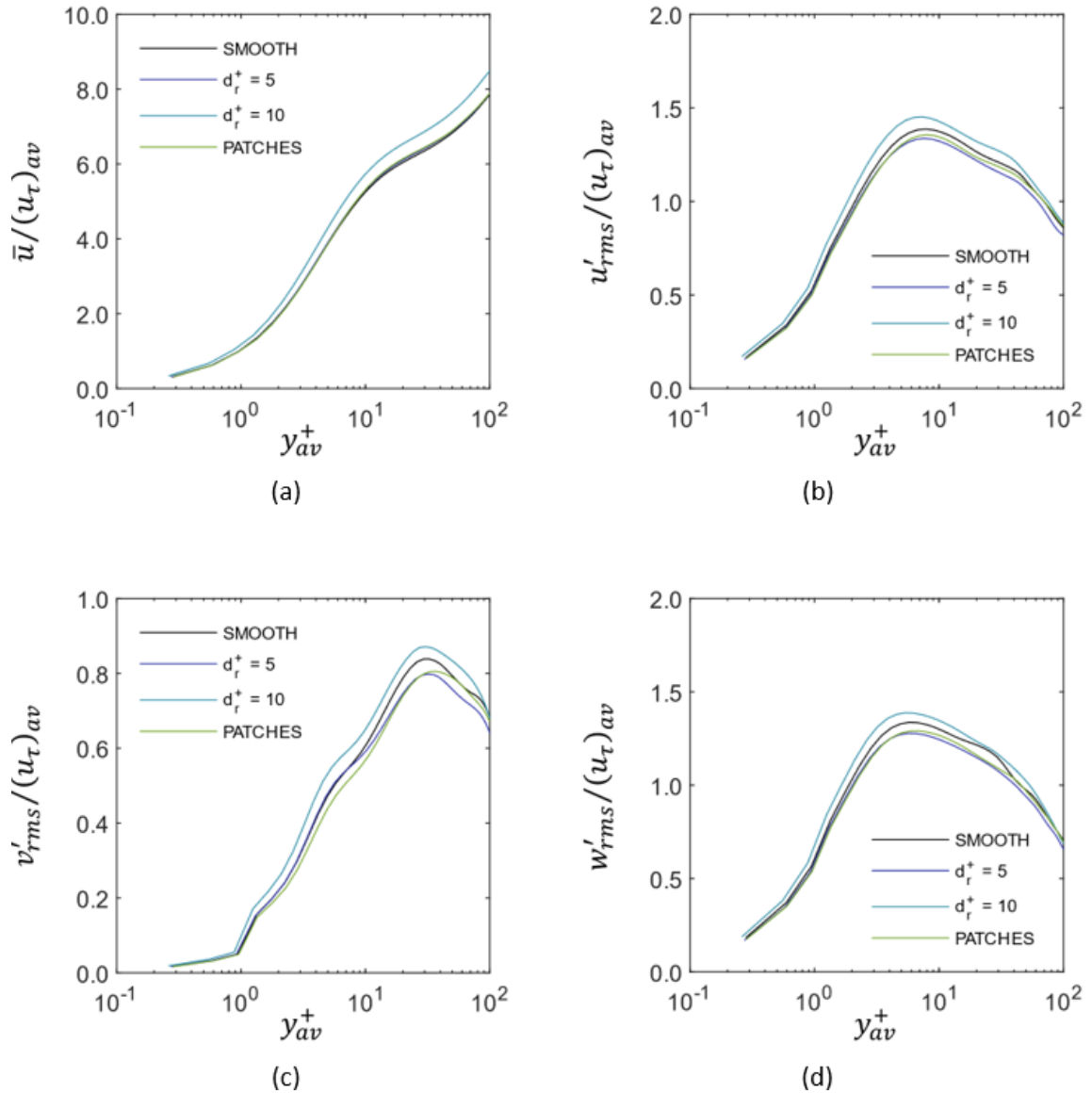


Figure 27: Normalized velocity profiles evaluated using conventional Reynolds time-averaging and spatial averaging over ; mean streamwise velocity component, (a), root-mean-square of perturbation velocity components (b), (c), and (d). The curves are plotted with respect to wall distance, normalized by the case-specific average viscous length scale.

## 4 Exposition of experimental specimens (CVR)

Material testing has been performed within WP2. The selected conditions were based on the available pre-conceptual design and experiences from the previous EU project (HPLWR, FQT), focusing on long-term corrosion resistance and fulfilling the knowledge gaps. One of the knowledge gaps is the development of the oxide layer within the long-term operation and its roughness. To complete this gap, the long-term exposure up to 10,000 h in SCW, at a temperature of 500 °C, pressure 25 MPa and 150 ppb oxygen, was proposed and performed within WP3.

For this purpose, candidate materials such as austenitic stainless steel 310S, and alloy 800H were chosen and accompanied by 316Ti possessing the same thermophysical properties as 310S. It must be mentioned, that at the beginning of the project, 310S was indicated as the key material based on available data concerning corrosion and mechanical properties at higher operation temperatures.

### 4.1 Experimental details

#### 4.1.1 Materials and specimens

Alloy 310 (UNS S31000) is an austenitic stainless steel developed for high-temperature corrosion-resistant applications. However, at a higher temperature (600-1000 °C [Amirkhiz B. S. et al, 2019]) the alloy is subjected to sigma phase precipitation, which deteriorates its properties. 310S (UNS S31008, DIN 1.4845) is the low-carbon version of the alloy. It is utilized for ease of fabrication. The composition is summarised in Table 4-1 and physical properties are in Table 4-2.

Iron-nickel-chromium alloy 800 is widely used for its strength at high temperatures and its ability to resist oxidation, carburisation, and other types of high-temperature corrosion. Titanium nitrides, titanium carbides, and chromium carbides normally appear in the alloy's microstructure. Consequently, alloys 800H and 800HT are similar to other austenitic alloys, in that they can be rendered susceptible to intergranular corrosion (sensitized) in certain aggressive environments by exposure to temperatures of 540-760 °C [Cao, Y. and Di, H., 2015]. The composition is summarized in Table 4-1 and the physical properties in Table 4-2.

Austenitic stainless steel 316Ti is a titanium-stabilized variation of alloy 316 that contains molybdenum to increase corrosion resistance, improve resistance to pitting chloride ion solutions, and increase strength at elevated temperatures. Due to its Titanium addition, 316Ti can be used at elevated sensitization temperatures. Corrosion resistance is improved, particularly against sulfuric, hydrochloric, acetic, formic and tartaric acids, acid sulphates and alkaline chlorides. The composition is summarized in Table 4-1 and physical properties are in Table 4-2.

Table 4-1: Chemical composition (in %wt.) of the selected materials.

	C	Si	Mn	P	S	Ni	Cr	Cu	Ti	Al	Mo	Co	Fe
<b>310S</b>	≤0.08	≤1.5	≤2	≤0.045	≤0.03	19-- 22	24-- 26	-	-	-	0.25	-	Bal.
<b>800H</b>	0.05-- 0.1	≤1	≤1.5	≤0.03	≤0.015	30-- 35	19-- 23	≤0.075	0.15- -0.6	0.15-- 0.6	0.18	0.11	Bal.
<b>316Ti</b>	≤0.08	≤1.0	≤2	≤0.04	≤0.03	10-- 14	16-- 18	≤0.075	5x (C+N) 0.07	-	2- -3	-	Bal.

Table 4-2: Selected physical properties (corresponding  $T$  at 20°C) of materials of interest.

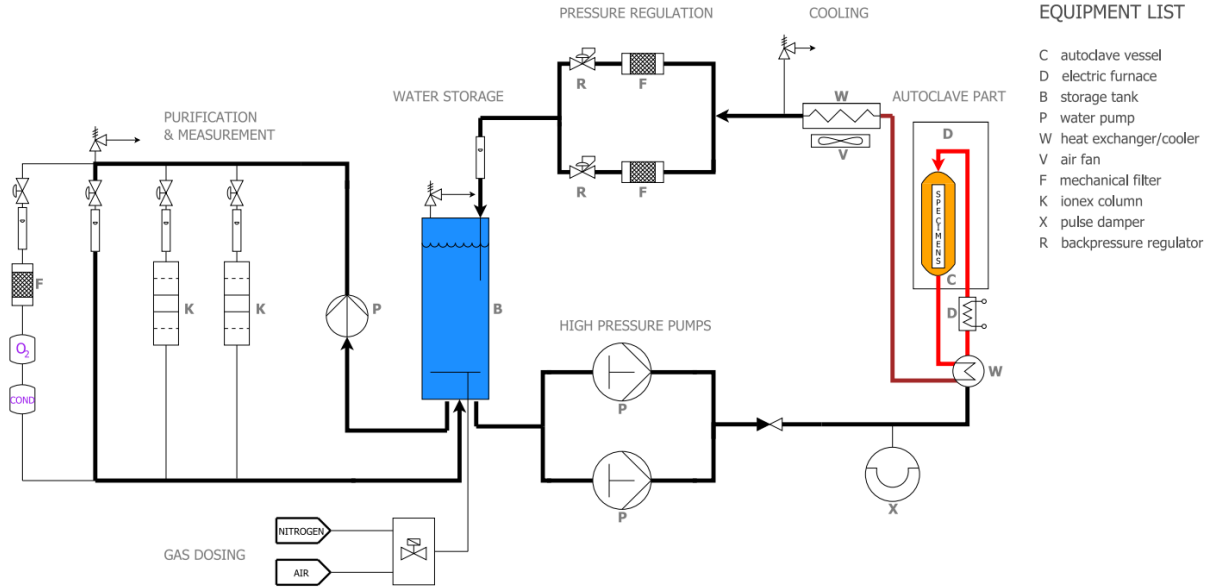
	Density [g.cm <sup>-3</sup> ]	Electrical Resistivity [Ω.mm <sup>2</sup> .m <sup>-1</sup> ]	Specific Thermal Capacity [J.kg <sup>-1</sup> .K <sup>-1</sup> ]	Thermal Conductivity [W.m <sup>-1</sup> .K <sup>-1</sup> ]
<b>310S</b>	7.8	0.72	500	14.2
<b>800H</b>	7.9	0.99	460	11.5
<b>316Ti</b>	8.0	0.75500	15.0	

The specimens were exposed in the shape of tubes in their as-received state. The two lengths of tubes were used due to the limited space in the autoclave vessel. The thickness of used tubes was varied as 1.0, 0.8, and 1.5 mm for 310S, 800H, and 316Ti, respectively. The diameter was 10 mm for 310S and 316Ti and 9.8 mm for 800H.

All specimens were ultrasonically cleaned with acetone and dried at the beginning of the exposure. During campaigns, the specimens were cleaned with ethanol. The specimens were weighed before and after each exposure with an accuracy of 0.00001 g.

#### 4.1.2 Autoclave

The specimens described in previous part 4.1.1 were exposed in SCW at 500 °C/25 MPa and 150 ppb DO. The temperature corresponds to the outlet temperature of the pre-conceptual design of EU SCW-SMR [Schulenberg, T., and Otic, I., 2022]. The exposure was performed in the high-temperature and high-pressure autoclave vessel. The autoclave vessel is a part of the system (Figure 27) consisting of a recirculating water loop and is designed for testing material corrosion under supercritical water conditions. The autoclave pressure vessel is made from Inconel 600, and it operates at a working pressure of 25 MPa and a maximum temperature up to 600 °C. The system is equipped with a low-pressure secondary recirculation loop that maintains water quality by using ion exchange columns and controls the level of dissolved oxygen.



- EQUIPMENT LIST**
- C autoclave vessel
  - D electric furnace
  - B storage tank
  - P water pump
  - W heat exchanger/cooler
  - V air fan
  - F mechanical filter
  - K ionex column
  - X pulse damper
  - R backpressure regulator

Figure 27: The sketch of the autoclave and accompanying equipment

### 4.1.3 Campaigns

The long-term exposure was divided into several campaigns to reveal how the oxide layer and the surface roughness are evaluated in time under SCW conditions. The overview of campaigns is shown in Figure 28. The specimens were evaluated between individual campaigns employing weight and surface roughness measurements. The surface was imaged by using SEM. The used techniques are described below in parts 4.1.4, and 4.1.5.

**ECC WP3 SCW experiment specimen distribution and matrix**

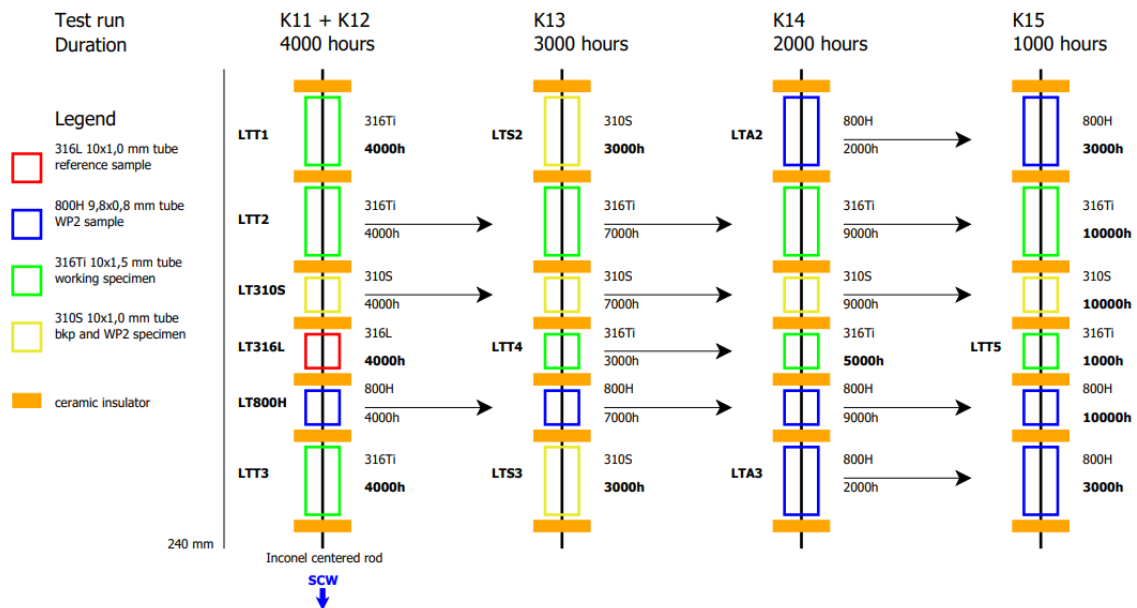


Figure 28: Scheme of the campaigns performed within WP3 based on cooperation with WP2

#### 4.1.4 Measurement of the surface roughness

##### *Contact profilometer*

Surface roughness profiles were measured with a stylus profilometer. This method is based on a contact of the stylus with specimens. The DektakXT stylus profilometer measures the electromechanical movement of the diamond tip over the specimen surface according to the scanning length, speed and force programmed by the user. The stylus is connected to an LVDT (Linear Variable Differential Transformer) transformer, which produces and processes electrical signals corresponding to the surface changes of the specimen. After conversion to digital format, surface changes are saved for display and analysis in Vision 64 software. Vision 64 displays and evaluates user-selected analytical functions for measuring surface finish and other parameters for characterizing profile data.

Roughness profiles were scanned by a stylus with a diamond tip with a radius of curvature of 2  $\mu\text{m}$  and a loading force of 7.5 mg. The standard scanning mode with a vertical scan resolution of 0.2  $\mu\text{m}$  in the range of about 4000  $\mu\text{m}$  was used. The cut-off  $\lambda_C = 0.8$  mm and short cut-off  $\lambda_S = 2.5$   $\mu\text{m}$  were used for the evaluation of the roughness according to ISO 4287 [ISO 4287:1997]. For  $R_a > 2$   $\mu\text{m}$  the scanning length was 1200  $\mu\text{m}$  and  $\lambda_C = 2.5$  mm and short cut-off  $\lambda_S = 2.5$   $\mu\text{m}$  [ISO 4287:1997]. Before the measurements, the specimens were cleaned with ethanol.

##### *Non-contact profilometer*

The Keyence VK-X100 optical profilometer was chosen for non-contact measurement. This device uses a red semiconductor laser with a wavelength of 658 nm to scan the surface. The surface topography was recorded with a 50x Nikon lens with a numerical aperture of 0.8 and a working distance of 0.54 mm. The Z-axis pitch in this configuration corresponds to 0.13  $\mu\text{m}$ . With this setup, measurements were carried out in three locations for each tested specimen in an area dimension of 4125x206  $\mu\text{m}$ . The data acquired was then used to map the topography of the surface and determine the roughness profile of each area.

#### 4.1.5 Evaluation of the oxide layer

A detailed evaluation of the oxide layer was done using the scanning electron microscope (SEM) TESCAN Lyra3 GMU equipped with a field emission gun. The acceleration voltage ranged from 0.05 up to 30 kV. The microscope is equipped with several detectors, from which SE (Secondary Electrons), and BSE (Backscatter Electron) were used for imaging.

#### 4.2 Results of the long-term exposure

The long-term exposure was performed in the frame of WP3 and in cooperation with WP2. The selected specimens with geometry corresponding to requirements on fuel cladding were exposed in SCW at 500 °C/25 MPa for up to 10,000 hours. The interest was given to evaluation of the surface roughness in time under simulated conditions of SCW-SMR. The achieved results are summarized in the plot shown in Figure 29.

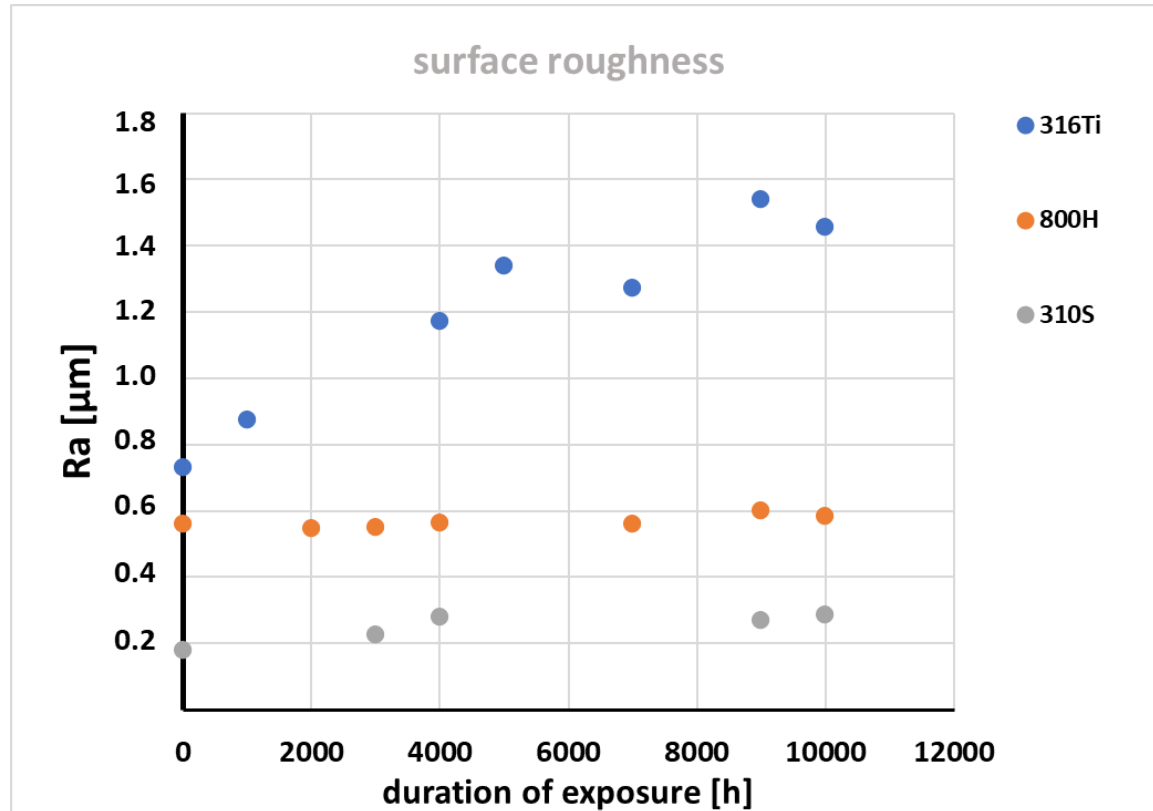


Figure 29: The evaluation of the surface roughness during exposure in SCW at 500 °C/25 MPa up to 10,000 hours

It can be seen in Figure 29 that the surface roughness represented by parameter  $R_a$  (see in Chapter 2.5) is almost without changes for stainless steel 310S and slightly increased for 800H. In the case of stainless steel 316Ti possessing lower corrosion resistance (in comparison with the other used material), the  $R_a$  is increased with time of exposure. Nevertheless, such values of  $R_a$  are still quite low even for 316Ti from the thermal-hydraulic point of view.

In Figure 29 the as-received surface of 316Ti with  $R_a \sim 0.7 \mu\text{m}$  can be seen in contrast with the cross-section of the oxide layer grown on the specimen during 10,000 h exposure. Based on the top view (Figure 30 (a, b)) images, it can be concluded that the topography of the oxides follows the as-received surface. As the oxide layer is not compact, the exfoliation of this layer could be expected with further increased exposure time and thus some changes in the surface roughness could occur. However, such changes are almost impossible to predict.

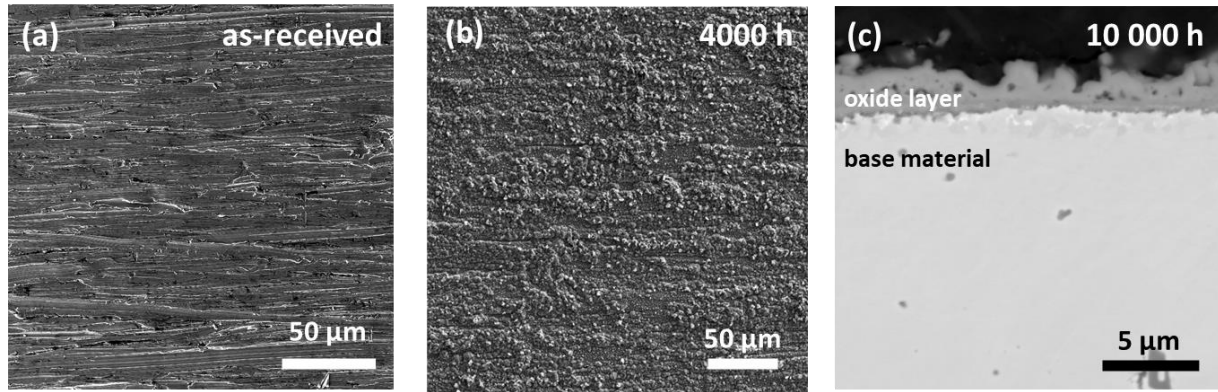


Figure 30: The SEM images of the surface of stainless steel 316Ti at the as - received state(a), after 4,000h in SCW 500 °C/25MPa (b), and after 10,000 h in SCW 500 °C/25MPa in the cross-section (c).

Figure 31 shows the 3D model of the surface of 316Ti and its changes after 4,000 and 10,000 hours.

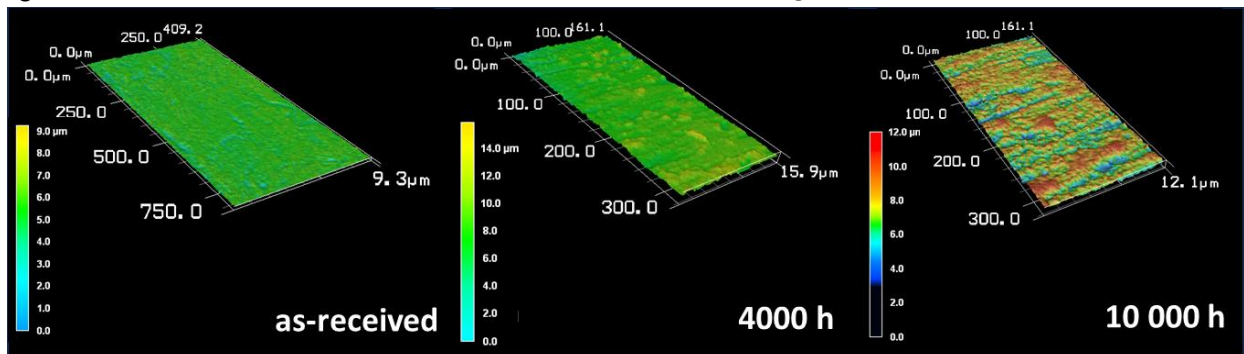


Figure 31: The 3D model of the surface of the stainless steel 316Ti before the exposure (as-received state), after 4,000 h in SCW 500 °C/25 MPa, and after 10,000 h in SCW 500 °C/25 MPa.

The changes in the surface of 310S are summarized in Figure 32 and Figure 34. It can be seen that the oxide layer is compact and thin ( $\leq 3 \mu\text{m}$ ), in Figure 32 (d).

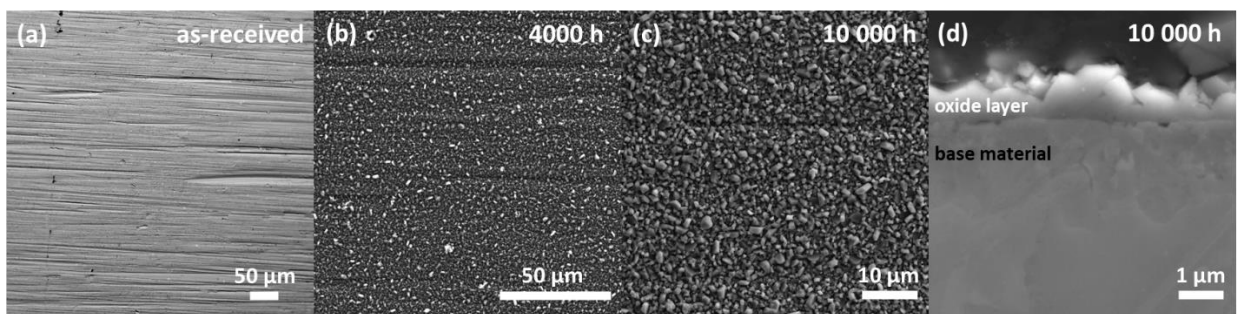


Figure 32: The SEM images of the surface of stainless steel 310S at as-received state (a), after 4,000 h in SCW 500 °C/25 MPa (b), and after 10,000 h in SCW 500 °C/25 MPa (c) also in the cross-section (d).

The 3D images of the surface of 310S after 4,000 and 10,000 hours in SCW show how the oxides follow/reflect the topography of the as-received surface more obviously in contrast with 316Ti (Figure 33).

D3.1 Report summarizing the newly generated reference data for natural convection, forced and mixed convection and decay heat removal

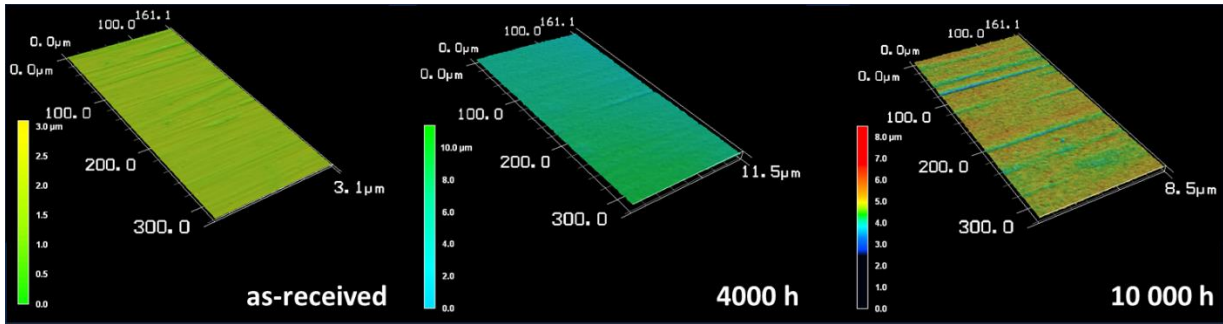


Figure 33: The 3D model of the surface of the stainless steel 310S before the exposure (as-received state), after 4,000 h in SCW 500 °C/25 MPa, and after 10,000 h in SCW 500 °C/25 MPa

In the case of 800H, the results (Figure 34) are comparable with austenitic stainless steel 310S, namely the compactness and thickness of the oxide layer.

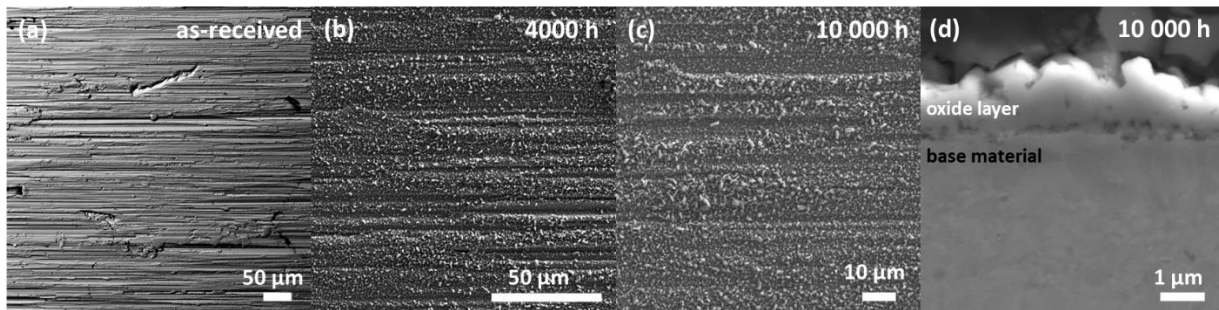


Figure 34: The SEM images of the surface of alloy 800H at as-received state (a), after 4,000 h in SCW 500 °C/25 MPa (b), and after 10,000 h in SCW 500 °C/25 MPa (c) also in the cross-section (d).

FFigure 35 does not reveal any interesting changes between the surface after 4,000 hours and 10,000 hours of exposure in SCW.

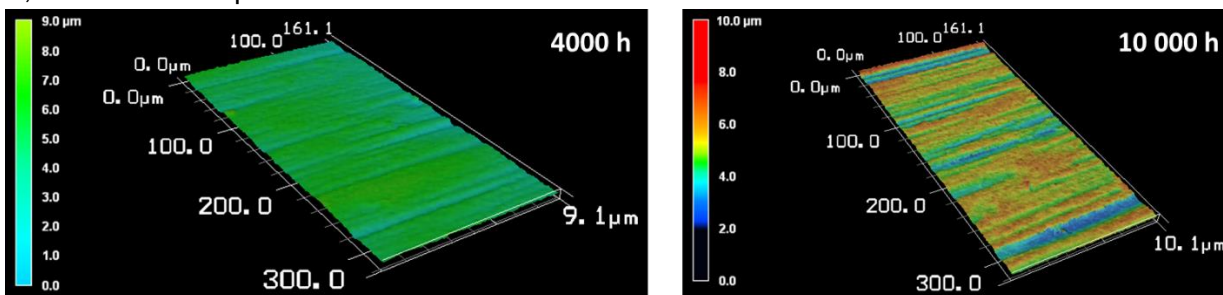


Figure 35: The 3D model of the surface of the alloy 800H after 4,000 h, and after 10,000 h in SCW 500 °C/25 MPa.

It should be noted that data on long-term exposure of candidate structural materials in SCW are rare. Usually, the surface roughness is not measured or considered when describing the corrosion behaviour. It is important to highlight that a successful change was implemented in ECC-SMART due to the close cooperation between WP2 (material testing) and WP3 (thermo-hydraulic and safety). This collaboration provided new insights into material testing and beneficial for WP3 as well. As the commercially available tubes were used, a unique set of data was produced. Unfortunately, it was also proven that candidate materials possess high corrosion resistance despite the harsh environment of SCW. As a result, the oxide layer remains thin, and compact and follows the initial texture/topography of the surface with almost negligible change of the surface roughness represented by parameter  $R_a$ .

## 5 Direct numerical simulations of flow over rough surfaces (USFD)

### 5.1 Introduction

Subtask 3.2.4 aims to produce reference data using DNS on the effect surface roughness has on supercritical turbulent flow and heat transfer. Barring, the work by Mann et al., 2023, where they investigated supercritical turbulent heat transfer for cavity- and protrusion-type roughness elements, there is a clear lack of DNS data on the effect of roughness in supercritical fluids. Surface roughness enhances turbulent heat transfer and shifts heat transfer deterioration to higher bulk enthalpies as discussed in Section 2 (sub-task 3.2.1) by KIT in the introduction of their experimental work. The outcome of sub-task 3.2.1 is an experimental reference database. Our work (sub-task 3.2.4) aims to complement the experimental campaign by providing a numerical database capturing the local effects that experiments cannot.

The subtask makes use of the in-house DNS solver CHAPSim2. To account for the wall roughness, we use an immersed boundary approach. Our work was split into three primary goals, which are:

- Develop and implement an Immersed Boundary Method with heat transfer for rough surfaces in CHAPSim2.
- Perform investigations for smooth surfaces
- Perform investigations for rough surfaces

An immersed boundary method with heat transfer considerations has been developed. This version of the DNS solver is open source and will be publicly available to use by 01/2025 (url is <https://github.com/weiwangstfc/CHAPSim2.git>). The investigations performed have considered both vertical and horizontal buoyancy influenced flows. Horizontal flows were a necessary addition to the work as the ECC-SMART concept has horizontal fuel assemblies (Schulenberg and Otic, 2022). The  $y^+$  of the roughness elements considered (at isothermal conditions) is 9.7, which is roughly in line with the studies by Mann et al., 2023 and some of the experimental cases in sub-task 3.2.1.

### 5.2 Methodology

The cases contained in the reference database are computed using the DNS solver CHAPSim 2.0. In this sub-section, the base DNS solver is described. Sub-section 5.3 and 5.4, then discuss the immersed boundary method implemented in the base solver to account for surface roughness.

The solver was initially developed at Sheffield as CHAPSim 1.0 but was further developed (into CHAPSim 2.0) by the UK CCP-NTH (Collaborative Computational Project Nuclear Thermal Hydraulics). The solver is fully staggered and uses high-order compact schemes (up to 6th order) for spatial discretisation (Lele, 1992). To advance in time, the solver uses the low-storage third-order explicit Runge-Kutta method, combined with the fractional step method by Kim and Moin, 1985 to enforce the continuity equation. The Poisson equation is solved fully in spectral space using 3D fast Fourier transforms. The 2D decomposition library (2DECOMP&FFT) is used to parallelise the code.

The dimensionless low-Mach number form of the Navier-Stokes equations is solved for supercritical fluids. In the low-Mach number limit, pressure is decomposed into thermodynamic and hydrodynamic components. The former is considered constant, while for the latter, the hydrodynamic pressure fluctuations are neglected. Thermophysical properties are thus

D3.1 Report summarizing the newly generated reference data for natural convection, forced and mixed convection and decay heat removal

considered at a constant thermodynamic pressure and vary as a function of enthalpy. Studies by Bae et al., 2005, Peeters et al., 2017, Nemati et al., 2016 and He et al., 2021 have similarly used this approach. In the present cases, the thermophysical properties are obtained from the NIST database (Lemmon et al., 2010). Equations 1 - 3 show the non-dimensional governing equations for mass, continuity, and energy solved in CHAPSim 2.0.

$$\frac{\partial(\rho)}{\partial t} + \frac{\partial(\rho u_i)}{\partial x_i} = 0 \quad (5.1)$$

$$\frac{\partial(\rho u_i)}{\partial t} + \frac{\partial(\rho u_i u_j)}{\partial x_j} = \frac{\partial p}{\partial x_i} + \frac{1}{Re} \frac{\partial \tau_{ij}}{\partial x_j} \pm \frac{\rho}{Fr^2} \delta_{1i} + \mathbf{F} \quad (5.2)$$

$$\frac{\partial(\rho h)}{\partial t} + \frac{\partial(\rho h u_j)}{\partial x_j} = \frac{1}{Re \cdot Pr} \frac{\partial}{\partial x_j} \left( \lambda \frac{\partial T}{\partial x_j} \right) \quad (5.3)$$

Where  $i, j = 1, 2, 3$ , and represents, the streamwise, wall-normal and spanwise directions, respectively.  $\rho$  is the density,  $p$  is the pressure,  $u$  is the velocity,  $t$  is the time,  $h$  is the enthalpy,  $\lambda$  is the thermal conductivity, and finally  $T$  is the temperature.  $\mathbf{F}$  is a body force only applied to the solid body using a direct forcing method. The non-dimensional variables are thus defined as  $t = \frac{t^*}{\delta^*/u_0^*}$ ,  $x_i = \frac{x_i^*}{\delta^*}$ ,  $u_i = \frac{u_i^*}{u_0^*}$ ,  $p = \frac{p^*}{\rho_0^* u_0^* u_0^*}$ ,  $h = \frac{h^* - h_{ref}^*}{c p_0^* T_0^*}$ , and  $T = \frac{T^*}{T_0^*}$ . The thermophysical properties are scaled by their respective values at the inlet temperature. Please note that to make enthalpy non-dimensional we use  $h_{ref}^*$ , which is the enthalpy at a reference temperature (where  $T_{ref}^* = T_0^* + \Delta K$ ). This reference temperature (which is 900 K for supercritical water) is chosen to shift the non-dimensional enthalpy such that the profiles for  $\rho h$  and  $h$  are smooth and monotonic. This shift is useful in increasing the numerical stability of the simulation. Reynolds, Prandtl and Froude numbers are thus defined as  $Re = \frac{\rho^* u_0^* \delta^*}{\mu_0^*}$ ,  $Fr = \sqrt{\frac{u_0^{*2}}{g^* \delta^*}}$  and  $Pr = \frac{\mu_0^* c p_0^*}{\lambda_0^*}$ . In the preceding definitions, \* is the dimensional quantity.

### 5.3 Immersed Boundary Method (IBM)

In equation 5.2, the term  $\mathbf{F}$  is introduced and is the IBM forcing term. The immersed boundary approach is a way of mimicking the effect of a complex body whilst using a structured grid. Figure 36 shows a couple of sketches illustrating the concept. The benefits of adopting an immersed boundary approach are an easier mesh generation approach for complex bodies (i.e. we avoid the use of unstructured grids), which ultimately leads low memory requirements, efficient solvers and usually better convergence characteristics.

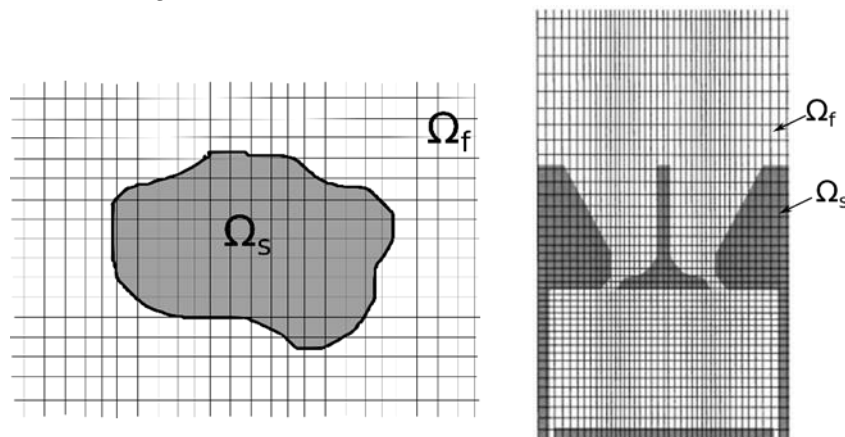


Figure 36: Illustrations of complex bodies imposed on a 2D cartesian grid. Right hand side figure from Fadlun et. al, 2000

D3.1 Report summarizing the newly generated reference data for natural convection, forced and mixed convection and decay heat removal

The force ( $F$ ) is computed using the direct forcing method by Fadlun et al., 2016 and is defined as  $F^{n+\theta} = (u^{n+1} - u^n)/\Delta t - RHS^{n+\theta}$ . Where, RHS is the right-hand side terms of the discretised momentum equation and  $u^{n+1}$  is the target velocity (usually zero for fixed solid body). This force is applied everywhere inside the solid region and ensures that the desired target velocity is attained.

There are three crucial steps required to compute  $F$ . These are (i) geometry description, (ii) identification of node type, and (iii) applying the IBM force. Steps (i) and (ii) are only done at the start of computation, while step (iii) is done at every time step. Figure 37 illustrates the steps, and for the sake of brevity we will not further elaborate on these.

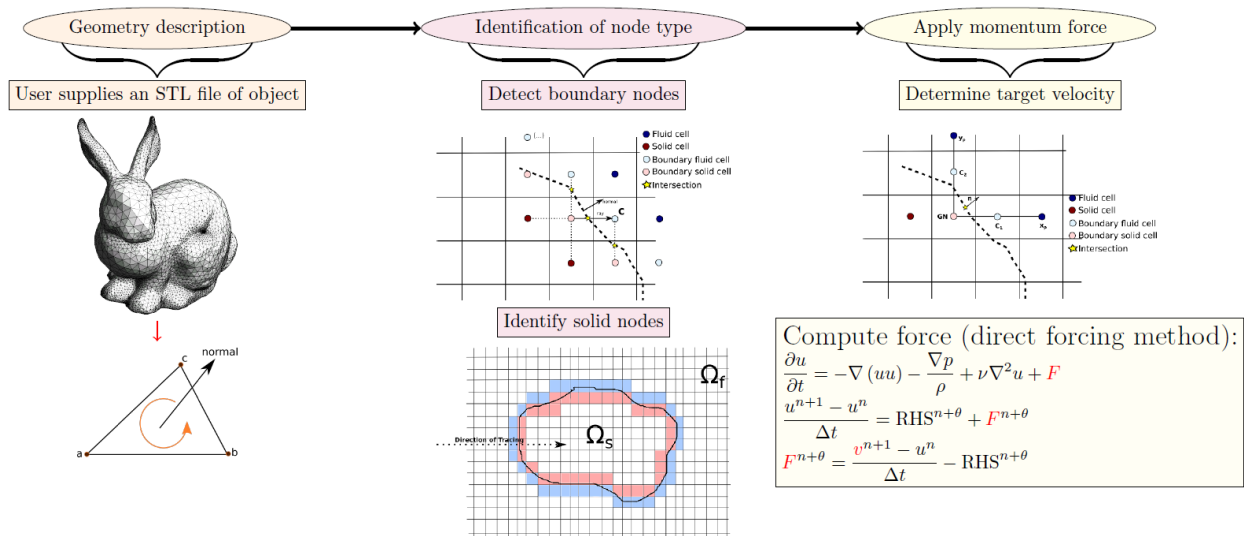


Figure 37: Illustration of the steps required to model an immersed body or rough surface in CHAPSim2. The steps for geometry description and Identification of node type are only performed once at the beginning of the computation.

## 5.4 Thermal boundary conditions for a rough surface using the Immersed Boundary Method

The immersed boundary method has been described above for momentum. In this section, we extend this approach so that thermal boundary conditions can be applied to the rough surface. The method developed to attain this capability is briefly described in this sub-section.

The fluid energy equation is presented in equation (5.3), and below in equation (5.4) the solid body energy equation is given:

$$\frac{\partial(\rho_s h_s)}{\partial t} = \frac{1}{Re \cdot Pr} \frac{\partial}{\partial x_j} \left( \lambda_s \frac{\partial T_s}{\partial x_j} \right) + S_\phi \quad (5.4)$$

Where, the subscript  $s$  represents the solid and  $S_\phi$  is a volumetric source term that is only applied to the solid body. As can be seen, within the solid body we neglect the convection term. This approach is adopted as it tends to enhance the stability of the simulation.  $Re$  and  $Pr$  are the same as those for the fluid region. The solid properties  $T_s$ ,  $\rho_s$ ,  $h_s$  and  $\lambda_s$  are the non-dimensional solid properties, which have been normalised using the reference fluid properties.

Three boundary conditions, which are (i) Constant Wall Temperature (CWT), (ii) Constant Wall Flux (CWF), and (iii) Conjugate Heat Transfer (CHT) can be applied. At a base level, these methods rely on imposing Dirichlet boundary conditions at the boundary face between a solid and fluid node. Furthermore, the CWT and CWF methods are simplifications of the CHT method.

D3.1 Report summarizing the newly generated reference data for natural convection, forced and mixed convection and decay heat removal

Thus, we will primarily describe the implementation of the CHT method. Figure 38 illustrates the approach.

To begin, the intersection/interface temperature ( $T_{int}$ ) must be computed by enforcing:

- the continuity of temperature  $T_s|_{int} = T_f|_{int}$
- heat flux  $\kappa \frac{\partial T_s}{\partial x}|_{int} = \kappa \frac{\partial T_f}{\partial x}|_{int}$ .

Here, the intersection temperature is that at the point where the path between two adjacent nodes, bisects the immersed/solid surface (see Figure 38). Taking these two equations, the intersection temperature is defined as:

$$T_{int} = \frac{\kappa_f(4T_{1f} - T_{2f}) + \kappa_s(4T_{1s} - T_{2s})}{3(\kappa_f + \kappa_s)} \quad (5.5)$$

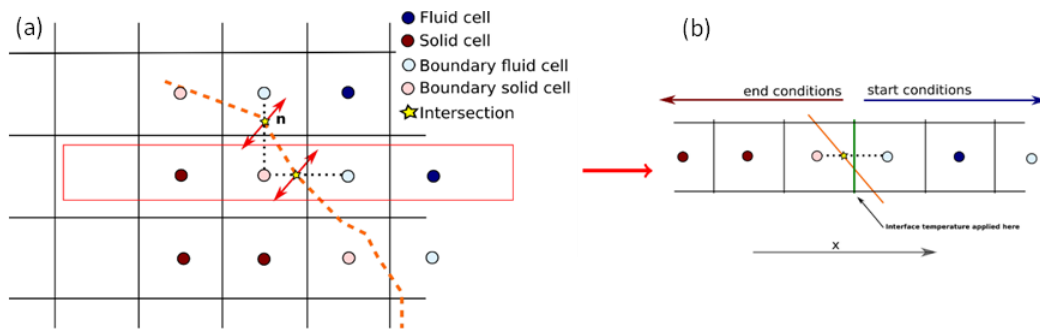


Figure 38: Schematic of the conjugate heat transfer implementation

The temperatures  $T_{1f}$ ,  $T_{1s}$ , etc are those interpolated to imaginary points. These points (imaginary) are probes normal to the immersed surface at the intersection. The above equation requires four imaginary points, and at each imaginary point, we compute its value via either tri-linear or bi-linear interpolation. If there are not enough nodes present for at least bi-linear interpolation, or the imaginary point does not reside in the desired region, the intersection temperature is then computed as:

$$T_{int} = \frac{\kappa_f T_{1f} + \kappa_s T_{1s}}{\kappa_f + \kappa_s} \quad (5.6)$$

It should be noted that the intersection point does not exist in the numerical grid, and thus the Dirichlet boundary condition must be indirectly imposed. As shown in Figure 38(b), the boundary condition must be applied on the face in-between the solid and fluid boundary nodes. There are two key steps to attain this:

- first, the intersection temperature must be interpolated to the artificial boundary face.
- Secondly, the resulting flux must be computed via the use of one-sided functions.

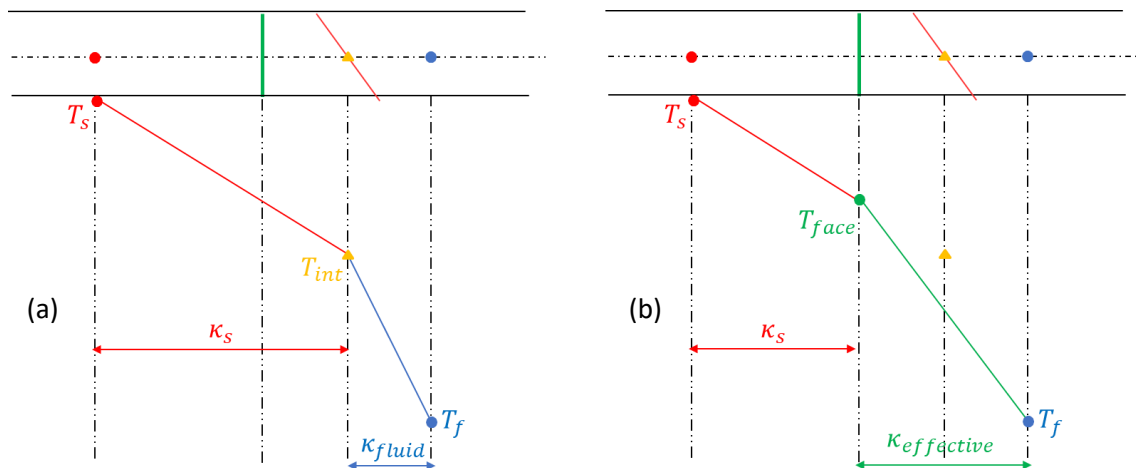


Figure 39: Sketch showing the computation of the artificial boundary face temperature. In Figure (a), the physical temperature variation is shown. Figure (b) shows the numerical temperature variation is shown.

The artificial boundary face temperature is linearly interpolated, and the approach is shown in Figure 39.

From the figure, note that the effective conductivity must be computed for the partially solid and fluid cells. To compute, the effective conductivity, three fluxes at the solid node, interface, and fluid node are equated (this derivation is not shown here). Once the temperature at the artificial boundary and effective conductivity are known, one-sided functions shown in equation (5.7) can be used to approximate the derivative as follows:

$$f'_{ib} = \frac{af_{ic} + bf_{ic+1}}{2\Delta x} \tag{5.7}$$

### 5.5 Validation and Verification

The Immersed Boundary Method and heat transfer aspects of the implementation have been validated and verified by comparing against data from literature. Table 5-1 provides a list of the tests carried out.

Table 5-1: Table of verification and validation tests carried out for the immersed boundary method

Test id	Code verification or validation test	Immersed surface thermal boundary conditions	Flow condition
1	Turbulent channel flow in a pyramid roughened channel	n/a	Turbulent
2a	Laminar unconfined flow over a heated cylinder	Constant Wall Temperature	Laminar
2b		Constant Wall Flux	Laminar
3	Pure conduction of an immersed sphere in an asymmetrically heated channel	Conjugate Heat Transfer	Conduction only

The first validation compares against the data by Seddighi et al., 2015. In their work, Seddighi et al., 2015 model an isothermal channel with a smooth top surface and roughened bottom surface. The roughened bottom surface comprises of closely packed pyramids. In our, validation simulation the modelled channel is made up of closely packed pyramids on both the top and bottom surface (i.e. both surfaces are roughened). Figure 40 shows the normal stress comparisons. As can be seen the comparisons are quite good with marginal differences appearing away from the wall. These differences are potentially tied to the consideration of roughness on both surfaces in our simulation.

The validation exercises are further extended to non-isothermal flow conditions by considering a cylinder in an unconfined flow (test 2). Two thermal boundary conditions, which are constant wall temperature (test 2a), and constant wall flux (test 2b) are considered in this study.

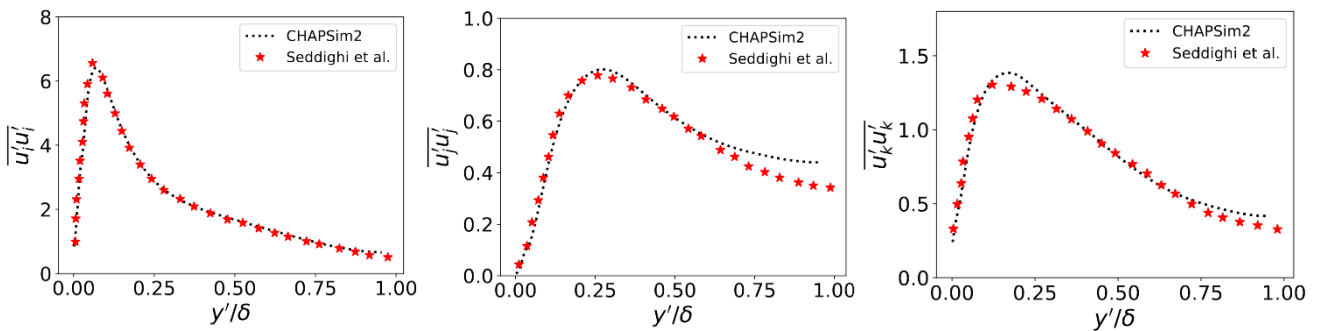


Figure 40: Comparison of the normal stresses against the data from Seddighi et al., 2015. Note that the reference data has only the bottom wall rough, while the present simulation has both surfaces roughened.

Figure 41 shows the constant wall temperature case. For this case, we can also compare the local pressure coefficient and local friction factor on the surface of the cylinder. The comparison is made against the datasets from Das et al, 2018, and Tseng and Ferzinger, 2003. As can be observed the comparisons are quite good. However, for the local friction factor it must be noted that the results for CHAPSim2 show a marginally increased peak. The next verification case (test 2b) is shown in Figure 42. For this case only the Nusselt number is compared.

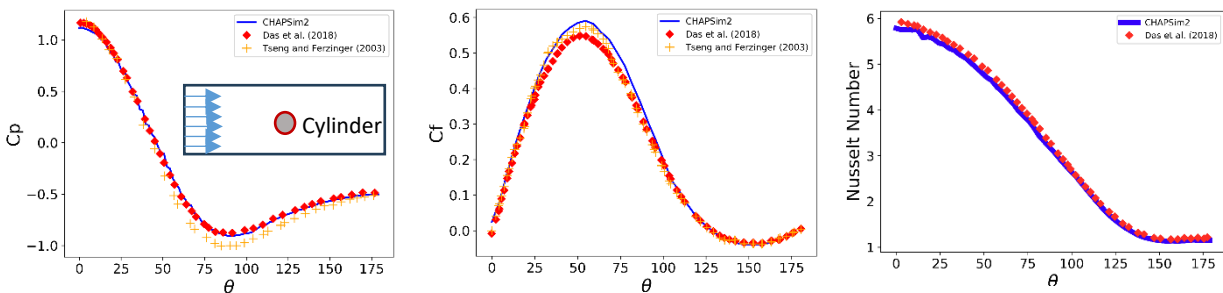


Figure 41: Test 2a – Nusselt number,  $C_p$  and  $C_f$  comparisons for an unconfined cylinder with a constant wall temperature boundary condition. Comparisons are made against the data from Das et al., 2018 and Tseng and Ferzinger, 2003.

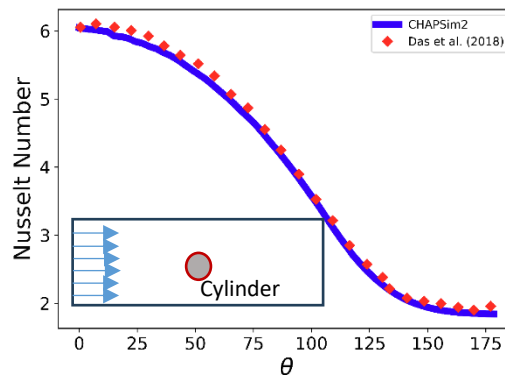


Figure 42: Test 2b – Nusselt number comparison for an unconfined cylinder with constant heat flux verification test case. Comparison is against data from Das et. al., 2018

The last verification case (test 3) essentially considers an immersed sphere in a stagnant fluid. The top and bottom surfaces of the modelled domain are asymmetrically heated with constant wall temperature boundary conditions being applied. A sketch of the geometry is shown in Figure 43. The submerged cylinder is then coupled to the outer fluid via a conjugate heat transfer approach. This system is allowed to thermally develop. Once fully developed the integral flux should be zero, and in our tests, with differing thermal conductivities the integral flux reaches  $\approx 10^{-6}$ .

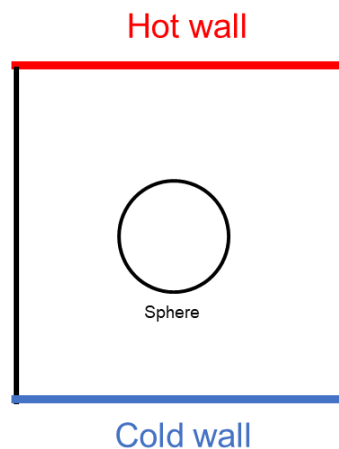


Figure 43: Test 3 – Sketch of the modelled domain for pure conduction for an immersed sphere in a heated channel.

## 5.6 Description of cases in the reference database

Four cases will be contained in the reference database. These cases are for fully developed asymmetrically heated channel flow with either smooth or pyramid-roughened surfaces. The fluid considered is supercritical water at 23.5 MPa. One wall is maintained at 640.15 K and the other at 655.5 K. The pseudocritical temperature for supercritical water at this pressure is 652.5 K. Table 5-2 provides a description of these cases.

Table 5-2: Cases presently contained in the reference database

Gravity vector	Case	Surface condition	$Re_b \approx$	$Re_\tau \approx$	$T_{cold}(K)$	$T_{hot}(K)$
Streamwise direction	SB2800-V	Smooth	2800	180	640.15	655.5
	PB2800-V	Rough		210		
Wall normal direction	SB2800-H	Smooth		180		
	PB2800-H	Rough		210		

Figure 44 shows the modelled domain for the vertical case. In the horizontal case, the gravity vector is flipped as shown in the figure.

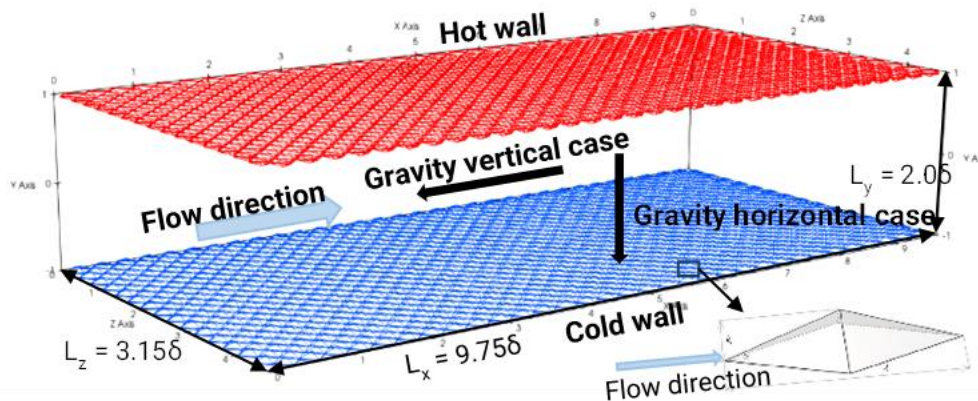


Figure 44: Modelled domain for rough wall simulations. Insert is a close-up of the roughness topography. The gravity vector is oriented in the streamwise direction for the vertical cases, and in the wall normal direction for horizontal case

Periodic boundary conditions are imposed in the streamwise (x), and spanwise directions (z). While in the wall-normal direction, Dirichlet boundary conditions are imposed for velocity and temperature. This setup means the cases are for a fully developed vertical or horizontal channel flow. In these cases, there is no heat advection nor streamwise thermal development. Instead, once the flow fully develops, heat is balanced by transfer from the hot to the cold wall via a combination of molecular, turbulent conduction, and turbulent heat flux.

In the rough wall simulation, the hot and cold surfaces are tiled with closely packed pyramids. The edge/slope angle of the pyramid is  $\alpha = 18.4^\circ$  with a wavelength of  $0.3 \delta$  and a peak height of  $k_t = 0.05\delta$ . A similar pyramid geometric configuration was used by Seddghi et al., 2015 The computational domain is  $9.75 \delta$ ,  $2.0 \delta$  and  $3.15 \delta$  in the streamwise (x), wall normal (y) and spanwise directions (z), respectively.

## 5.7 The reference database

The reference database for the DNS results is stored in the ECC-SMART share point and presently only contains the fully developed flow cases. A description of these cases is provided in the preceding section.

D3.1 Report summarizing the newly generated reference data for natural convection, forced and mixed convection and decay heat removal

The data contained in the reference database is presented in non-dimensional form. In the methodology sub-section, the non-dimensionalisation approach is discussed. Fluid property values at the inlet temperature, the reference enthalpy, and dimensional half-channel height, which are necessary to non-dimensionalise the variables are provided here.

The half channel height ( $\delta^*$ ) is 0.0015 m, the Reynolds number based on the half channel height is 2800. The inlet temperature is 640.15 K and the thermal properties are; density ( $\rho_0^*$ ) is 505.116 kg/m<sup>3</sup>, dynamic viscosity ( $\mu_0^*$ ) is  $5.818 \times 10^{-5}$  Pa.s, thermal conductivity ( $\kappa_0^*$ ) is 0.42 W/(m.K) and thermal capacity ( $Cp_0^*$ ) is  $1.462 \times 10^4$  J/(kg K). The reference temperature is 900 K and the reference enthalpy is  $3.584 \times 10^{-5}$  J/kg.

The reference database will contain four text files (one text file per case). In each text file a single-line profile is stored. This is because the statistical variables contained in the repository are space and time averaged. A list of the variables contained in the repository is listed here.

- For the first-order statistics we have:  $\bar{u}$ ,  $\bar{v}$ ,  $\bar{w}$ ,  $\bar{T}$ ,  $\bar{h}$ ,  $\bar{\rho}$ ,  $\bar{Cp}$ ,  $\bar{\kappa}$ .
- The Reynolds averaged normal and shear stresses:  $\overline{u'u'}$ ,  $\overline{v'v'}$ ,  $\overline{w'w'}$ ,  $\overline{u'w'}$ ,  $\overline{v'w'}$ ,  $\overline{u'v'}$ .
- Favre averaged normal and shear stresses:  $\overline{\rho u''u''}$ ,  $\overline{\rho v''v''}$ ,  $\overline{\rho w''w''}$ ,  $\overline{\rho u''w''}$ ,  $\overline{\rho u''v''}$ ,  $\overline{\rho v''w''}$ .
- Reynolds averaged turbulent heat fluxes:  $\overline{u'h'}$ ,  $\overline{v'h'}$ ,  $\overline{w'h'}$
- Favre averaged turbulent  $\overline{\rho u''h''}$ ,  $\overline{\rho v''h''}$ ,  $\overline{\rho w''h''}$ .

Profiles of some of the variables contained in the repository are shown from Figure 45 to Figure 48.

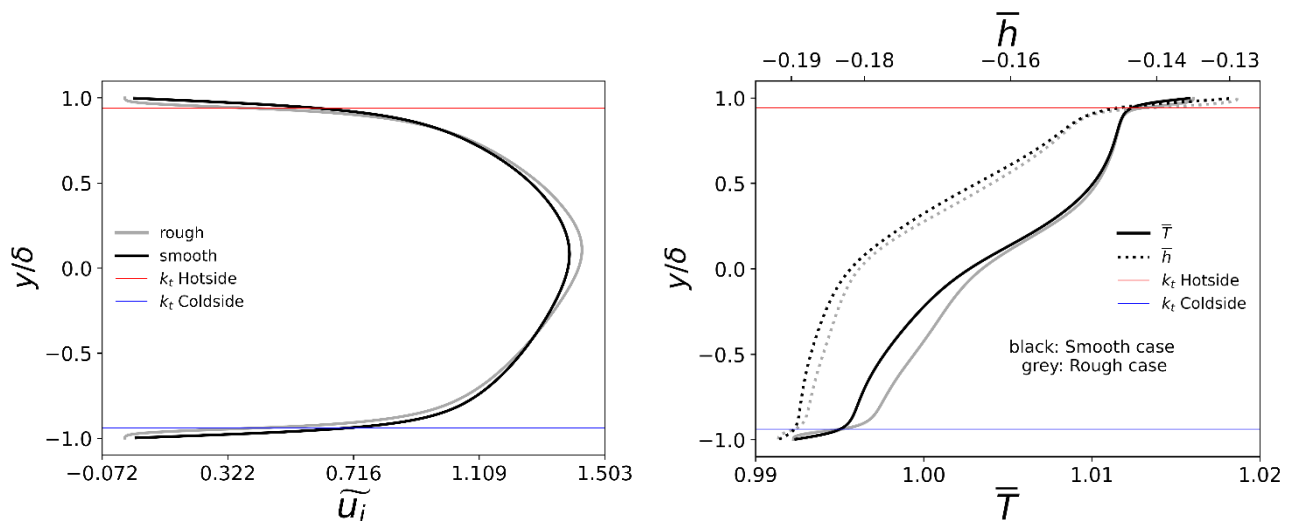


Figure 45: Horizontal flow profiles for Favre averaged velocity (left) plus temperature and enthalpy (right). Black lines are for smooth case (SB2800-H) and grey for rough case (PB2800-H). Red and blue horizontal lines denote the peak roughness height on the hot and cold wall, respectively.

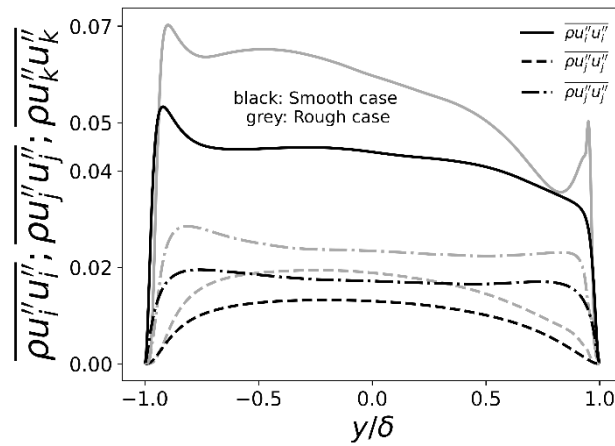


Figure 46: Vertical flow profile for the normal Favre averaged cases for the smooth case (SB2800-V) and rough case (PB2800-V).

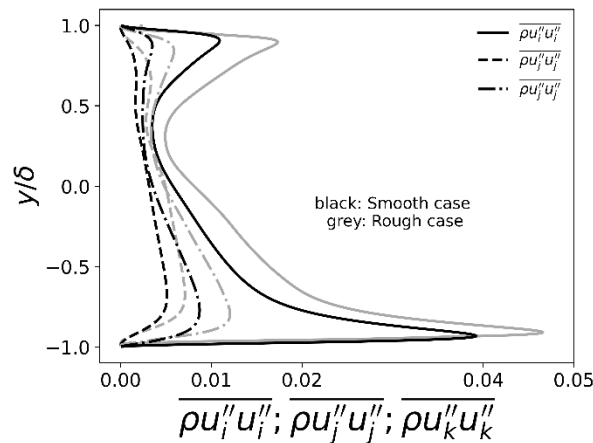


Figure 47: Horizontal flow profiles for the normal Favre averaged stresses for the smooth case (SB2800-H) and rough case (PB2800-H).

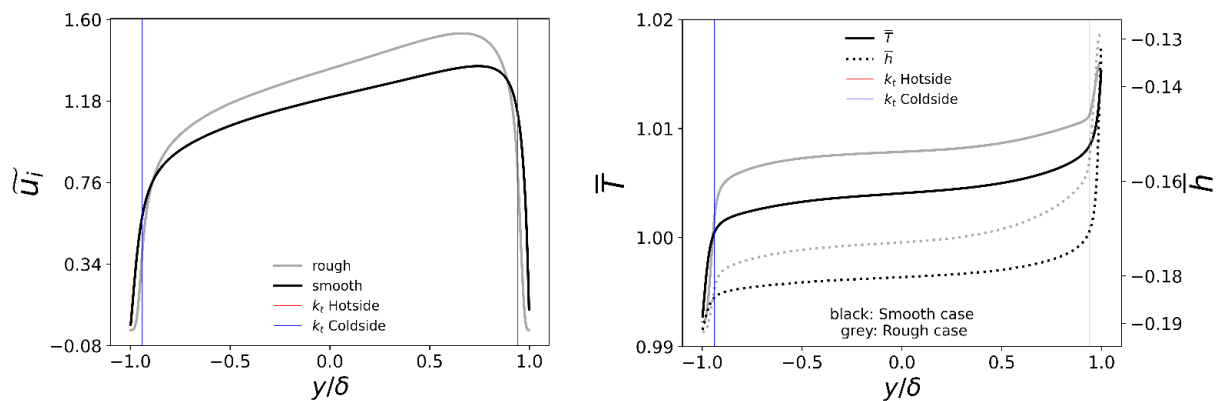


Figure 48: Vertical flow profiles for Favre averaged velocity (left) plus temperature and enthalpy (right). Black lines are for smooth case (SB2800-V) and grey for rough case (PB2800-V). Red and blue vertical lines denote the peak roughness height on the hot and cold wall, respectively.

## 6 Numerical simulations of turbulent heat transfer under supercritical pressure conditions (KIT)

### 6.1 Introduction

The aim of the work performed at KIT within the Subtask 3.2.5, DNS of turbulent heat transfer under supercritical pressure conditions (KIT), is

- to develop a customized fully compressible Direct Numerical Simulation (DNS) solver for open source CFD code OpenFOAM®,
- to validate the solver based on the data from the literature,
- to perform DNS of turbulent heat transfer in water under supercritical pressure conditions
- provide data for the reference data base for turbulent natural convection in water at supercritical pressure conditions.

In the following the work performed at KIT is presented.

To improve simulation strategies for turbulent natural convection at low and supercritical pressure conditions we have developed an optimization approach for heat transfer similarity analysis. This approach is presented in the next section.

### 6.2 Optimization approach for heat transfer similarity analysis

In Otic 2024, we introduce a Physics Informed Optimization (PIO) approach which provides a systematic method for scaling natural convection problems from air to water while maintaining key dimensionless parameters. By optimizing the geometry and temperature difference while maintaining consistent Rayleigh- and Nusselt-numbers, it allows for flexible adaptation to different fluids and conditions while preserving the essential physics of the problem.

The key features of our optimization algorithms are:

- It handles bound constraints on variables, crucial for maintaining physical meaningfulness of our parameters.
- It uses a limited-memory technique to approximate the Hessian matrix, making it efficient for our optimization problem.
- It employs gradient information to navigate the complex landscape of our objective function

The method iteratively improves the solution through the following process:

- It maintains a history of the  $m$  most recent updates to the optimization vectors and the corresponding gradients.
- Using these vectors, it constructs a low-rank approximation of the inverse Hessian matrix, representing the curvature of the objective function.
- This approximation is updated at each iteration using the Sherman-Morrison formula, allowing for efficient updates of the matrix inverse.
- The algorithm computes a step direction using this approximated Hessian.
- It then projects this step onto the feasible region defined by the bounds using an active set strategy.
- A line search is performed along this projected direction to ensure sufficient decrease in the objective function.

This process allows the algorithm to make "intelligent" steps towards the optimum by:

- Using curvature information to determine both the direction and size of each step.

D3.1 Report summarizing the newly generated reference data for natural convection, forced and mixed convection and decay heat removal

- Respecting the defined bounds through the projection step.
- Ensuring each step leads to an improvement in the objective function value.

This approach allows for the scaling of natural convection problems from air to water while maintaining the Rayleigh number and aspect ratios, and adjusting the Fourier number to a desired value. It provides insights into how geometry and temperature difference need to change to achieve specific dimensionless parameters in different fluids. The optimization approach is first applied for the validation of the customized CFD solver.

A custom fully compressible OpenFOAM (see OpenFOAM, 2024) DNS solver was developed with capabilities to incorporate temperature-dependent fluid properties through data tables during runtime. The computational domain and boundary conditions were configured according to the similarity parameters to ensure direct comparability with the reference case.

Doing so, we are able to validate both:

- the PIO approach and
- the customized fully compressible OpenFOAM solver.

The similarity approach is validated by comparing existing experimental data for air at low pressure with our Direct Numerical Simulation (DNS) results for water. The DNS computations were performed using a specialized solver developed for this study.

In the next section we first present the solver.

### 6.3 CFD solver

Mass Conservation:

$$\partial \rho / \partial t + \nabla \cdot (\rho u) = 0$$

Momentum Conservation:

$$\partial (\rho u) / \partial t + \nabla \cdot (\rho u \otimes u) = -\nabla p + \nabla \cdot \tau + \rho g$$

Viscous Stress Tensor:

$$\tau = \mu(\nabla u + \nabla u^T) - (2/3)\mu(\nabla \cdot u)I$$

Energy Conservation (Sensible Enthalpy Form):

$$\partial (\rho h_s) / \partial t + \nabla \cdot (\rho h_s u) = Dp/Dt + \nabla \cdot (k \nabla T) + \Phi$$

Viscous Dissipation:

$$\Phi = \tau : \nabla u$$

Where:

- $\rho$ : Density [kg/m<sup>3</sup>]
- $u$ : Velocity vector [m/s]
- $p$ : Pressure [Pa]
- $T$ : Temperature [K]
- $h_s$ : Sensible enthalpy [J/kg]
- $\mu$ : Dynamic viscosity [Pa·s]
- $k$ : Thermal conductivity [W/(m·K)]
- $c_p$ : Specific heat capacity at constant pressure [J/(kg·K)]

D3.1 Report summarizing the newly generated reference data for natural convection, forced and mixed convection and decay heat removal

- $g$ : Gravitational acceleration [ $m/s^2$ ]
- $\tau$ : Viscous stress tensor [Pa]
- $\Phi$ : Viscous dissipation [ $W/m^3$ ]
- $I$ : Identity tensor [-]

All fluid properties:

- Density:  $\rho = \rho(T, p)$
- Dynamic Viscosity:  $\mu = \mu(T, p)$
- Thermal Conductivity:  $k = k(T, p)$
- Specific Heat Capacity:  $c_p = c_p(T, p)$
- Sensible Enthalpy:  $h_s = \int_{T_{ref}}^T c_p(T', p) dT'$
- Pressure:  $p = p(\rho, T)$

are iteratively obtained from temperature and pressure dependent data tables during the simulation runtime.

## 6.4 Simulation setup and results

### 6.4.1 Reference case

Starting from the experimental case of turbulent natural convection in a tall, differentially heated rectangular cavity DNS simulations are performed. Geometry and boundary conditions correspond to the experimental setup by Betts and Bokhari, 2000.

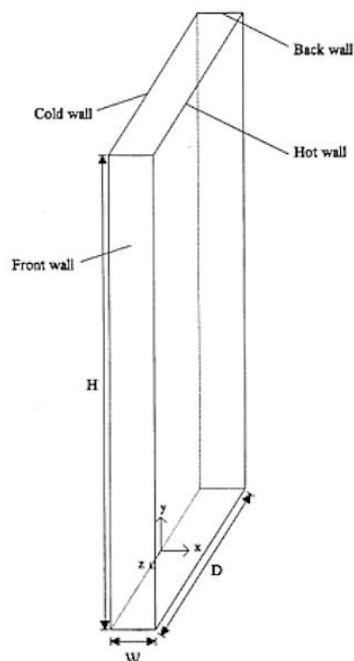


Figure 49: Geometry sketch

D3.1 Report summarizing the newly generated reference data for natural convection, forced and mixed convection and decay heat removal

The geometry sketch of the cavity is given in Figure 49: Geometry sketch where  $W=76$  mm,  $H=2180$  mm and  $D=520$  mm are width, height and depth, respectively. The temperature differences between the hot and cold vertical walls is  $19.6$  °K.

Experimental data by Betts and Bokhari 2000, used for comparisons are available at: <http://cfd.mace.manchester.ac.uk/ercoftac/doku.php?id=cases:case079>. These data are also considered as ERCOFTAC benchmark case for natural convection

To perform comparisons between natural convection convection cases for different fluids we performed the PIO approach briefly introduced previously, Otic 2024. The optimization approach determines equivalent parameters for water at supercritical pressure to achieve similar heat transfer characteristics. The width  $W$  from Betts and Bokhari 2000, is rescaled based on the PIO approach together with the estimate for  $\Delta T$ . Aspect ratios of the geometry from Betts and Bokhari 2000, Figure 1, are also preserved. The parameters are given in Table 6-1. Four simulation cases are considered in this report and summarized in Table 6-1. The cases Air L and Air L correspond to the cases reported in [1]. These cases are used for the validation of the OpenFOAM solver and of the PIO approach. Cases Water Sub and Water PC in Table 6-1 are new DNS simulations of natural convection in a closed cavity for water at 25 MPa.  $T_c$  and  $T_h$  assign the cold and hot wall temperature of the differentially heated cavity, respectively (see Figure 49).

Table 6-1 Cases considered for the simulation

Parameter	Air L	Air H	Water Sub	Water PC
Ra	$8.6 \times 10^5$	$1.6 \times 10^6$	$8.6 \times 10^5$	$1.9 \times 10^8$
MPa	0.1013	0.1013	25	25
$T_c$ (°K)	288.25	288.75	557.965	654
$T_h$ (°K)	327.85	307.85	580.035	664
Mesh in H	296	296	296	320
Mesh in W	104	104	104	124
Mesh in D	124	124	124	144

## 6.4.2 Computational Mesh and Initial Fields

Near wall mesh is constructed as parabolic near-wall mesh refinement. This task is performed by implementation of a dedicated script for snappyHexMesh subroutine of the OpenFOAM. The well known DNS strategy to generate refined mesh layers near walls with a parabolic distribution is particularly beneficial for capturing transient boundary layer phenomena. This is of particular importance for convection at supercritical pressures.

It is important to notice that the case Water PC, which is at higher Rayleigh number (Ra), is performed for the mesh resolution which can only be considered as "coarse mesh"-DNS, (see Table 1). However, this resolution appears to be sufficient for the first order statistics. For the second order statistics, additional simulations at higher resolution are ongoing and will be provided to the project partners later.

Of particular importance for direct numerical simulations is the initial field generation. Well chosen initial field may considerably contribute to convergence of the simulation case.

D3.1 Report summarizing the newly generated reference data for natural convection, forced and mixed convection and decay heat removal

To improve the initial field set up we provide an approach for initializing non-uniform velocity (U) and temperature (T) fields with perturbations in OpenFOAM 11, using the codeStream utility. The full initialization code for both U and T fields is provided below:

### Velocity Field (0/U)

```

internalField #codeStream
{
  codeInclude
  #{
    #include "fvMesh.H"
    #include "volFields.H"
    #include "Random.H"
  #};
  codeOptions
  #{
    -I$(LIB_SRC)/finiteVolume/InInclude \
    -I$(LIB_SRC)/meshTools/InInclude
  #};
  codeLibs
  #{
    -lfiniteVolume \
    -lmeshTools
  #};
  code
  #{
    const IOdictionary& d = static_cast<const IOdictionary&>(dict);
    const fvMesh& mesh = refCast<const fvMesh>(d.db());

    // Read base U field
    volVectorField Ubase
    (
      IOobject
      (
        "U_base",
        mesh.time().constant(),
        mesh,
        IOobject::MUST_READ,
        IOobject::NO_WRITE
      ),
      mesh
    );

    scalar uPrimeRatio = 0.1; // RMS of fluctuations (10% of local velocity magnitude)
    Random ranGen(1234); // Random number generator
    vectorField U(mesh.nCells());

    forAll(U, cellI)
    {
      scalar localUMag = mag(Ubase[cellI]);
      scalar uPrime = uPrimeRatio * localUMag;
      vector fluct(
        uPrime * (2.0*ranGen.scalar01() - 1.0),

```

```

    uPrime * (2.0*ranGen.scalar01() - 1.0),
    uPrime * (2.0*ranGen.scalar01() - 1.0)
  );
  U[cellI] = Ubase[cellI] + fluct;
}
writeEntry(os, "", U);
#};
};

```

### Temperature Field (0/T)

```
internalField #codeStream
```

```

{
  codeInclude
  #{
    #include "fvMesh.H"
    #include "volFields.H"
    #include "Random.H"
  #};
  codeOptions
  #{
    -I$(LIB_SRC)/finiteVolume/lnInclude \
    -I$(LIB_SRC)/meshTools/lnInclude
  #};
  codeLibs
  #{
    -lfvMesh \
    -lmeshTools
  #};
  code
  #{
    const IOdictionary& d = static_cast<const IOdictionary&>(dict);
    const fvMesh& mesh = refCast<const fvMesh>(d.db());

    // Read base T field
    volScalarField Tbase
    (
      IOobject
      (
        "T_base",
        mesh.time().constant(),
        mesh,
        IOobject::MUST_READ,
        IOobject::NO_WRITE
      ),
      mesh
    );

    scalar tPrime = 1.0; // RMS of temperature fluctuations
    Random ranGen(5678); // Different seed from velocity
    scalarField T(mesh.nCells());

    forAll(T, cellI)

```

D3.1 Report summarizing the newly generated reference data for natural convection, forced and mixed convection and decay heat removal

```

    {
        scalar fluct = tPrime * (2.0*ranGen.scalar01() - 1.0);
        T[cellI] = Tbase[cellI] + fluct;
    }
    writeEntry(os, "", T);
#};
};

```

## 6.5 Solver Validation

To reach higher accuracy of the results, all DNS simulations reported here are performed with four pressure corrections at each time step using geometric-algebraic multigrid solver. For all simulations the maximum Courant number is kept below 0.4 while the mean Courant number was around 0.05. Apart of pressure, all other fields are solved using Diagonal Incomplete Cholesky (DIC) preconditioner along with the conjugate gradient method.

Table 6-2 summarizes  $y^+$  values for different surfaces for the case **Air H**. Near wall and overall resolution for the case **Air L** was clearly finer since the Ra in case **Air L** is lower for the same mesh cell number.

Table 6-2:  $y^+$  Values for Different Surfaces

Surface	Min $y^+$	Max $y^+$	Average $y^+$
Top	0.00617666	0.408458	0.235863
Bottom	0.00753303	0.442914	0.259219
Front	0.00666859	0.290961	0.169612
Back	0.00666867	0.290952	0.169612
Hot	0.00523152	0.158902	0.0881149
Cold	0.00432707	0.149267	0.0821662

In Figure 50 we present the comparison between the experimental results by Betts and Bokhari 2000, case **Air L**, with the numerical results for the validation. In Figure 51 the case **Air H** is compared, see also Table 1. Figure 50 and Figure 51 show vertical mean temperature profiles for different height positions of the cavity. All data, experimental and numerical, are taken at the mid plane at  $d=D/2$ . All results are presented dimensionless and the position  $y/H=0.5$  means that the data are taken at the half height  $H/2$ . The results show that our approach and the DNS solver agreement with experimental results for the first order statistics.

## 6.6 DNS of natural convection in water at supercritical pressure conditions

After validating the OpenFOAM solver, we proceed to set up new Direct Numerical Simulations (DNS). The cases for these simulations are detailed in Table 1. Each DNS simulation reported here employs four pressure correction steps per time step, utilizing a geometric-algebraic multigrid solver to enhance convergence.

For all simulations, the maximum Courant number is maintained below 0.4, while the average Courant number is approximately 0.05, ensuring numerical stability and temporal accuracy. All fields, with the exception of pressure, are solved using a Diagonal Incomplete Cholesky (DIC) preconditioner in conjunction with the conjugate gradient (CG) method. This approach optimizes computational efficiency and stability for the solution of the discretized governing equations, providing accurate resolution of the flow fields within the specified numerical constraints.

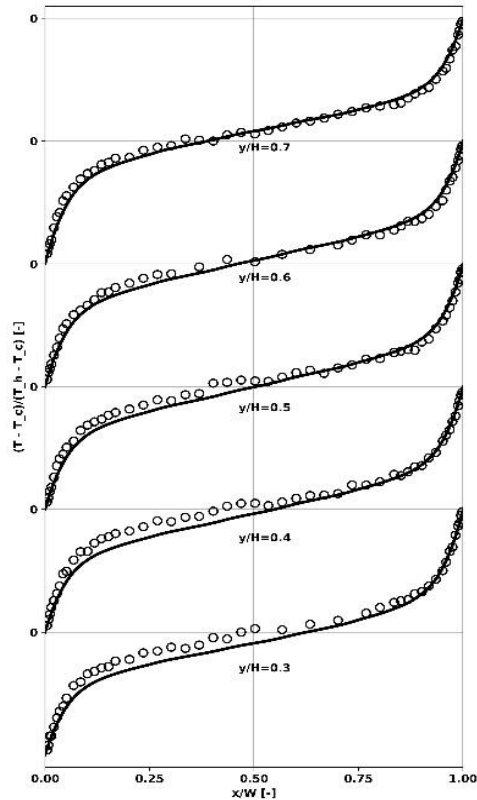


Figure 50: Mean temperature, Air L

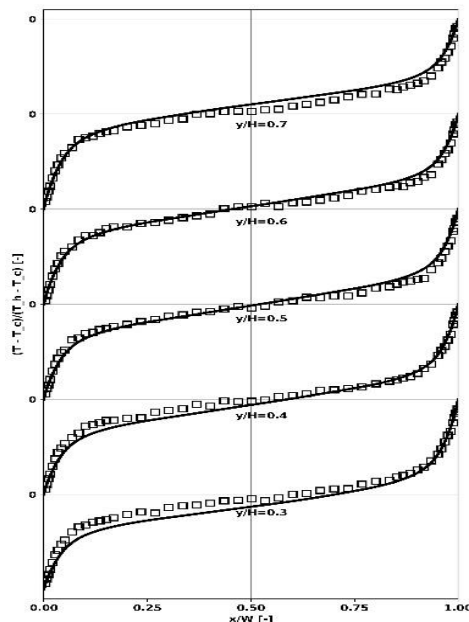


Figure 51: Mean temperature Air H

Table 6-3 summarizes  $y^+$  values for different surfaces for the case **Water PC**.

The mesh resolution for the case **Water Sub** was comparable to the mesh resolution of validation cases listed in Table 1. For the case **Water PC** the near wall resolution was slightly coarser as compared to the

D3.1 Report summarizing the newly generated reference data for natural convection, forced and mixed convection and decay heat removal

case Water Sub but the mesh expansion from walls to the bulk of the cavity was much higher than in the case Water Sub. Hence, we consider the case **Water PC** as coarse-mesh DNS.

Table 6-3:  $y^+$  Values for Different Surfaces

Surface	Min $y^+$	Max $y^+$	Average $y^+$
Top	0.0199884	1.56111	0.797694
Bottom	0.0252019	2.60398	1.27652
Front	0.0182139	2.64987	1.18936
Back	0.0199884	3.35647	1.18928
Hot	0.0251958	1.00834	0.65544
Cold	0.0199885	1.00559	0.666991

Comparison of the mean temperature vertical profiles given in Figure 52 shows the key difference in the temperature distribution for the sub-critical temperature range of 550°K - 580°K and the super-critical temperature range of 654°K - 664°K. In the small temperature range of  $\pm 15^\circ\text{K}$  around the pseudo-critical temperature of  $\sim 662^\circ\text{K}$  at 25 MPa the fluid properties changing strongly and so is the Rayleigh number change in this range. In the DNS case presented here the results are in the range 654°K - 664°K where the Rayleigh number reaches its maximum for  $\sim 662^\circ\text{K}$  which is very close to the hot wall.

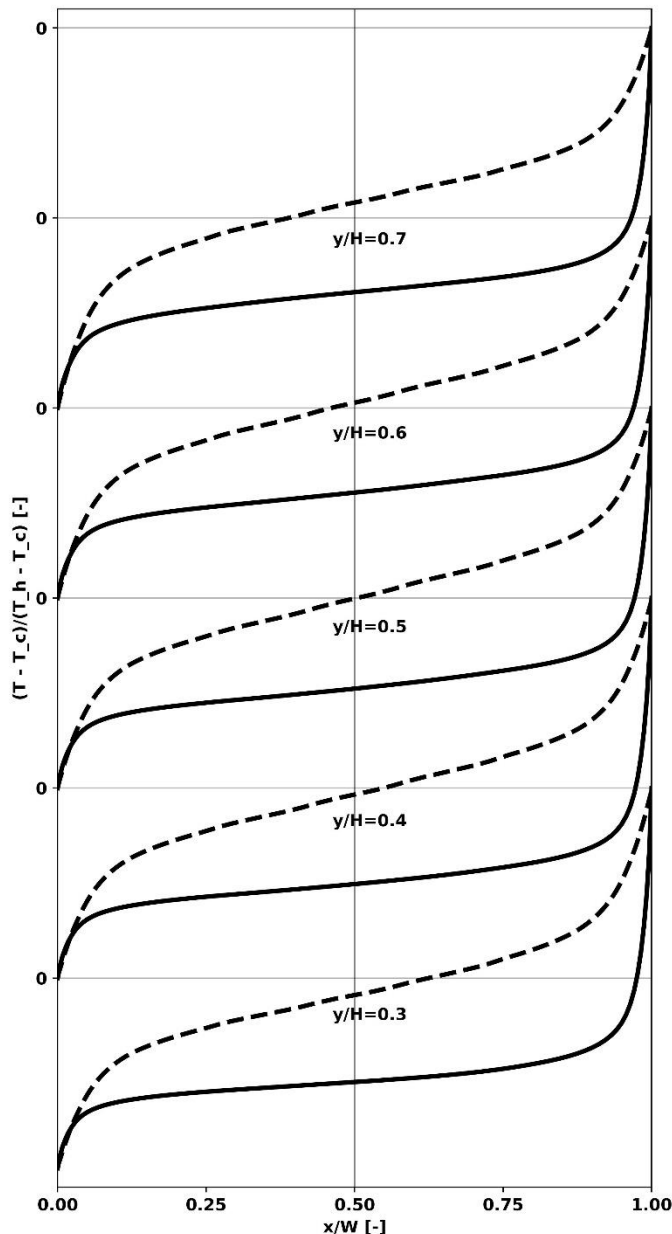


Figure 52: Vertical profile of the mean temperature;  
 — solid line represents results for case **Water PC** in Table 1;  
 - - dashed line represents results for case **Water Sub** in Table 1.

Afterwards the Rayleigh number ( $Ra$ ) will strongly decrease towards the bulk of the flow providing vertically asymmetric temperature profiles, as shown in Figure 52, — solid line, what is in opposite to the vertically symmetric profile of sub critical case Water Sub, as shown in FFigure 52, - - dashed line.

## 6.7 Summary and Outlook

The research conducted under Subtask 3.2.5 focuses on turbulent heat transfer under supercritical pressure conditions, with following primary objectives:

- Development of a customized DNS solver for OpenFOAM®, specifically designed for fully compressible flows
- Development of mesh-generation subroutines for OpenFOAM

D3.1 Report summarizing the newly generated reference data for natural convection, forced and mixed convection and decay heat removal

- Validation of the solver against established literature data
- DNS for turbulent heat transfer in supercritical water

Another achievement is the development of a Physics Informed Optimization (PIO) approach that:

- Enables systematic scaling of natural convection problems from air to water
- Provides flexible adaptation across different fluids while preserving fundamental physics

This PIO approach provides a systematic method for scaling natural convection problems from air to water while maintaining key dimensionless parameters. By optimizing both the geometry and the Nu correlation, it allows for flexible adaptation to different fluids and conditions while preserving the essential physics of the problem.

The development of the customized fully compressible DNS solver enables further research and development based on the open source CFD software OpenFOAM®.

These DNS investigations will provide essential insights for improving engineering-level CFD models and advancing our fundamental understanding of supercritical fluid behavior in heat transfer applications.

## 7 Assembling the existing experimental data base (IPP)

The goal of subtask 3.2.6 was to assemble existing experimental data collected and obtained within the project and present it in the form of a database. This section provides a brief description of the features and form of the proposed and generated database. The general view of such a database should first of all be universal and reflect all possible parameters regarding the coolant, operating conditions, geometric characteristics of test sections, as well as the measurement data themselves.

The formation of the experimental database included two stages: at the first stage, the array of data available in the literature and from IPP was processed and the first version was compiled, after which, at the second stage, its expansion with the new experimental data obtained within the framework of the project (see sections 3 and 4) is considered. In general, based on the specifics of the available experiments, the entire data array was divided into categories corresponding to fundamentally different geometric configurations of the test sections - the Bare tube and Rod bundles (FA's simulators). These categories are placed in separate tables (document sheets). An additional table contains some of the data from the JIHTRAS test facility, the key feature of which is the presence of experimental radial profiles, useful for validating the CFD models. The expansion of this third table by the results of Direct Numerical Simulations is considered in the form of the data from points placed in chosen cross sections of the test section. The proposed first version of database includes experimental data for both bare tubes (NTUU Test facility (Razumovskiy), JIHTRAS Test facility (Kurganov), IPPE test facility (Kirillov), MSTF lab test facility (Katsuyoshi), Yamagata's test facility, Adebisi's test facility and Bazargan's test facility) and rod bundles test sections (1-rod, 3-rod and 7-rod bundles data from NTUU Test facility (Razumovskiy)). A short specification of the formed database is presented in Table 8.1. The more detailed description of the listed experimental facilities and the corresponding regime parameters could be found in ECC-SMART Deliverable - D.3.2. Report on the results of the benchmark exercise.

Table 8.2 - Table 8.4 provide the specifications of the data sets for selected categories – Bare tubes, Rod bundles and Data set with experimental radial profiles.

Table 8.1: Collected experimental data specification

Geometry type	Facility (Reference)	Coolant	Flow direction	Number of regimes
<b>Bare Tube</b>	NTUU Test facility (Razumovskiy) (Razumovskiy et al. 2009), (Razumovskiy et al. 2016), (IAEA-TECDOC-1900, 2020)	H <sub>2</sub> O	Vertical (Upward/Downward)	26/2
	JIHTRAS Test facility (Kurganov) (Kurganov et al., 1992), (Kurganov et al., 1993), (Kurganov et al., 2018)	CO <sub>2</sub>		13/10
	IPPE test facility (Kirillov) (Mokry, Kirillov et al., 2010) (Mokry, Pioro et al., 2010)	H <sub>2</sub> O		24/-
	MSTF lab test facility (Katsuyoshi) (Katsuyoshi et al., 2015)	CO <sub>2</sub>	Horizontal	11

## D3.1 Report summarizing the newly generated reference data for natural convection, forced and mixed convection and decay heat removal

	Yamagata's test facility (Yamagata et al., 1971)	H <sub>2</sub> O		36
	Adebiyi's test facility (Adebiyi et al., 1976)	CO <sub>2</sub>		34
	Bazargan's test facility (Bazargan et al., 2005)	H <sub>2</sub> O		8
<b>Rod bundles (1-rod, 3-rods, 7-rods)</b>	NTUU Test facility (Razumovskiy) (Razumovskiy et al. 2009), (Razumovskiy et al. 2016), (IAEA-TECDOC-1900, 2020)	H <sub>2</sub> O	Vertical (Upward)	29
<b>Bare Tube with CS Sensor data</b>	JHTRAS Test facility (Kurganov) (Kurganov et al., 1992), (Kurganov et al., 1993), (Kurganov et al., 2018)	CO <sub>2</sub>	Vertical (Upward/Downward)	8/4

Table 8.2: Specification of the data for the Bare tube

Header	Position in file	Description	Header	Position in file	Description
<b>#Regimes (Num)</b>	A	Regime numbering in the file	<b>Author</b>	B	Author of experimental data
<b>#Regimes (Ex)</b>	C	Regime numbering according to the author of the experiment	<b>Direction</b>	D	Flow direction relative to the gravity
<b>TypeGeom</b>	E	Geometry type (adding of the annular channel is possible)	<b>TypeCoolant</b>	F	Type of the studied coolant (e.g. H <sub>2</sub> O/CO <sub>2</sub> )
<b>OD, [mm]</b>	G	Outer diameter	<b>ID, [mm]</b>	H	Inner diameter
<b>P<sub>work</sub>, [MPa]</b>	I	Operating pressure	<b>T<sub>in</sub>, [°C]</b>	J	Inlet temperature
<b>G, [kg/(s*m<sup>2</sup>)]</b>	K	Mass velocity	<b>q<sub>Ave</sub>, [kW/m<sup>2</sup>]</b>	L	Average value of the heat flux in regime
<b>ΔP, [Pa]</b>	M	Pressure drop	<b>L<sub>heat</sub>, [mm]</b>	N	Length of the heated section
<b>#sensors(T)</b>	O	Number of the temperature measurement cross-section	<b>L/ID</b>	P	Specific length of the heated section
<b>q [kg/(s*m<sup>2</sup>)]</b>	Q	Axial profile of the heat flux	<b>T<sub>w</sub>, [°C]</b>	R	Wall temperature
<b>T<sub>f</sub>, [°C]</b>	S	Bulk temperature	<b>h<sub>f</sub>, [kJ/kg]</b>	T	Bulk enthalpy

Table 8.3: Specification of the data for the Rod bundles

Header	Position in file	Description	Header	Position in file	Description
<b>#Regimes (Num)</b>	A	Regime numbering in the file	<b>Author</b>	B	Author of experimental data

## D3.1 Report summarizing the newly generated reference data for natural convection, forced and mixed convection and decay heat removal

<b>#Regimes (Ex)</b>	C	Regime numbering according to the author of the experiment	<b>Direction</b>	D	Flow direction relative to the gravity
<b>TypeCoolant</b>	E	Geometry type (adding of the annular channel is possible)	<b>NumRods</b>	F	Type of the studied coolant (H <sub>2</sub> O and CO <sub>2</sub> )
<b>TPR</b>	G	Rod packing type	<b>StepTPR, [mm]</b>	H	Rod packing step
<b>OD, [mm]</b>	I	Outer diameter	<b>ID, [mm]</b>	J	Inner diameter
<b>D<sub>hydr</sub>, [mm]</b>	K	Hydraulic diameter	<b>S<sub>cs</sub>, [mm<sup>2</sup>]</b>	L	Free cross-sectional area
<b>NumWire</b>	M	Number of screws (wires)	<b>L<sub>w</sub>, [mm]</b>	N	Screws thickness
<b>H<sub>w</sub>, [mm]</b>	O	Screws height	<b>T<sub>zw</sub>, [mm]</b>	P	Screws twist period
<b>P<sub>work</sub>, [MPa]</b>	Q	Operating pressure	<b>T<sub>in</sub>, [°C]</b>	R	Inlet temperature
<b>G, [kg/(s*m<sup>2</sup>)]</b>	S	Mass velocity	<b>q<sub>Ave</sub>, [kW/m<sup>2</sup>]</b>	T	Average value of the heat flux in regime
<b>ΔP, [Pa]</b>	U	Pressure drop	<b>L<sub>heat</sub>, [mm]</b>	V	Length of the heated section
<b>#sensors(T)</b>	W	Number of the temperature measurement cross-section	<b>L/ID</b>	X	Specific length of the heated section
<b>q [kg/(s*m<sup>2</sup>)]</b>	Y	Axial profile of the heat flux	<b>T<sub>w</sub>, [°C]</b>	Z	Wall temperature
<b>T<sub>f</sub>, [°C]</b>	AA	Bulk temperature	<b>h<sub>f</sub>, [kJ/kg]</b>	AB	Bulk enthalpy

Table 8.4: Specification of the data for the Bare tube (with radial profiles)

Header	Position in file	Description	Header	Position in file	Description
<b>#Regimes (Num)</b>	A	Regime numbering in the file	<b>Author</b>	B	Author of experimental data
<b>#Regimes (Ex)</b>	C	Regime numbering according to the author of the experiment	<b>Direction</b>	D	Flow direction relative to the gravity
<b>TypeGeom</b>	E	Geometry type (adding of the annular channel is possible)	<b>OD, [mm]</b>	F	Outer diameter
<b>ID, [mm]</b>	G	Inner diameter	<b>P<sub>work</sub>, [MPa]</b>	H	Operating pressure
<b>T<sub>in</sub>, [°C]</b>	I	Inlet temperature	<b>h<sub>in</sub><sup>*</sup>, [kJ/kg]</b>	J	Inlet flow enthalpy (* - according to the authors' data)
<b>G, [kg/(s*m<sup>2</sup>)]</b>	K	Mass velocity	<b>q<sub>Ave</sub>, [kW/m<sup>2</sup>]</b>	L	Average value of the heat flux in regime
<b>X/D</b>	M	Position of the measurement cross-section relative to the	<b>Tau<sub>wall</sub>, [Pa]</b>	N	Shear stress on the wall

## D3.1 Report summarizing the newly generated reference data for natural convection, forced and mixed convection and decay heat removal

		start of heated section			
<b><math>h_f</math>, [kJ/kg]</b>	O	Bulk enthalpy in current cross section	<b>R/R0</b>	P	Dimensionless radius
<b><math>u/u_f</math></b>	Q	Dimensionless velocity profile ( $u_f$ – average mass velocity)	<b><math>h-h_{in}</math>, [kJ/kg]</b>	R	Enthalpy profile
<b><math>\tau/\tau_{wall}</math></b>	S	Dimensionless shear stress profile	<b><math>q/q_c</math></b>	T	Dimensionless heat flux profile

## References

- Abe, H., Kawamura, H. & Matsuo, Y., 2001, Direct numerical simulation of a fully developed turbulent channel flow with respect to the Reynolds number dependence, Transactions of the ASME, 123(2), pp.382-393
- Adebiyi G.A., Hall W.B., 1976, Experimental investigation of heat transfer to supercritical pressure carbon dioxide in a horizontal pipe, Int. J. Heat Mass Transfer. Volume 19, Issue 7, pp. 715-720, [https://doi.org/10.1016/0017-9310\(76\)90123-X](https://doi.org/10.1016/0017-9310(76)90123-X)
- Amirkhiz B. S., Xu, S. and Scott, C., 2019. Microstructural assessment of 310S stainless steel during creep at 800 °C, Materialia, vol. 6, doi: 10.1016/j.mtla.2019.100330.
- Azih C. and Yaras, M.I., 2018, "Effects of Spatial Gradients in Thermophysical Properties on the Topology of Turbulence in Heated Channel Flow of Supercritical Fluids," Phys. Fluids 30, 015108
- Bae J.H., Yoo J.Y, Choi H, 2005, Direct numerical simulation of turbulent supercritical flows with heat transfer. Physics of Fluids, 17(10).
- Bazargan M., Fraser D., Chatoorgan V., 2005, Effect of Buoyancy on Heat Transfer in Supercritical Water Flow in a Horizontal Round Tube, J. Heat Transfer. 127(8): pp. 897-902, <https://doi.org/10.1115/1.1929787>
- Betts P.L., and Bokhari I.H. 2000. Experiments in turbulent natural convection in an enclosed tall cavity. International Journal of Heat and Fluid Flow, 21:675–683.
- Cao, Y. and Di, H., 2015, Research on the hot deformation behavior of a Fe-Ni-Cr alloy (800H) at temperatures above 1000 °C, J. Nucl. Mater., vol. 465, pp. 104–115, doi: 10.1016/j.jnucmat.2015.05.014.
- Chen J., Yang S., Zhao R. and Cheng W.-L. 2022. „Experimental study on the effect of wall roughness on heat transfer characteristics of supercritical carbon dioxide in vertical tubes, International Journal of Heat and Mass Transfer, Nr. 196.
- Cheng, X. und Liu, X.J., Gu, H.Y, 2011. Fluid-tofluid scaling of heat transfer in circular tubes cooled with supercritical fluids. Nuclear Engineering and Design, 241.
- Copping A.W. and Yaras M.I., 2022. "Convective Heat Transfer at Supercritical Pressure in the Presence of Surface Roughness - A Literature Review," Carleton University, Department of Mechanical Aerospace Engineering, Ottawa.
- Das S., Panda A., Deen N.G., Kuipers J.A.M., 2018, A sharp-interface Immersed Boundary Method to simulate convective and conjugate heat transfer through highly complex periodic porous structures. Chemical Engineering Science, 191:1–18.
- Eckelmann H. 1974. "The structure of the viscous sublayer and the adjacent wall region in a turbulent channel flow". Journal of fluid Mechanics, 65(3), 439-459.

D3.1 Report summarizing the newly generated reference data for natural convection, forced and mixed convection and decay heat removal

Fadlun E. A., Verzicco R., Orlandi P., Mohd-Yusof J., 2000, Combined Immersed Boundary Finite Difference Methods for Three-Dimensional Complex Flow Simulations. *Journal of Computational Physics*, 161(1):35–60.

He J., Tian R., Jiang P.X., He J, 2021, Turbulence in a heated pipe at supercritical pressure, *Journal of Fluid Mechanics*, 920:45.

Herkenrath H. , 1967. Wärmeübergang an Wasser bei erzwungener Strömung im Druckbereich von 140 bis 250 bar (in German), Ispra, Italy: Europäische Atomgemeinschaft, EURATOM.

IAEA, 2008. Analysis of Severe Accidents in Pressurized Heavy Water Reactors, IAEA-TECDOC-1594, IAEA, Vienna (2008)

IAEA, 2013. Benchmarking Severe Accident Computer Codes for Heavy Water Reactor Applications, IAEA-TECDOC-1727, IAEA, Vienna (2013)

IAEA, 2014. Heat Transfer Behaviour and Thermohydraulics Code Testing for Supercritical Water Cooled Reactors (SCWRs), IAEA-TECDOC-1746, IAEA, Vienna (2014).

IAEA, 2016. Safety of Nuclear Power Plants: Design, IAEA Safety Standards Series No. SSR-2/1 (Rev. 1), IAEA, Vienna (2016)

IAEA, 2019a. Status of Research and Technology Development for Supercritical Water Cooled Reactors, IAEA-TECDOC-1869, IAEA, Vienna (2019)

IAEA, 2019b. Status and Evaluation of Severe Accident Simulation Codes for Water Cooled Reactors, IAEA-TECDOC-1872, IAEA, Vienna (2019)

IAEA, 2020a, Understanding and Prediction of Thermohydraulic Phenomena Relevant to Supercritical Water Cooled Reactors (SCWRs), IAEA-TECDOC-1900, IAEA, Vienna (2020).

IAEA 2020b, Advances in Small Modular Reactor Technology Developments, A Supplement to: IAEA Advanced Reactors Information System (ARIS), 2020 Edition, Printed by the IAEA in Austria, September 2020.

IAPWS 2009, Revised release on the IAPWS formulation 1995 for the thermodynamic properties of ordinary water substance for general scientific use, The International Association for the Properties of Water and Steam.

ISO 4287:1997, Geometrical Product Specifications (GPS) - Surface texture: Profile method - Terms, definitions and surface texture parameters.

Katsuyoshi T., Reza S., 2015, Experimental investigation of buoyancy effects on convection heat transfer of supercritical CO<sub>2</sub> flow in a horizontal tube. *Heat and Mass Transfer* 52(4), <http://dx.doi.org/10.1007/s00231-015-1580-9>

Kawamura H., Ohsaka K., Abe H., and Yamamoto K. 1998. "DNS of turbulent heat transfer in channel flow with low to medium-high Prandtl number fluid", *International Journal of Heat and Fluid Flow*, 19(5), 482-491.

Kim J., Moin P., 1985, Application of a fractional-step method to incompressible Navier-Stokes equations, "Journal of Computational Physics", 59(2), 308–323, [https://doi.org/10.1016/0021-9991\(85\)90148-2](https://doi.org/10.1016/0021-9991(85)90148-2)

D3.1 Report summarizing the newly generated reference data for natural convection, forced and mixed convection and decay heat removal

Kim, J., Moin, P., Moser R.D., 1987, Turbulence statistics in fully developed channel flow and low Reynolds number, *Journal of Fluid Mechanics*, 177, pp.133-166.

Lele, SK, 1992, Compact finite difference schemes with spectral-like resolution, *Journal of Computational Physics*, 103(1):16–42.

Li, X., Hashimoto, K., Tominaga, Y., Tanahashi, M., Miyauchi, T., 2008, Numerical study of heat transfer mechanism in turbulent supercritical CO<sub>2</sub> channel flow, *J. Therm. Sci. Technol.* 3, 12.

Lemmon E, Huber M, and McLinden M, 2010, NIST Standard Reference Database 23: Reference Fluid Thermodynamic and Transport Properties (REFPROP), Version 9.0.

Mann A., Copping A.W., Yaras M. I., 2023, DNS study of thermohydraulic effects of surface roughness in boundary layer and channel flows with application to heated channel flow of water near pseudocritical temperature, Carleton University, Department of Mechanical Aerospace Engineering, Ottawa

Niino M., Suzuki A., Kumakawa A., Sakamoto H. and Sasaki M., 1979. „Heat Transfer Characteristics of Liquid Hydrogen at Supercritical Pressure,“ National Aerospace Laboratory of Japan.

Mokry S., Kirillov P., Pioro I., Gospodinov Y., 2010, Supercritical Water Heat Transfer in a Vertical Bare Tube: Normal, Improved, and Deteriorated Regimes, *Nuclear Technology*, 172:1, 60-70, <http://dx.doi.org/10.13182/NT10-A10882>

Mokry S., Pioro I., Kirillov P., Gospodinov Y., 2010, Supercritical-water heat transfer in a vertical bare tube, *Nuclear Engineering and Design*, V. 240(3), 2010, p. 568-576, <https://doi.org/10.1016/j.nucengdes.2009.09.003>.

Nemati H, Patel A, Boersma B J., Pecnik R, 2016, The effect of thermal boundary conditions on forced convection heat transfer to fluids at supercritical pressure. *Journal of Fluid Mechanics*, 800:531–556.

Oka, Y., Koshizuka, S., Ishiwatari, Y., Yamaji, A., 2010. *Super Light Water Reactors and Super Fast Reactors: Supercritical-Pressure Light Water Cooled Reactors*. Springer.

Peeters J. W.R., Pecnik R., Rohde M., Van Der Hagen T. H.J.J., Boersma B. J, 2017, Characteristics of turbulent heat transfer in an annulus at supercritical pressure. *Physical Review Fluids*, 2(2):1–24.

Pioro, I.L., Duffey, R.B., 2007. *Heat Transfer and Hydraulic Resistance at Supercritical Pressure in Power Engineering Applications*. ASME Press, New York.

Otic, I., 2024. Physics informed optimization approach for similarity analysis of turbulent natural convection at low and supercritical pressure, Submitted for publication.

OpenFOAM, 2024. The Open Source CFD Toolbox. OpenCFD Ltd. (ESI Group). <https://www.openfoam.com>

Schulenberg, T., Starflinger, J., 2012. *High Performance Light Water Reactor: Design and Analyses*. KIT Scientific Publishing.

D3.1 Report summarizing the newly generated reference data for natural convection, forced and mixed convection and decay heat removal

Schulenberg, T., and Otic, I. (March 15, 2022). "Concept of a Small Modular SCWR With Horizontal Fuel Assemblies." ASME. *ASME J of Nuclear Rad Sci.* July 2022; 8(3): 031104. <https://doi.org/10.1115/1.4052191>

Seddighi M., He S., Pokrajac D., O'Donoghue T., Vardy A. E, 2015, Turbulence in a transient channel flow with a wall of pyramid roughness. *Journal of Fluid Mechanics*, 781(October):226–260.

Razumovskiy V.G., Pis'mennyy E.N., Koloskov A.E., and Piro I.L., 2009, "Heat transfer to supercritical water in vertical 7-rod bundle", *Proceedings of the ICONE-16, 2009*, pp. 963-969.

Razumovskiy V.G., Pis'mennyi Eu. N., Sidawi Kh. , Piro, I. L., Koloskov A. Eu., 2016, "Experimental heat transfer in an annular channel and 3-rod bundle Cooled with upward flow of supercritical water", *JNERS*, Vol. 2, Iss.1, 2016, pp 1-8.

Tanaka H., Nishiwaki N., Hirata M. and Tsuge A., 1971. „Forced Convection Heat Transfer to Fluid Near Critical Point Flowing in Circular Tube,“ *International Journal of Heat and Mass Transfer*, Nr. 14, pp. 739-750.

Tseng Y., Ferziger J., 2003, A ghost-cell immersed boundary method for flow in complex geometry, *Journal of Computational Physics*, pp 593-623.

Vít j., Šípová M., Bricín D., 2024, Treatment and evaluation of surface roughness of fuel cladding for heat transfer experiments in supercritical fluids, *Conference Proceedings of International Symposium on Supercritical Water Cooled Reactors (ISSCWR-11)*, Pisa, 3-5 February, 7 pages.

Yamagata K., Nishikawa K., Hasegawa S., Fujiiand T., Yoshida S., 1971, Forced Convective Heat Transfer To Supercritical Water Flowing In Tubes, *Int. J. Heat Mass Transfer*. Vol. 15, pp. 2575-2593, [https://doi.org/10.1016/0017-9310\(72\)90148-2](https://doi.org/10.1016/0017-9310(72)90148-2)